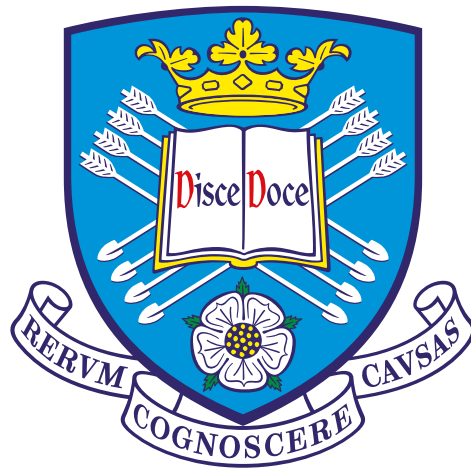


# Measuring and Modelling the Magnetic Field of the MICE Spectrometer Solenoids



**Joe Langlands**

Supervisor: Dr. Chris Booth

Department of Physics and Astronomy  
University of Sheffield

This dissertation is submitted for the degree of  
*Doctor of Philosophy*

September 2018



I would like to dedicate this thesis to my grandfather who sadly passed away when I was two years into this thesis programme. I will forever miss the surprisingly strong rum runners that you used to make.



## Declaration

Chapter one gives a brief description of the the main two motivations for building a muon accelerator from publications. Then some basic accelerator physics is detailed along with the basic arguments for why the ionisation cooling technique is required and how it works again from published material.

Chapter two details the entire MICE experiment using published material and MICE internal notes that are available publicly.

Chapter three describes: the two spectrometer solenoids; the partial return yoke and the field mapping machine with material taken from MICE internal notes and publications. Then chapter three details the field mapping work that occurred in March 2018 that I was made responsible for managing and performing. The remainder of the chapter gives a few small analyses, that are useful for chapter four, that are my own work. The magnetic axis analysis was inspired by work done by Victoria Blackmore and John Cobb. Also the  $B_\phi$  corrections work is my own interpretation and implementation of the work done with the ATLAS field maps and applied to the MICE field map data.

The geometrical fit model for chapter four originates from work previously done by Victoria Blackmore of which I extended greatly. The Fourier Bessel model has been applied to many magnet systems including ALEPH and ATLAS. I adapted the model for the MICE spectrometer solenoids and the work presented is entirely my own.

Joe Langlands  
September 2018



## Acknowledgements

Firstly, I would like to thank Chris Booth for giving me the opportunity to do this thesis in the first place and the support you have given me along the way. I would also like to thank the MICE target 'A-team' – Ed, Craig, Henry and Paul – we had a lot of 'fun' keeping the target running all these years. I learned so much too.

A big thanks also goes to all the lovely people that I have met on the MICE experiment. I have had a lot of entertaining times along the way, especially when the collaboration meetings had subsidised bars.

This thesis would not have been possible without the unwavering support and guidance of Victoria Blackmore. Thank you for handing me a load of data and code and trusting me with it all! Also thank you for putting up with me desperately asking for help week in week out.

Even though I only had the pleasure for the one week of data taking that we had, I would like to thank the CERN B-field mapping team – Pierre-Ange, Felix and Roman – for teaching me about the mapping machine and ultimately letting me loose on it.

Thank you to all my friends that I have met in Sheffield over the years who have now become a big close knit family. A special mention for the Sheffield PhD crew – Harry, Ross, Ellie, Sam and Mike – you guys helped me through difficult times and made the good times even better.

Everyday I count my blessings for meeting my wonderful girlfriend, Kat. You have supported me 100% throughout this time, you have given me the confidence to do well and you have given me the happiest times of my life. Thank you so much and I can not wait for the future.

Lastly I would like to thank my amazing parents and family for their incredible support over my entire university career.

*“Who ordered that?”* – I.I. Rabi

## Abstract

Muon accelerators offer precise measurements of the Higgs boson's properties and the PMNS matrix parameters. To make muon accelerators possible, tertiary beams of muons must first be cooled to allow them to be accepted into the accelerator and have a useful luminosity.

The Muon Ionisation Cooling Experiment aims to demonstrate the ionisation cooling technique. This method involves passing muons through an absorber material. MICE will demonstrate the method by measuring the emittance of a muon beam before and after it passes through an absorber material. The two spectrometer solenoids are critical to the experiment as they produce the magnetic fields which cause the muons to undergo helical trajectories, thus allowing the two scintillating fibre trackers to measure the emittance.

The field produced by the spectrometer solenoids needs to be known and software models are required for the tracking algorithm and simulation packages. A custom made field mapping machine was produced for the task of measuring the field produced by the solenoids. Using the data from this machine, models of the field are produced using least squares fitting. The full model uses a two-step procedure. The first step calculates two fields with differing lengths and thicknesses about the as-built dimensions of the coil being modelled. Then these fields are mixed until the square residuals with the data are minimised. The residual field is calculated between the model and data. The next stage of the model solves Laplace's equation to yield Fourier-Bessel expansions. The coefficients and phases of each term of the expansions are found by fitting to different parts of the residual field. The full model is then a sum of the mixed field and the Fourier-Bessel terms. The results of these models are compared with data and show decent agreement.



# Table of contents

<b>List of figures</b>	<b>xv</b>
<b>List of tables</b>	<b>xix</b>
<b>1 Introduction</b>	<b>1</b>
1.1 Motivations for Muon Accelerators . . . . .	2
1.1.1 Higgs Factories . . . . .	2
1.1.2 Neutrino Factories . . . . .	8
1.2 Accelerator Physics . . . . .	10
1.2.1 Emittance . . . . .	13
1.2.2 Luminosity . . . . .	15
1.2.3 Beam Matching . . . . .	15
1.3 Traditional Cooling Techniques . . . . .	16
1.3.1 Stochastic Cooling . . . . .	16
1.3.2 Electron Beam Cooling . . . . .	16
1.3.3 Synchrotron Damping . . . . .	17
1.4 Ionisation Cooling . . . . .	17
1.5 Conclusion . . . . .	18
<b>2 The Muon Ionisation Cooling Experiment</b>	<b>21</b>
2.1 MICE Hardware . . . . .	22
2.1.1 MICE Muon Beamline . . . . .	22
2.1.1.1 ISIS . . . . .	22
2.1.1.2 Target Mechanism . . . . .	23
2.1.1.3 Conventional Magnets . . . . .	25
2.1.1.4 Decay Solenoid . . . . .	25
2.1.1.5 Proton Absorber . . . . .	25
2.1.1.6 Diffuser . . . . .	26

2.1.2	Cooling Channel . . . . .	26
2.1.2.1	Spectrometer Solenoids . . . . .	28
2.1.2.2	Absorber Focus Coil . . . . .	28
2.1.2.3	Absorber Material . . . . .	29
2.1.3	Detectors . . . . .	30
2.1.3.1	Luminosity Monitor . . . . .	31
2.1.3.2	Time of Flight Detectors . . . . .	31
2.1.3.3	Cherenkov Light Detectors . . . . .	33
2.1.3.4	Scintillating Fibre Trackers . . . . .	34
2.1.3.5	KLOE-Light Detector . . . . .	36
2.1.3.6	Electron Muon Ranger . . . . .	38
2.2	MICE Software . . . . .	39
2.2.1	MICE Analysis User Software . . . . .	39
2.2.2	Configuration Database . . . . .	40
2.2.3	Controls, Monitoring and DAQ . . . . .	40
2.3	Conclusion . . . . .	41
<b>3</b>	<b>Field Mapping of the MICE Spectrometer Solenoids</b>	<b>43</b>
3.1	Motivation . . . . .	44
3.2	Spectrometer Solenoids . . . . .	45
3.2.1	As Built Dimensions . . . . .	47
3.2.2	SSU Cold Dimensions . . . . .	48
3.3	Superconducting Magnet Training . . . . .	49
3.3.1	SSD M1 and Quench Protection Issues . . . . .	49
3.4	Partial Return Yoke . . . . .	49
3.5	Field Mapping Machine . . . . .	51
3.5.1	Design . . . . .	51
3.5.2	Operation . . . . .	52
3.5.3	Mapper Coordinate System . . . . .	53
3.6	Field Mapping Data . . . . .	54
3.6.1	Original Data Set . . . . .	54
3.6.2	In Situ Data Set . . . . .	54
3.7	Field Mapper Survey . . . . .	56
3.7.1	Survey Results . . . . .	57
3.7.1.1	SSU . . . . .	58
3.7.1.2	SSD . . . . .	59
3.7.2	Applying Survey Corrections . . . . .	60

3.7.3	Mapper Coordinate Reproducibility . . . . .	61
3.8	Estimating the Centre Positions of the Coils . . . . .	62
3.9	Finding the Magnetic Axis . . . . .	65
3.9.1	Probe Tilt Corrections . . . . .	65
3.9.2	Method . . . . .	69
3.9.3	Test on a Simulated Coil . . . . .	71
3.9.4	Results . . . . .	72
3.10	Conclusion . . . . .	73
<b>4</b>	<b>Magnetic Field Models of the MICE Spectrometer Solenoids</b>	<b>75</b>
4.1	Calculating a Solenoidal Field . . . . .	76
4.2	Geometrical Fit Model . . . . .	77
4.2.1	Geometrical Fit Model for Match Coil Data . . . . .	79
4.2.2	Geometrical Fit Model for ECE Data . . . . .	81
4.2.3	Geometrical Fit Model of a Complete Spectrometer Solenoid . . . . .	82
4.2.4	Geometrical Fit Model Results . . . . .	83
4.2.5	Forming the Residual Field . . . . .	86
4.2.6	Effect of the PRY . . . . .	88
4.3	Fourier-Bessel Model . . . . .	91
4.3.1	Determining the Coefficients for the Fourier Terms . . . . .	94
4.3.2	Determining the Coefficients for the Hyperbolic Terms . . . . .	95
4.3.3	Determining the Coefficients for the Multipole Terms . . . . .	95
4.3.4	Fourier-Bessel Fit Examples . . . . .	95
4.3.5	Full Field Model . . . . .	96
4.4	Results of the Full Model . . . . .	97
4.5	Conclusion . . . . .	105
<b>5</b>	<b>Conclusions</b>	<b>107</b>
	<b>References</b>	<b>109</b>



# List of figures

1.1	Vertex factor for s-channel Higgs production, $f\bar{f} \rightarrow H$ . . . . .	3
1.2	Feynman diagrams for the production modes of the Higgs boson for proton-proton colliders . . . . .	4
1.3	Scale drawing comparing relative sizes of different proposed and existing particle accelerators. . . . .	6
1.4	Plot showing the effective s-channel cross-section for Higgs production versus the centre of mass energy. . . . .	7
1.5	Schematic drawing of a neutrino factory concept. . . . .	10
1.6	Diagram showing the relation between the beam ellipse in 2D trace space and the Twiss parameters $\alpha, \beta, \gamma$ . . . . .	12
1.7	Diagram of the main processes in the ionisation cooling technique. . . . .	17
2.1	MICE step IV layout . . . . .	22
2.2	Diagram of MICE muon beamline . . . . .	23
2.3	Cutaway of MICE target mechanism . . . . .	24
2.4	Photograph of the diffuser . . . . .	26
2.5	Rendering of the MICE step IV cooling channel . . . . .	27
2.6	Plots showing the axial field and betatron function . . . . .	28
2.7	Labelled cutaway drawing of the absorber focus coil . . . . .	30
2.8	Labelled diagram showing the design of the luminosity monitor . . . . .	31
2.9	Time of Flight Plots for a mixed beam and a1 muon beam . . . . .	32
2.10	Photograph of TOF1 installed in the MICE beamline. . . . .	33
2.11	Labelled exploded view of the MICE Cherenkov detectors . . . . .	34
2.12	Photograph of one of the scintillating fibre trackers . . . . .	35
2.13	Diagram showing the arrangement of the tracker fibre doublet layers. . . . .	36
2.14	Cross sectional diagram showing the arrangement of the lead foil and scintillating fibres in the KL detector . . . . .	37

2.15	Labelled exploded view of one KL module on the left. On the right is a rendering of the whole KL detector showing how the seven modules are arranged. . . . .	37
2.16	Drawings of the EMR detector . . . . .	38
2.17	Plots showing a muon decay and an electron shower event in the EMR detector	39
3.1	Labelled cutaway diagram showing the cold mass assembly of a spectrometer solenoid and cutaway diagram of a spectrometer solenoid . . . . .	46
3.2	Simplified circuit diagram of the spectrometer solenoids . . . . .	47
3.3	Labelled rendering showing how the cooling channel is enclosed within the partial return yoke . . . . .	50
3.4	Labelled diagram of the field mapping machine. . . . .	51
3.5	Schematic diagram of the mapper disk and a close up of one of the Hall probes	52
3.6	Plots showing the axial field component for each mapped setting for both spectrometer solenoids . . . . .	56
3.7	Diagram showing the position of the survey target for the three sets of survey data . . . . .	57
3.8	Plots summarising the results of the survey performed on the mapping machine installed in SSU. . . . .	58
3.9	Plots summarising the results of the survey performed on the mapping machine installed in SSD. . . . .	60
3.10	Histogram showing the longitudinal interval between neighbouring points for all survey data. . . . .	62
3.11	Histogram of residual between measured $B_z$ and $\langle B_z \rangle$ for each data point. . . . .	63
3.12	Plots showing the polynomial fits used for the centre finding algorithm. The titles indicate the coil under inspection. . . . .	64
3.13	Vector plot showing the transverse field as measured by probe 1 for a whole rotation of the mapper disk at a single position in $z$ . . . . .	66
3.14	Plot showing an example of the fit performed on the left hand side of equation 3.13. . . . .	67
3.15	Vector plot showing the same transverse field as figure 3.13 but with the $B_\phi$ components corrected. . . . .	68
3.16	Plots showing $A_{\phi_z}$ and $A_{\phi_r}$ mixing angles for probes 1-5 for both solenoids.	68
3.17	Plots of $B_{x,y}$ vs $x',y'$ for a particular $z'$ position using data from all probes. . . . .	70
3.18	Plot showing the $B_r, B_\phi$ and $B_z$ components of the test coil as would be measured by a Hall probe at a radius of 0.15 m and angle of $30^\circ$ . . . . .	72

4.1	Cutaway diagram showing the arrangement of the two bracketing coils and the true coil. . . . .	78
4.2	Plot illustrating the axial field at $r = 0$ of SSU's centre coil, powered at 30 A, as calculated from the listed dimensions in green. The blue and red lines show axial field from the two bracketing fields. . . . .	79
4.3	Histograms of the residuals between the geometrical fit model and the data for the 3T-SSU setting for each field component. . . . .	83
4.4	Histograms of the residuals between the geometrical fit model and the data for the 2T-SSD setting for each field component. . . . .	84
4.5	Histograms of the residuals between the geometrical fit model and the data for the 3T-SSD setting for each field component. . . . .	85
4.6	Example of a fitted cubic spline to the $B_z$ component at a $z$ slice of data. The red points show the data and the blue surface is the fitted cubic spline. . . . .	86
4.7	Histograms of the absolute (left) and fractional (right) residuals between the interpolated values and data. . . . .	87
4.8	Plots showing the residual axial field for all $z$ and $\phi$ for each cylindrical surface. These plots show the residual between the geometrical fit model and the 3T-SSU setting. . . . .	89
4.9	Plots showing the residual axial field for all $z$ and $\phi$ for each cylindrical surface. These plots show the residual between the geometrical fit model and the 3T-SSD setting. . . . .	90
4.10	Examples of the Fourier-Bessel fit to the residual $B_z$ field on the bounding cylinder surface. The residual fields are represented by the purple surfaces. The black wire frame surfaces are calculated from the $B_z$ expansion. . . . .	96
4.11	Residual $B_z$ field on each radial surface between the full field model and the interpolated data for the 3T-SSU setting. . . . .	98
4.12	Residual $B_z$ field on each radial surface between the full field model and the interpolated data for the 3T-SSD setting. . . . .	99
4.13	Residual $B_z$ field on each radial surface between the full field model and the interpolated data for the 2T-SSD setting. . . . .	100
4.14	Histograms of the residuals between the full model and the data for the 3T-SSU setting. . . . .	101
4.15	Histograms of the residuals between the full model and the data for the 3T-SSD setting. . . . .	102
4.16	Histograms of the residuals between the full model and the data for the 2T-SSD setting. . . . .	103

4.17 Histograms of the fractional error,  $\Delta B_z/B_z$ , in terms of percentage for the three comparison fields. . . . . 104

# List of tables

2.1	Table of diffuser iris parameters . . . . .	27
2.2	Table of radiation length, mean energy loss and equilibrium emittance for the MICE absorbers . . . . .	29
2.3	Table showing key parameters for the TOF detectors . . . . .	33
2.4	Table showing which particle species are above the threshold velocity, and therefore show a signal, for both Cherenkov detectors . . . . .	34
3.1	As built coil dimensions of SSU . . . . .	48
3.2	As built coil dimensions of SSD . . . . .	48
3.3	Estimated cold dimensions of SSU . . . . .	48
3.4	Probe number with its corresponding radius from the centre of the disk. . .	52
3.5	Table of mapped currents for SSU . . . . .	55
3.6	Table of mapped currents for SSD . . . . .	55
3.7	Table of centre positions in $z$ and $z'$ for all of SSU's coils. Coloured cells are those that are calculated from the method described above. . . . .	65
3.8	Table of centre positions for all of SSD's coils. . . . .	65
3.9	Rotation angles and offsets applied to the simulated test coil. . . . .	71
3.10	Calculated rotation angles and offsets of the simulated test coil. . . . .	71
3.11	Estimated rotation angles and offsets of SSU. . . . .	72
3.12	Estimated rotation angles and offsets of SSD. . . . .	72
4.1	Table summarising the residuals of the full field model for each of the MICE beam setting field maps. . . . .	105



# Chapter 1

## Introduction

During the mid 20th Century, particle physics experienced an explosion of discoveries. Many new particles were discovered due to new techniques in detection and also the invention of early particle accelerators. Suddenly a need to classify these new particles according to their properties and interactions was required.

Murray Gell-Man laid the foundations when he published papers describing the so-called 'Eightfold Way'[1]; this classified many newly discovered hadrons into multiplets according to their quantum numbers, namely their charge and strangeness. This eventually led to the quark model and then evolved into Quantum Chromodynamics (QCD) which uses the non-Abelian  $SU(3)$  group to explain the underlying interactions of the strong force.

At around the same time, Sheldon Glashow<sup>1</sup> worked on describing how the electromagnetic and weak forces could be unified by using an  $SU(2) \times U(1)$  gauge group. This work linked the already established theory of Quantum Electrodynamics (QED) with the weak force into electroweak theory.

The Standard Model of particle physics incorporates the strong, weak and electromagnetic forces using a product of the three groups mentioned above:  $SU(3) \times SU(2) \times U(1)$ . The Standard Model is a hugely successful theory, with many of its predictions being proven. It does however have its problems. It does not include the gravitational force with the other three. It also does not give an answer to dark matter or dark energy nor does it predict neutrino oscillations.

The electroweak theory is a chiral theory with the leptons being represented by weak isospin doublets. This means that simple mass terms in the Lagrangian could not be added to account for the particles masses because they break the gauge invariance as left and right handed-particles have different gauge transformations. A mechanism in which the fermions

---

<sup>1</sup>Abdus Salam and Steven Weinberg also contributed heavily to the theory independently of Glashow.

gain their masses along with the heavy gauge bosons of the weak interaction, whilst leaving the photon massless, was needed.

This mechanism is of course now widely known as the Higgs mechanism (or more accurately the Brout-Englert-Higgs mechanism). It originates from theory used to describe how superconductivity works and it predicted a massive scalar boson. After many years of being hypothetical, the Higgs boson was discovered in 2012 by the ATLAS and CMS experiments at CERN with a mass of 126 GeV [2, 3]. A piece of the Standard Model puzzle was found and it still proves to be a successful theory.

The discovery of the Higgs boson and neutrino oscillations has set the focal point for new particle physics experiments and the accelerator is the workhorse. The muon has gained attention for new accelerator experiments as it has numerous advantages. Precise measurements of the mass of the Higgs boson could be carried out at a lepton anti-lepton collider especially a muon collider. Also muon accelerators known as neutrino factories can provide intense neutrino beams of perfectly known flavour to study oscillations.

However more research and development is required to make a muon accelerator become reality. The muon's instability proves to be a hurdle and traditional accelerator techniques are futile, as described later in section 1.3. The Muon Ionisation Cooling Experiment (MICE) is a proof of concept experiment that aims to measure a reduction of the emittance of a muon beam using the ionisation cooling technique. This is explored in more detail from section 1.2 and beyond. The actual experiment is detailed in chapter 2. First a description of the main proposed uses for muon accelerators is given.

## 1.1 Motivations for Muon Accelerators

Muon colliders are ideal candidates for so-called 'Higgs factories'. Higgs factories are proposed particle accelerators that collide high luminosity beams to produce large amounts of Higgs bosons to study its properties in detail. Higgs factories are discussed in section 1.1.1 with a description of the different types and their respective advantages and disadvantages.

Muon storage rings can be used to produce intense beams of neutrinos with a well known flavour profile for precise neutrino oscillation experiments. Such facilities are known as neutrino factories. These are discussed in section 1.1.2.

### 1.1.1 Higgs Factories

There are two obvious subcategories for particle colliders: hadron and lepton colliders. Each has advantages and disadvantages over the other in the context of Higgs physics. First a

description of hadron colliders will be given since one was used to discover the Higgs boson – the LHC.

## Hadron Colliders

The two main forms of hadron colliders are proton-proton ( $pp$ ) or proton anti-proton synchrotrons ( $p\bar{p}$ ), examples of which are the LHC and Tevatron respectively. Two beams circulate the accelerator ring in opposing directions and are made to collide with each other at the interaction point (IP). Detectors, like ATLAS and CMS, are built around the IP to detect the products of the collisions.

Protons are composite particles made up of three valence quarks ( $uud$ ), sea quarks and gluons. These constituent particles share the energy that the accelerator gives to the proton. This means that the initial state energy is not well defined. There are also large QCD backgrounds, mainly in the form of jets arising from the break up of the colliding protons. These QCD backgrounds obscure Higgs decays into final states containing quarks and so techniques, such as b-tagging, are required.

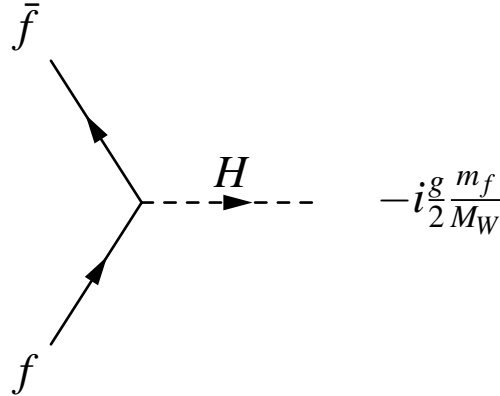


Fig. 1.1 Vertex factor for s-channel Higgs production,  $f\bar{f} \rightarrow H$ .

Figure 1.1 shows the three-point coupling between a fermion, anti-fermion pair and a Higgs boson. The coupling is dependent on the mass of the fermion. As the masses of the  $u$  and  $d$  quarks are small, the cross section for direct production is very small at proton colliders. Instead other production modes with much higher cross sections and requiring higher collision energies are available. For the LHC these are shown in figure 1.2.

Given a mass of the Higgs, the Standard Model predicts its decay width,  $\Gamma_H$ . Precisely measuring the width is therefore a good way to test the Standard Model as a significant discrepancy from the prediction indicates beyond Standard Model (BSM) physics [5]. The composite nature of protons and the large backgrounds produced means that it is extremely difficult to measure the Higgs width using a hadron collider [6]. By far the best way to

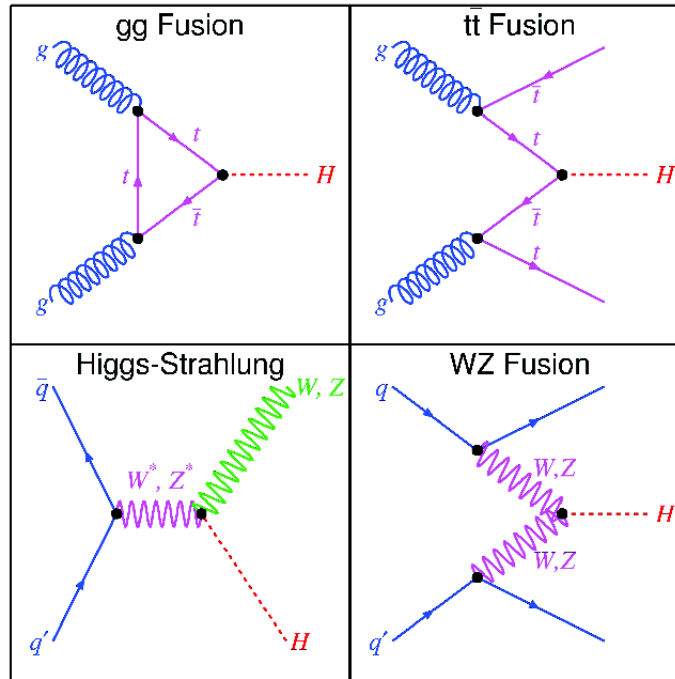


Fig. 1.2 Feynman diagrams for the production modes of the Higgs boson for proton-proton colliders [4].

measure  $\Gamma_H$  is to use a  $\mu^- \mu^+$  collider with good energy resolution to produce Higgs bosons via the s-channel to measure the resonance peak.

## Lepton Colliders

Leptons are point-like fundamental particles which have advantages when colliding them. The most obvious is that the energy is well defined as it is not shared over any constituent particles. Also the initial state is well known and the final states will not have to be picked out of large QCD backgrounds. The main sources of background are secondary  $e^+e^-$  production and photon-photon collisions, which can leave hadronic final states [7].

The Large Electron Positron Collider (LEP) was used to search for the Higgs boson but it only succeeded in excluding mass ranges. Due to the very low electron mass, the coupling to the Higgs is very weak meaning that s-channel production is negligible and measuring  $\Gamma_H$  is not directly accessible although still possible by tagging leptonic decays of the Z boson in the Higgs-strahlung process  $e^+e^- \rightarrow HZ$  [8]. The dominant production modes are  $W/Z$ -Fusion and Higgs-Strahlung like in hadron colliders. A consequence of this is that the centre of mass energy must exceed the rest energy of the Higgs boson.

Building circular  $e^+e^-$  colliders with higher energies than LEP requires overcoming a few technical challenges, the most obvious of which is the energy loss due to synchrotron radiation. As particles are guided around the collider ring by magnetic fields, they emit synchrotron radiation costing them energy. The synchrotron power loss of a particle being accelerated to a total energy  $E$  and with a mass  $m$  is given by

$$P_{\text{loss}} \propto \frac{E^4}{m^4 \rho} \quad (1.1)$$

where  $\rho$  is the bending radius of the accelerator. Hence the power loss increases with the accelerator energy to the fourth power. A remedy for this is to make a linear collider in the case of the proposed ILC accelerator.

The International Linear Collider (ILC) is a proposed linear  $e^+e^-$  collider with a collision energy in the range 200-500 GeV [9]. With a maximum collision energy roughly double that of the maximum LEP reached, it promises a wider physics program searching for new particles and following up on measurements made by the LHC. The linear design means that to reach high energies using existing RF-cavity acceleration, the accelerator portions have to be tens of kilometers long. The baseline for ILC is roughly 30km. From a practical standpoint the cost and geographical footprint become serious factors to consider. The physics argument for the ILC is convincing in the context of Higgs factories as the technology is available and measurements of the Higgs parameters can be made.

Circular colliders are more desirable for a Higgs factory because there can be multiple IPs and therefore more detectors can be in operation. To build circular  $e^+e^-$  colliders with higher collision energies than LEP, the radius of the machine will need to be increased to overcome the significant synchrotron radiation. Some machines have been proposed with large radii such as TLEP with a proposed circumference of  $\sim 80$  km, resulting in a bending radius that is roughly triple that of LEP [10]. However the returns are diminishing and again the practicalities need to be considered.

Another disadvantage is the limitations due to beamstrahlung. Beamstrahlung is the emission of synchrotron radiation from one beam due to the electromagnetic field of the other beam as they collide. As the particles in the beam radiate photons, the energy spread of the beam increases. Since knowledge of the collision energy is one of the main advantages of a lepton collider, this phenomenon must be taken into account in a colliders design.

## Muon Colliders

Colliding muons have significant advantages in the context of lepton colliders. As was mentioned this is due to the higher muon mass,  $m_\mu \approx 207m_e$ . There are advantages to both the physics and the practicality of building the collider.

Firstly it is obvious from equation 1.1 that muons emit much less synchrotron radiation. For a given energy and radius, muons will emit a factor of approximately  $10^9$  less radiation. This enables much more compact circular colliders with a higher energy reach. Figure 1.3 illustrates this.

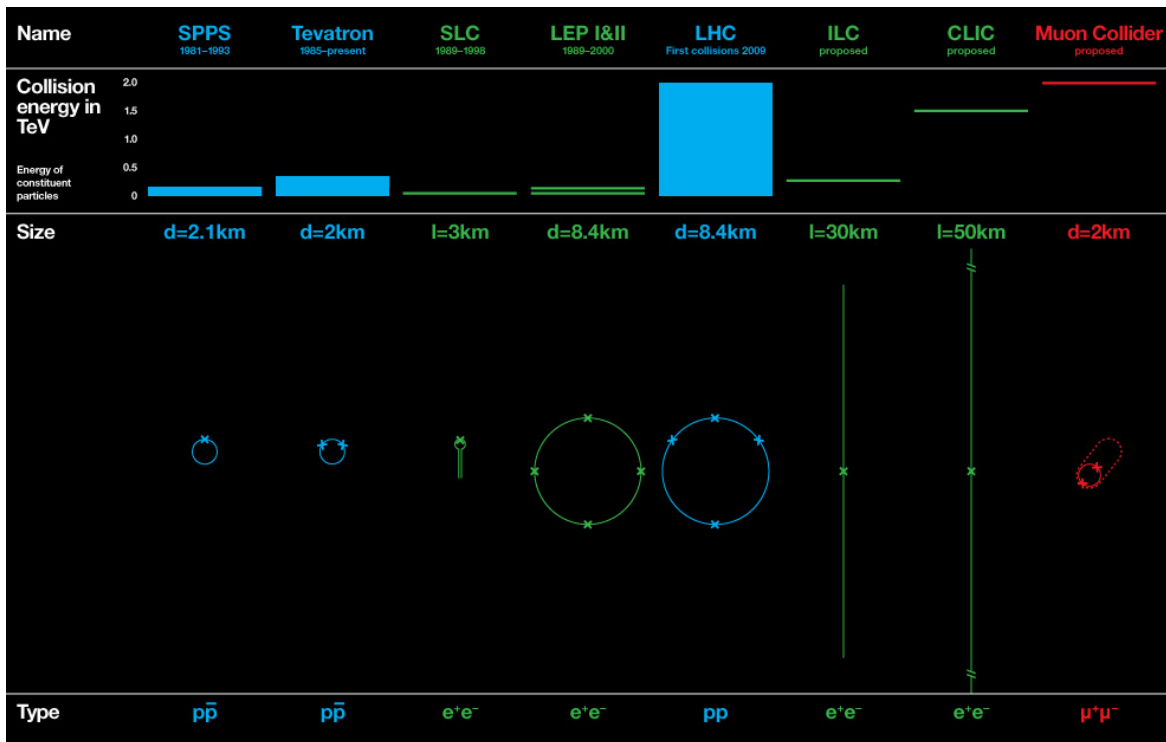


Fig. 1.3 Scale drawing comparing relative sizes of different proposed and existing particle accelerators. Details about potential and actual collision energies is also given. Image adapted from Muon Accelerator Program website [11].

Secondly beamstrahlung is greatly reduced in a muon collider for the same argument as synchrotron radiation – the higher mass means less radiation. Therefore muon colliders would have better defined collision energy spreads than electron colliders.

As mentioned, one of the main physics advantages for muon colliders is the capability to directly measure the width of the Higgs Boson. A consequence of the vertex factor shown in figure 1.1 is that the cross section for s-channel production of Higgs bosons is much higher for muons than electrons or first generation quarks. By tuning the centre of mass collision

energy,  $\sqrt{s}$ , of a muon collider to around the Higgs mass, a scan of the resonance peak can be performed. However the energy spread of the muon beam will convolute the Breit-Wigner distribution of the decay, obscuring the measurement. This effect is shown in figure 1.4. Providing the energy spread of the beam is around the same as the Higgs width, a precise measurement of the width can be performed.

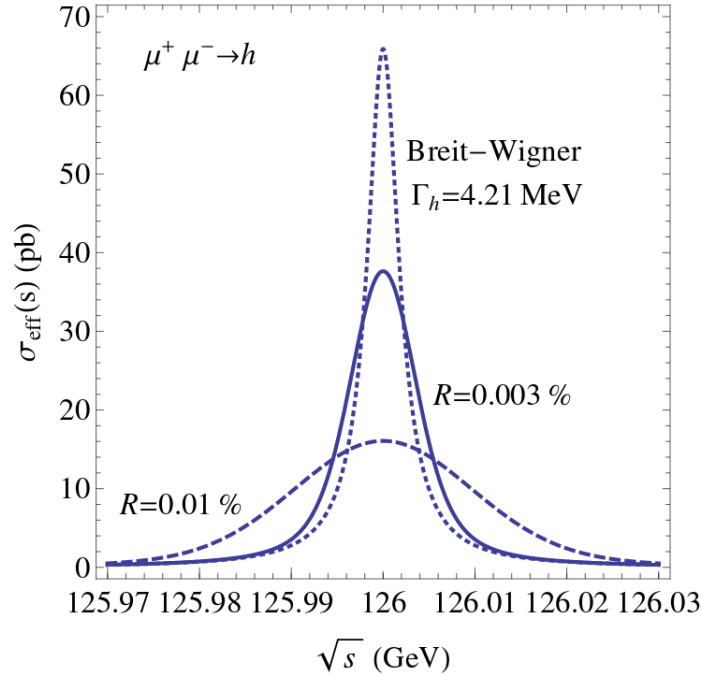


Fig. 1.4 Plot showing the effective  $s$ -channel cross-section for Higgs production versus the centre of mass energy. The true distribution is shown for a Higgs width of 4.21 MeV and  $m_H = 126$  GeV. Also shown are the measured distributions for a muon collider with energy spreads of 0.01% and 0.003%. Plot from [6].

Whilst the Higgs physics arguments are the most attractive, muon colliders can have rich physics programmes. Included is the ability for accurate measurements of the top quark mass using threshold scans for the processes  $\mu^+\mu^- \rightarrow X \rightarrow t\bar{t}$ . This measurement along with an accurate measurement of  $m_H$  would be able to answer the question of whether the electroweak vacuum is stable or metastable [12].

The key technical challenges for muon colliders arise from the muon's instability. Significant backgrounds from electrons produced from decaying muons will exist in the detectors whilst also potentially damaging the accelerators quadrupole and dipole magnets. It has been suggested that with careful consideration for the layout of the magnetic lattice and by installing tungsten shielding, the effects of decay electrons can be mitigated [13].

Muons beams are tertiary because they are derived from pion beams which in turn are made from proton beams fired at metal targets. Therefore the muons have a large spread of transverse and longitudinal momenta due to the decay kinematics. This spread is quantified by the *emittance*,  $\epsilon$ , which is explained further in section 1.2.1.

Emittance is related to the luminosity of the accelerator as will be seen in section 1.2.2. The emittance of the muon beam needs to be lowered in order to approach useful luminosities for a collider. Established emittance reduction techniques, known as “cooling” techniques for reasons that will become obvious, are not suitable for use on muon beams. This is described in section 1.3. However the untested ionisation cooling technique offers a way to cool muon beams for use in accelerators.

### 1.1.2 Neutrino Factories

The Homestake experiment observed that the electron neutrino flux originating from the Sun was about a third of that expected by the standard solar model (SSM) [14]. This became known as the solar neutrino problem. Bruno Pontecorvo proposed that neutrinos oscillate between flavours due to the flavour and mass eigenstates being separate. Consequentially a portion of electron neutrinos become muon or tau neutrinos at the detector which was only sensitive to  $\nu_e$ . The Sudbury Neutrino Observatory (SNO) confirmed neutrino flavour oscillations by using a detector that was sensitive to all flavours. The flux of all flavours combined added up to the expected flux from the SSM [15].

The theory was further developed by Maki, Nakagawa and Sakata and the now ubiquitous matrix formalism derived. Neutrino flavour eigenstates are related to the mass eigenstates via:

$$|\nu_\alpha\rangle = \sum_i U_{\alpha i}^* |\nu_i\rangle \quad (1.2)$$

where  $|\nu_\alpha\rangle$  are the flavour eigenstates with  $\alpha = e, \mu, \tau$  and  $|\nu_i\rangle$  are the mass eigenstates with  $i = 1, 2, 3$ . Then  $U_{\alpha i}^*$  is the complex conjugate of the mixing matrix known as the Pontecorvo-Maki-Nakagawa-Sakata (PMNS) matrix. This matrix underpins the theory of neutrino oscillations. For Dirac fermions<sup>2</sup> the matrix can be parameterised as

$$U_{\text{PMNS}} = \begin{pmatrix} c_{12}c_{13} & s_{12}c_{13} & s_{13}e^{-i\delta} \\ -s_{12}c_{23} - c_{12}s_{23}s_{13}e^{i\delta} & c_{12}c_{23} - s_{12}s_{23}s_{13}e^{i\delta} & s_{23}c_{13} \\ s_{12}s_{23} - c_{12}c_{23}s_{13}e^{i\delta} & -c_{12}s_{23} - s_{12}c_{23}s_{13}e^{i\delta} & c_{23}c_{13} \end{pmatrix} \quad (1.3)$$

<sup>2</sup>Whether neutrinos are Dirac or Majorana is not clear at present.

where  $c_{ij}$  and  $s_{ij}$  represent  $\cos \theta_{ij}$  and  $\sin \theta_{ij}$  respectively. The parameters  $\theta_{ij}$  are the three mixing angles and  $\delta$  is the CP-violating phase. Neutrino experiments of various types have been designed and operated to measure the mixing angles. The angle  $\theta_{13}$  in particular is measured by experiments that use nuclear reactors or neutrino beams derived from accelerators. Neutrino beams from accelerators offer more control over the flux, flavour profile and energy spectrum.

The current standard for producing neutrino beams for experiments like T2K are known as super beams. Neutrinos are derived from the primary decay mode of pions:

$$\begin{aligned}\pi^+ &\rightarrow \mu^+ + \nu_\mu \\ \pi^- &\rightarrow \mu^- + \bar{\nu}_\mu\end{aligned}$$

Super beams start with high energy beams of protons which are typically collided with a graphite target. Large quantities of pions are produced from QCD processes. These pions are then strongly focussed using a magnetic horn and allowed to decay in a chamber, resulting in a directional neutrino beam.

A disadvantage of super beams is the inevitable contamination from decays of other mesons and the large energy spread of the beam. The contamination hinders the measurement of  $\theta_{13}$  and  $\delta$ . To remedy this super beams are usually aimed slightly off-axis to the far detector exploiting the two-body decay kinematics of pions resulting in an almost mono-energetic and high  $\nu_\mu$  purity beam [16]. Off-axis beams sacrifice luminosity for lower backgrounds and better energy resolution.

Neutrino factories are proposed accelerator complexes that can produce high purity and intense beams of neutrinos with easily tunable energies. Neutrinos are derived from muon decays:

$$\begin{aligned}\mu^+ &\rightarrow e^+ + \nu_e + \bar{\nu}_\mu \\ \mu^- &\rightarrow e^- + \bar{\nu}_e + \nu_\mu\end{aligned}$$

Muon beams are circulated in racetrack shaped storage rings shown in figure 1.5. These beams are derived in a similar manner to those in a muon collider. Muons that decay on the long straight sections produce an intense collimated beam of neutrinos. The resulting beam is a 50-50 mix of electron and muon flavoured (anti-) neutrinos.

Neutrino factories give access to survival and appearance studies for flavour oscillations  $\nu_e \rightarrow \nu_{e,\mu,\tau}$  owing to the fact that 50% of the beam is electron flavoured. The oscillation  $\nu_e \rightarrow \nu_\mu$  is known as the ‘‘golden channel’’ for neutrino factories. Muon neutrino appearance can be measured by detecting muons that are the opposite charge of the ones from which the

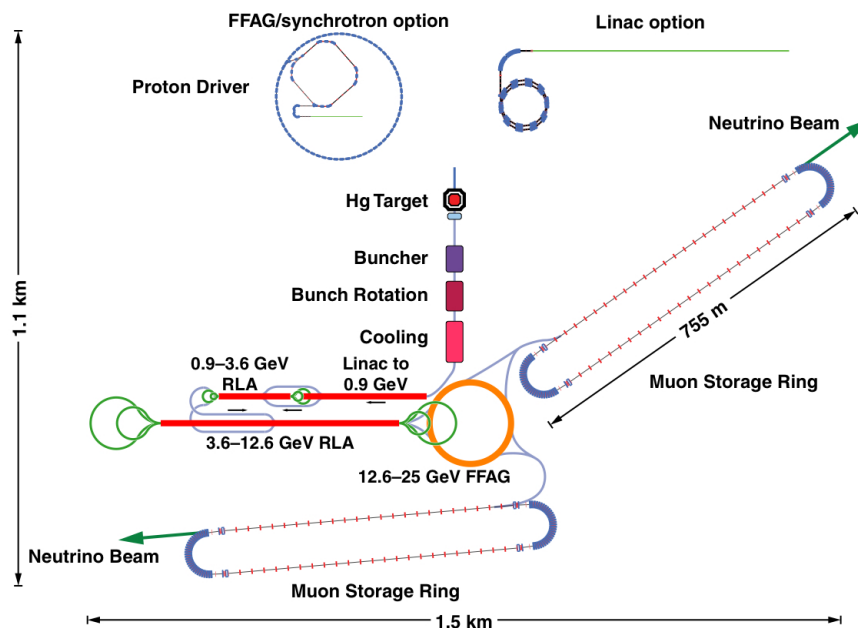


Fig. 1.5 Schematic drawing of a neutrino factory concept.

neutrino beam was derived. This requires a magnetised detector to discriminate the charge. By comparing the measured probabilities of the appearances  $\nu_e \rightarrow \nu_\mu$  and  $\bar{\nu}_e \rightarrow \bar{\nu}_\mu$  the value for  $\delta$  can be inferred [17].

As with muon colliders, muon beams need to be cooled before use in a neutrino factory, although the cooling requirements for a neutrino factory are much less than for a collider. This is because high luminosity, defined in section 1.2.2, is desired for a muon collider to maximise the rate of particle interactions.

## 1.2 Accelerator Physics

Before emittance and cooling is discussed, it is first useful to review some accelerator physics and the motions of particles within an accelerator.

Magnets are used to guide particles round an accelerator in a collimated beam. In synchrotrons, like the LHC, the two main types of magnet used to keep the particle beams on the design orbit are *dipoles* and *quadrupoles*. Dipoles bend particles around the design trajectory and quadrupoles focus the beam so that it does not diverge excessively and hit the beam pipe. However particles do not follow the design orbit perfectly, instead the magnetic lattice applies restoring forces to the particles so that they oscillate about this orbit. These oscillations are called *betatron oscillations*. The following formulation is from [18].

The motion of particles perpendicular to the design trajectory is governed by Hill's equation:

$$\frac{d^2u(s)}{ds^2} + k(s)u(s) = 0 \quad (1.4)$$

where  $u(s)$  is one of two positions perpendicular to  $s$ ,  $k(s)$  is a function that represents the periodic focussing from the magnetic lattice and  $s$  is the distance along the design orbit.

The trial solution is similar to the harmonic oscillator solution:

$$u(s) = \sqrt{\varepsilon} \sqrt{\beta(s)} \cos(\psi(s) - \psi_0) \quad (1.5)$$

Using this trial solution in equation 1.4 and comparing coefficients of cosines and sines (and dropping the  $(s)$  arguments and letting derivatives with respect to  $s$  be denoted by a prime symbol) yields:

$$\begin{aligned} \frac{1}{2} \left( \beta \beta'' - \frac{1}{2} \beta'^2 \right) - \beta^2 \psi'^2 + \beta^2 k &= 0 \\ \beta' \psi' + \beta \psi'' &= (\beta \psi')' = 0 \end{aligned} \quad (1.6)$$

It is obvious from the second relation that  $\beta \psi' = \text{const}$ , and a normalisation of the phase function,  $\psi$ , is picked so that  $\beta \psi' = 1$  so that the first relation in equations 1.6 becomes:

$$\frac{1}{2} \beta \beta'' - \frac{1}{4} \beta'^2 + \beta^2 k = 1 \quad (1.7)$$

This equation governs the form of the betatron function,  $\beta(s)$ , which represents the periodic magnetic focussing lattice of the accelerator in equation 1.5.

Making the substitution  $q(s) = \sqrt{\beta(s)}$  and substituting into equation 1.7 the equation becomes:

$$q'' + kq - \frac{1}{q^3} = 0 \quad (1.8)$$

The above equation shows that the betatron function always stays the same sign and never reaches zero. This can be seen by letting  $q$  tend to zero which according to the above equation means that  $q''$  will get very large, turning  $q$  away from zero. It is conventional to choose only the positive solutions of the betatron function so that it is always positive and non zero.

Now using the definition of  $u(s)$  in equation 1.5 and its derivative. By eliminating terms with the phase,  $\psi(s)$ , using  $\cos^2 \theta + \sin^2 \theta = 1$  the relation below is formed:

$$\gamma u^2 + 2\alpha u u' + \beta u'^2 = \varepsilon \quad (1.9)$$

where the parameters  $\alpha(s)$ ,  $\gamma(s)$  are defined as:

$$\begin{aligned}\alpha(s) &= -\frac{\beta'(s)}{2} \\ \gamma(s) &= \frac{1 + \alpha^2(s)}{\beta(s)}\end{aligned}\tag{1.10}$$

Equation 1.9, known as the Courant-Snyder invariant, gives information about the nature of  $\epsilon$ . It is a constant of motion and known as the *emittance*. The parameters,  $\alpha, \beta, \gamma$  are known as the *Twiss* parameters.

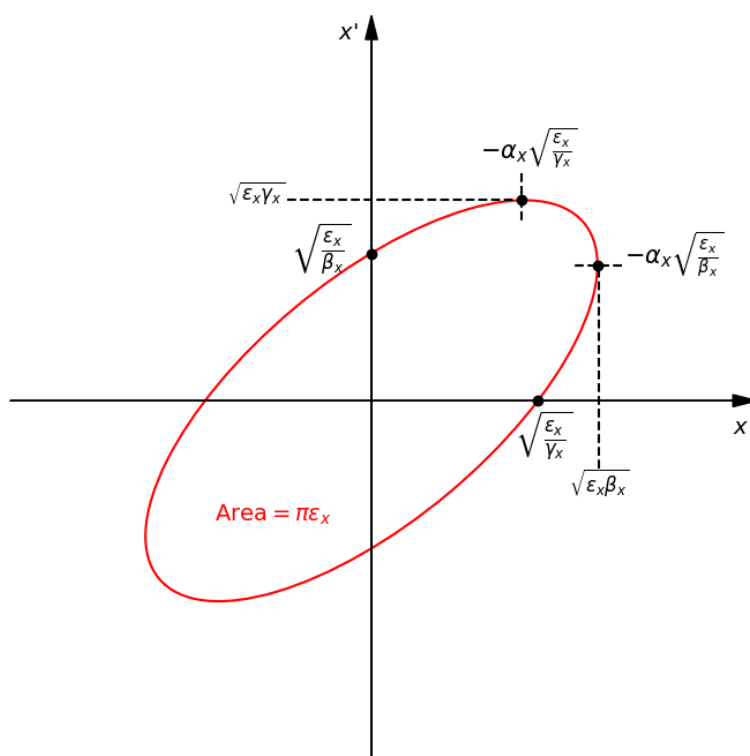


Fig. 1.6 Diagram showing the relation between the beam ellipse in 2D trace space and the Twiss parameters  $\alpha, \beta, \gamma$ .

The reason for the definitions of  $\alpha(s)$  and  $\gamma(s)$  as they are is that equation 1.9 is now in the same form as that of an ellipse in the  $u-u'$  plane. Due to the geometry of the ellipse and the fact that the area enclosed is defined as  $A = \pi\epsilon$ , the Twiss parameters obey the relation:

$$\beta(s)\gamma(s) - \alpha^2(s) = 1\tag{1.11}$$

Figure 1.6 shows a diagram of the beam ellipse for some distance along the beam axis and the relation between the emittance and the Twiss parameters. A particle undergoing betatron oscillations traces out ellipses in the transverse trace spaces,  $x$ - $x'$  and  $y$ - $y'$  with:

$$\begin{aligned} x' &= \frac{dx}{ds} = \frac{p_x}{p_s} \\ y' &= \frac{dy}{ds} = \frac{p_y}{p_s} \end{aligned} \quad (1.12)$$

where  $p_s$  is the longitudinal momentum. The above equations show the relationship between phase space,  $(x, p_x)$ , and trace space,  $(x, x')$ .

The area of this ellipse is a conserved quantity according to Liouville's theorem which states a volume in phase space is conserved providing the particles obey the canonical equations of motion. This means that where there is no energy change and the particles are progressing through the magnetic lattice of the accelerator, the transverse emittance is constant.

### 1.2.1 Emittance

The emittance is an important parameter in accelerator physics, as it has many implications for the physical size and density of the beam. From equation 1.5, the motion of the particles undergoing the largest amplitude betatron oscillations can be seen by setting the cosine function to  $\pm 1$ . This leaves:

$$E(s) = \pm \sqrt{\varepsilon} \sqrt{\beta(s)} \quad (1.13)$$

This is known as the envelope function and all the particles in a beam will fall within its bounds. The particles that form the beam envelope have the largest area ellipses in trace space and have area equal to  $\pi\varepsilon$ . The trace space ellipses of all other particles will fall inside this ellipse. This is one definition of the emittance for the whole beam.

Emittance is not invariant under acceleration or deceleration. Since this is not true in particle accelerators it is convenient to define the normalised emittance which is invariant:

$$\varepsilon_N = \gamma_r \beta_r \varepsilon \quad (1.14)$$

where  $\gamma_r$  and  $\beta_r$  are the Lorentz factor and relativistic velocity respectively.

Rather than defining the emittance for the whole beam in terms of the particles on the beam envelope, it is better to define the RMS emittance,  $\varepsilon_{\text{RMS}}$ , which assumes the beam density has a Gaussian distribution. Then  $\varepsilon_{\text{RMS}}$  is defined by the area in trace space enclosed

by one standard deviation in each trace space coordinate. For a transverse coordinate, say  $x$ , the two dimensional RMS emittance can then be interpreted in terms of the determinant of the covariance matrix in trace space

$$\epsilon_{x,\text{RMS}} = \sqrt{\det(\Sigma_x)} \quad (1.15)$$

with the covariance matrix

$$\Sigma_x = \begin{pmatrix} \langle x^2 \rangle & \langle xx' \rangle \\ \langle xx' \rangle & \langle x'^2 \rangle \end{pmatrix} \quad (1.16)$$

This covariance matrix can be related to the Twiss parameters by using the general equation for an  $n$ -dimensional ellipse:

$$\vec{u}^\top \sigma^{-1} \vec{u} = 1 \quad (1.17)$$

where  $\vec{u}$  is the coordinate vector,  $\vec{u}^\top$  is its transpose and  $\sigma$  is a symmetric matrix. An  $n$ -dimensional ellipse defined by this equation has the volume

$$V_n = \frac{\pi^{n/2}}{\Gamma(1 + n/2)} \sqrt{\det(\sigma)} \quad (1.18)$$

where  $\Gamma$  is the gamma function [18].

Working in 2D trace space so that  $\vec{u}^\top = (x, x')$  and multiplying out equation 1.17, the following relation is obtained:

$$\sigma_{22}x^2 + 2\sigma_{12}xx' + \sigma_{11}x'^2 = 1 \quad (1.19)$$

where  $\sigma_{ij}$  are the elements of the matrix and  $\sigma_{12} = \sigma_{21}$  due to  $\sigma$  being a symmetric matrix. Comparing the above relation with the Courant-Snyder invariant from equation 1.9 reveals the elements of the matrix  $\sigma$ :

$$\sigma = \epsilon \begin{pmatrix} \beta & -\alpha \\ -\alpha & \gamma \end{pmatrix} \quad (1.20)$$

Hence the Twiss parameters for an ensemble of muons can be expressed in terms of the elements of the covariance matrix  $\Sigma_x$  accordingly:

$$\begin{aligned} \langle x^2 \rangle &= \epsilon\beta \\ \langle x'^2 \rangle &= \epsilon\gamma \\ \langle xx' \rangle &= -\epsilon\alpha \end{aligned} \quad (1.21)$$

The expression for the emittance is recovered by considering the relation 1.11:

$$\varepsilon = \sqrt{\det(\boldsymbol{\sigma})} = \sqrt{(\varepsilon\beta)(\varepsilon\gamma) - (\varepsilon\alpha)^2} = \varepsilon\sqrt{\beta\gamma - \alpha^2} \quad (1.22)$$

The concept of emittance can be extended to four –  $(x, x', y, y')$  – and six dimensional –  $(x, x', y, y', t, E)$  – trace spaces by extending the covariance matrix accordingly and also taking the  $n^{\text{th}}$  root of the determinant where  $n$  is the phase space dimension.

## 1.2.2 Luminosity

Luminosity is an important parameter for particle colliders. The luminosity underpins how many interactions occur when the two beams are collided together at an interaction point. The number of events expected,  $N_{\text{exp}}$ , for an interaction with a cross section  $\sigma_{\text{int}}$  is given by:

$$N_{\text{exp}} = \sigma_{\text{int}} \int \mathcal{L}(t) dt \quad (1.23)$$

where  $\mathcal{L}(t)$  is the instantaneous luminosity. For two beam bunches, with Gaussian momentum and position distributions, containing  $N_1, N_2$  particles colliding with frequency  $f_{\text{rev}}$  and transverse position RMS  $\sigma_{x,y}$ , the luminosity is given by

$$\mathcal{L} = f_{\text{rev}} \frac{N_1 N_2}{4\pi\sigma_x\sigma_y} \quad (1.24)$$

The relation between emittance and luminosity becomes obvious. A lower emittance beam, for a given  $\beta$  function at the interaction point, has lower transverse position RMS and therefore a higher luminosity. This results in more events occurring at the interaction point and therefore a higher data rate.

## 1.2.3 Beam Matching

Another concept related to the phase space ellipse is the *acceptance*. The acceptance is a property of a beamline element, such as a beampipe segment or a magnet. Particles must fall within the acceptance phase space ellipse to be able to propagate through that beamline element. The shape of the acceptance ellipse is governed by the physical size of the beam pipe and the magnetic focussing present.

To pass beams of particles from one beamline element to the next, the phase space of the beam must be matched so that it falls within the acceptance ellipse. The beam is matched through the accelerator by carefully considering the magnetic focussing strength of each

of the magnets present in the focussing lattice. Normally this is done using computational methods as the analytical solutions quickly become far too complex to calculate by hand.

## 1.3 Traditional Cooling Techniques

Many cooling techniques exist and are employed in various particle accelerators. The technique used is dependent on many factors one of which is the particle species being accelerated. A brief description of a few are given below along with the types of accelerator that use them and why they are unsuitable for muon beams.

### 1.3.1 Stochastic Cooling

This technique was conceived by Simon van der Meer [19] and earned him the Nobel prize in physics in 1984. Stochastic cooling played a huge role in the CERN Super Proton Synchrotron (SPS) experiment which supplied  $p\bar{p}$  beams to the UA1 and UA2 experiments that discovered the  $W^\pm, Z$  bosons. It is the main cooling technique used on  $p\bar{p}$  colliders; most notably the Tevatron, enabling the discovery of the top quark.

Stochastic cooling utilises an electromagnetic pick-up and kicker. The pick-up detects the average transverse position of samples of particles in the beam. The size of the samples is governed by the bandwidth of the system. Signals from the pick-up are then amplified and sent to the kicker, which applies an electric field that attempts to correct for the transverse offset of each sample.

Since only small corrections are applied at the kicker, multiple revolutions of the beam through the system are required for significant cooling. Stochastic cooling is therefore not suitable for muon beams since the time scale it operates on are longer than the muon lifetime.

### 1.3.2 Electron Beam Cooling

This method involves introducing a low emittance co-moving electron beam with the particle beam. The particles in the beam then exchange momentum with the electron beam via Coulomb scattering. After multiple passes through the apparatus, the momenta of the particles reaches equilibrium with the electrons and a cooling effect is seen. However due to the incremental nature of this technique, just like stochastic cooling, electron beam cooling is too slow to cool muon beams before significant amounts of muons decay.

### 1.3.3 Synchrotron Damping

Synchrotron radiation can be exploited by accelerators to cool the particle beam. The momenta of particles is reduced due to the radiation emitted as they pass through the magnetic lattice of the accelerator. The longitudinal momentum is then replenished by the RF-cavities. This results in an overall reduction of transverse momentum but the longitudinal momentum remains unchanged, or increases, and therefore a net reduction of  $\epsilon_{\perp}$  is seen.

As was mentioned, muon's high mass makes them unsuitable for this method because of their reluctance to emit synchrotron radiation. According to equation 1.1 protons radiate much less. Therefore this method is only useful for electron beams since they readily emit synchrotron radiation.

## 1.4 Ionisation Cooling

Ionisation cooling is a novel technique that is ideal to reduce the transverse emittance of a muon beam within the muon lifetime. The process can be summarised as follows:

- Pass the particle beam through a material so that the particle's momenta are reduced isotropically i.e both longitudinally and transverse.
- Re-accelerate the particles longitudinally using RF-cavities to restore momentum parallel to the beam direction.
- Repeat until transverse emittance is sufficiently reduced.



Fig. 1.7 Diagram of the main processes in the ionisation cooling technique. The x and y axes show the longitudinal and transverse momenta respectively.

This process is shown diagrammatically in figure 1.7. This process would take place in a cooling channel which is a periodic lattice of absorbers and RF-cavities surrounded by high field solenoid magnets for containment and focussing of the beam. Additionally the figure shows the effect of multiple Coulomb scattering (MCS). Whilst particles lose energy in the absorber material they also undergo scattering. This process will have the undesired effect of

increasing the emittance of the beam if care is not taken in the design of a cooling channel and absorber material.

Normalised transverse emittance can be reduced without the re-acceleration stage, however it is dependent on the absorber material chosen and the beam itself. The amount of heating or cooling a beam experiences is governed by equation 1.25. The rate of change of normalised emittance of a beam is approximately given by [20]:

$$\frac{d\varepsilon_n}{dz} = \underbrace{-\frac{\varepsilon_n}{\beta^2 E} \left\langle \frac{dE}{dz} \right\rangle}_{\text{Cooling}} + \underbrace{\frac{\beta_{\perp}(z)(0.014\text{GeV})^2}{2\beta^3 E m_{\mu} X_0}}_{\text{Heating (MCS)}} \quad (1.25)$$

where  $\beta$  is the relativistic velocity,  $E$  is the total energy of the muons,  $X_0$  is the radiation length of the absorber material,  $\beta_{\perp}(z)$  is the betatron function at the absorber and  $\left\langle \frac{dE}{dz} \right\rangle$  is the mean energy loss per unit length in the absorber material. The negative term labelled ‘‘cooling’’ determines the emittance reduction in the absorber and the positive term labelled ‘‘heating’’ estimates the emittance growth from MCS processes. By setting the left hand side to zero and rearranging for  $\varepsilon_n$ , the equilibrium emittance,  $\varepsilon_{\text{eq}}$ , can be calculated via:

$$\varepsilon_{\text{eq}} = \frac{\beta_{\perp}(z)(0.014\text{GeV})^2}{2\beta m_{\mu} X_0} \left\langle \frac{dE}{dz} \right\rangle^{-1} \quad (1.26)$$

Beams with  $\varepsilon_n$  above the equilibrium emittance are cooled when passed through the absorber and beams with a lower emittance are heated due to the MCS processes dominating. It is favourable for a cooling channel to have a low  $\varepsilon_{\text{eq}}$ . To achieve this the betatron function at the absorber needs to be small by strongly focussing the beam into the absorber. Furthermore the product  $X_0 \left\langle \frac{dE}{dz} \right\rangle$  must be large. This dictates the choice of absorber material to one with a low proton number,  $Z$ , the ideal candidates being liquid hydrogen ( $\text{LH}_2$ ) or Lithium Hydride ( $\text{LiH}$ ) with the latter being much easier to work with considering it is solid at room temperature and therefore does not require a cryostat. Both of these absorbers are tested in the MICE experimental programme.

## 1.5 Conclusion

Both neutrino factories and muon colliders enable precise measurements of the Standard Model’s parameter space along with the elements of the PMNS matrix. Furthermore muon accelerators offer the prospect of multi TeV lepton colliders, with small footprints, that can be used to search for beyond standard model physics at the high energy scale.

However the technology required to build muon accelerators is not yet tried and tested. The major issue is reducing the emittance of the tertiary muon beam to a point where it is usable. Ionisation cooling is proposed as the initial cooling method for muon accelerators; the Muon Ionisation Cooling Experiment (MICE) aims to demonstrate it.



## Chapter 2

# The Muon Ionisation Cooling Experiment

Although the theory of ionisation cooling is well established, the technique has never been implemented. To make muon accelerators a possibility, a cooling channel capable of ionisation cooling must be constructed and proven to work. Furthermore the ability to produce accurate computer models of particle beams passing through cooling channels is desirable as it will enable the designs of future channels to be refined.

The Muon Ionisation Cooling Experiment is based at the Rutherford Appleton Laboratory (RAL) in the United Kingdom and is operated by an international collaboration. The goal of MICE is to measure a  $\sim 10\%$  reduction in the transverse emittance of a muon beam with an absolute precision of 0.1%, using ionisation cooling implemented with a realistic cooling channel [21]. Another aspect of the experiment is to produce analysis and modelling software which enables Monte Carlo simulations of the cooling channel which matches the data as much as possible.

MICE is a unique accelerator experiment that is made up of many components and detectors, with some being recycled from former particle physics experiments. During MICE's operational lifetime, it has undergone various redesigns. This thesis will focus on the final stage only, known as Step IV<sup>1</sup>.

The step IV set-up is designed to perform ionisation cooling without any re-accelerating structures. This step also serves as a test bed for multiple coulomb scattering studies with  $\text{LH}_2$  or  $\text{LiH}$  absorbers. Figure 2.1 shows the basic outline of MICE step IV.

This chapter gives a summary of the experiment, including hardware components and software for analysis.

---

<sup>1</sup>This step is the final stage to be operated.

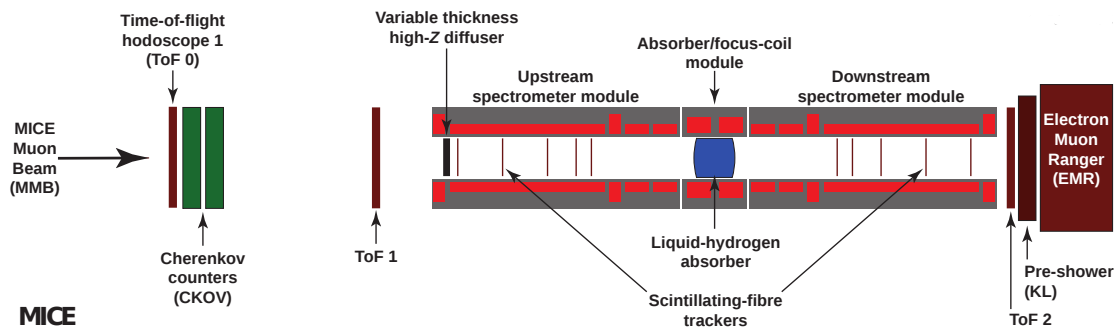


Fig. 2.1 A schematic of MICE Step IV showing the main detectors and the cooling channel in relation to the muon beam. The red boxes in the spectrometer and focus coil modules show the superconducting magnet coils.

## 2.1 MICE Hardware

The hardware for MICE can be categorised into three elements:

1. The beam line that supplies a muon beam for the experiment.
2. The cooling channel that will perform ionisation cooling.
3. The detectors for particle identification (PID), emittance measurement and beam characterisation.

Any detectors present in the beamline or cooling channel are described in 2.1.3.

### 2.1.1 MICE Muon Beamline

The MICE muon beamline is an offshoot of the ISIS synchrotron. It consists of the pion production target, magnets for beam transfer and detectors for beam characterisation. A schematic of the beamline is shown in figure 2.2.

#### 2.1.1.1 ISIS

ISIS is a pulsed proton synchrotron with a peak energy of 800 MeV. Its official purpose is a spallation neutron and muon source for material science experiments.

To achieve this, protons are accelerated, extracted and then fired into a tungsten or carbon target for neutrons or muons respectively. First  $H^-$  ions produced by an ion source are accelerated to 70 MeV by a radio frequency quadrupole (RFQ) and then a linac. The ions are then injected into the synchrotron and passed through a thin aluminium oxide foil, stripping the electrons and leaving bare protons. Continued acceleration of the protons then occurs in

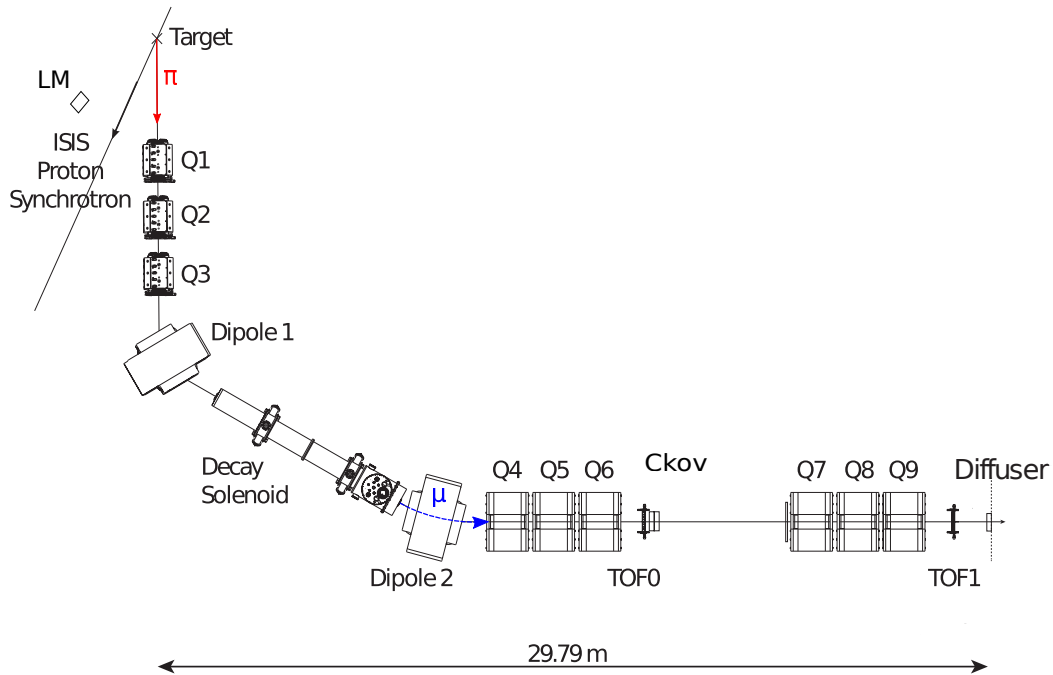


Fig. 2.2 Diagram showing the MICE muon beamline. Q denotes a quadrupole magnet, TOF denotes a time of flight detector, Ckov denotes the Cherenkov detectors and LM denotes the luminosity monitor.

the synchrotron ring by means of RF cavities up to 800 MeV which takes approximately 10 ms. At this point the beam is extracted to the two target stations for use in experiments. This whole process repeats 50 times a second.

The muon beam for MICE is first derived from a pion beam. Pions are produced by the target mechanism which acts as the interface between ISIS and MICE.

### 2.1.1.2 Target Mechanism

The target itself consists of a hollow cylinder of titanium which is dipped into the halo of the ISIS beam when its energy is roughly at maximum. It typically operates at a rate of one actuation per second. In numbers this means that the target must move a minimum distance of 24 mm to reach the halo of the beam in the last 1-2 ms of the acceleration phase. The target must then travel back and be held out of the beam before the next pulse is injected [22]. Furthermore the target must preserve the high vacuum conditions of the beam pipe. The shower of particles released from one actuation of the target is known as a “spill”.

To fulfil these requirements the target mechanism employs a linear motor to move the titanium shaft in and out of the beam. The motor is comprised of a stack of coils forming the stator and neodymium-iron-boron permanent magnets fixed to the shaft. This arrangement

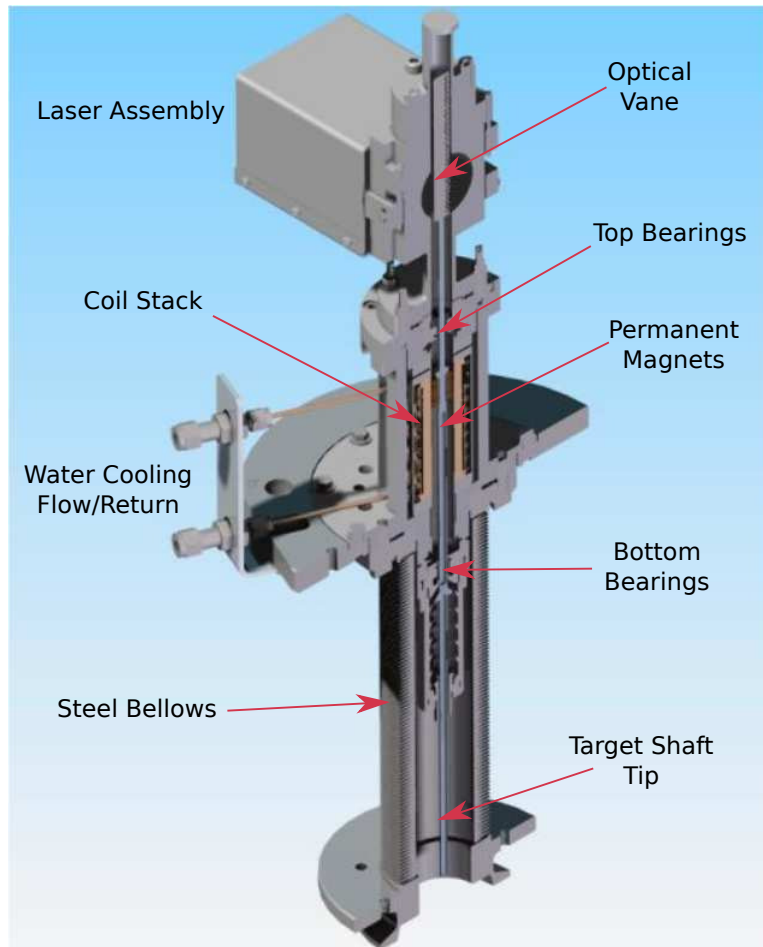


Fig. 2.3 Cutaway view of the MICE target mechanism. When the frame is lowered, the steel bellows are compressed. Figure adapted from [22].

allows accelerations of up to  $\sim 780 \text{ ms}^{-2}$ . The bearings are made from VESPEL<sup>®</sup>, an advanced polymer that is hard wearing and has low coefficient of friction. This in conjunction with a diamond like carbon (DLC) coating on the contact points of the target shaft ensures that friction is minimal and the lifetime of the target is maximised. The full target mechanism is shown in figure 2.3.

The target mechanism is attached to a frame that allows it to be lowered and raised via a stepper motor. When the mechanism frame is raised, the target shaft is allowed to rest on the bottom bearings as it sits well out of the ISIS beam pipe. When lowered, the target shaft must be magnetically levitated by the coils so that it sits out of the particle beam. In the lowered state the target is then dipped into the ISIS beam to provide pions for the MICE beamline.

A Field Programmable Gate Array (FPGA) based controller dictates the currents supplied to the coil stack to perform dipping and magnetic levitation of the shaft. Position of the target

shaft is measured using an optical quadrature system consisting of three lasers that are passed through an optical vane – a thin piece of metal with periodic slits cut into it.

### 2.1.1.3 Conventional Magnets

Conventional magnets are used to transport the beam from the target area in the synchrotron hall to the MICE hall and ultimately to the cooling channel. Eleven conventional magnets form the transport line. Nine of these are quadrupole magnets, Q1-9, arranged in triplets to focus and contain the beam. Lastly two dipole magnets, D1 and D2, bend the beam into the MICE hall.

The first quadrupole triplet (Q1-3) captures pions from the target and transports them into D1. The other two quadrupole triplets (Q4-6, Q7-9) transport and focus the beam into the cooling channel.

The dipole magnets also serve as a beam selection tool. Firstly, different momenta beams can be selected by adjusting the field in the magnets. Secondly beams of different particle species composition can be chosen to perform different tasks. For instance, a high purity muon beam can be formed by using a field at D2 that is roughly half that of D1 so that the backwards decaying muons in the pion rest-frame are selected. This beam is used for ionisation cooling data taking. Alternatively if the field at D2 is roughly equal to D1, a beam that is composed of pions, muons and electrons can be selected. This mixed beam mode is useful for calibrating detectors since it has a much higher particle rate. The pion contamination of the muon beam mode has been measured to be  $\sim 1\%$  [23].

### 2.1.1.4 Decay Solenoid

Between the two dipoles sits a superconducting solenoid magnet called the decay solenoid (DS). The high field, typically 5 T, in the DS causes pions from D1 to follow helical trajectories. Its primary purpose is to contain the divergent pion beam that emerges from D1. Moreover, the induced helical trajectory increases the pion's path length that allows them some more time to decay into muons.

### 2.1.1.5 Proton Absorber

Exiting the decay solenoid, the beam is passed through the proton absorber. This consists of four sheets of borated polyethylene with thicknesses of 15, 29, 49 and 54 millimetres. These sheets can be individually placed into or out of the beam, enabling protons to be removed for various momentum settings. The proton absorber is only needed if the polarity of the beam is chosen to be positive, otherwise all sheets are placed out of the beam.

### 2.1.1.6 Diffuser

Along with multiple momentum beams, it is desirable to test beams with different input emittances. This is done by exploiting the heating term of the cooling equation. By passing the beam through material with a short radiation length the emittance can be increased appropriately. The diffuser achieves this by employing four irises of different thicknesses and material, see table 2.1. Each iris can be independently opened/closed to allow various input emittance beams to be produced. The irises are pneumatically operated since the diffuser sits next to the upstream spectrometer solenoid that produces large magnetic fields. By having different combinations of irises open or shut, the diffuser allows a maximum of 3 radiation lengths in steps of  $0.2 X_0$  to be inserted into the beam.

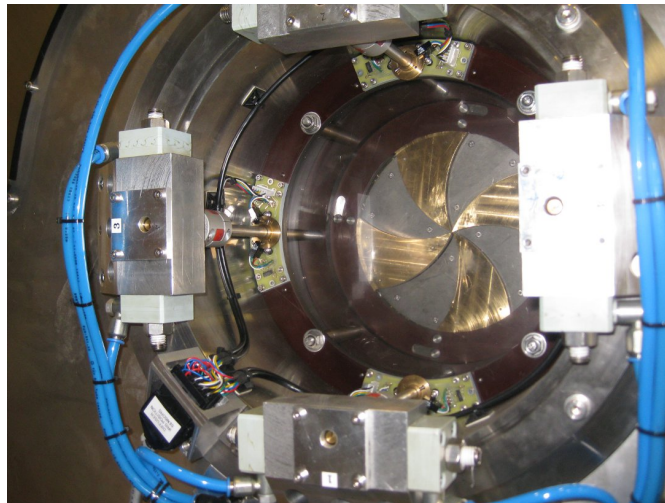


Fig. 2.4 Photograph of the diffuser with closed irises shown as it is installed inside the bore of the upstream spectrometer solenoid.

The diffuser and the dipole magnets allow beams with different input emittance and momentum to be selected. The beam settings are referred to by their nominal longitudinal momentum and emittance, just after the diffuser, measured in MeV/c and  $\pi$  mm·rad respectively. For instance a 6-200 beam is one that has an initial emittance of  $6 \pi$  mm·rad and a mean longitudinal momentum of 200 MeV/c.

### 2.1.2 Cooling Channel

Technically the cooling channel is only the absorber focus coil module, as this is where the emittance reduction happens. This is the part that would be repeated, along with RF-cavities, in a real cooling channel for a muon accelerator. For ease of reference, in this thesis the

Iris	Material	Thickness [mm]	Equivalent Radiation Length
1	Brass	2.97	$0.2 X_0$
2	Brass	5.94	$0.4 X_0$
3	Tungsten	2.80	$0.8 X_0$
4	Tungsten	5.60	$1.6 X_0$

Table 2.1 Table of diffuser iris parameters.

cooling channel will refer to the equipment necessary to perform the ionisation cooling and measure the emittance before and after.

The step IV cooling channel is comprised of two spectrometer solenoids (SS) with an absorber focus coil (AFC) in between. The two spectrometer solenoids are referred to as SSU and SSD, where ‘U’ and ‘D’ denote upstream and downstream with respect to the beam. The layout of the channel is shown in figure 2.5.

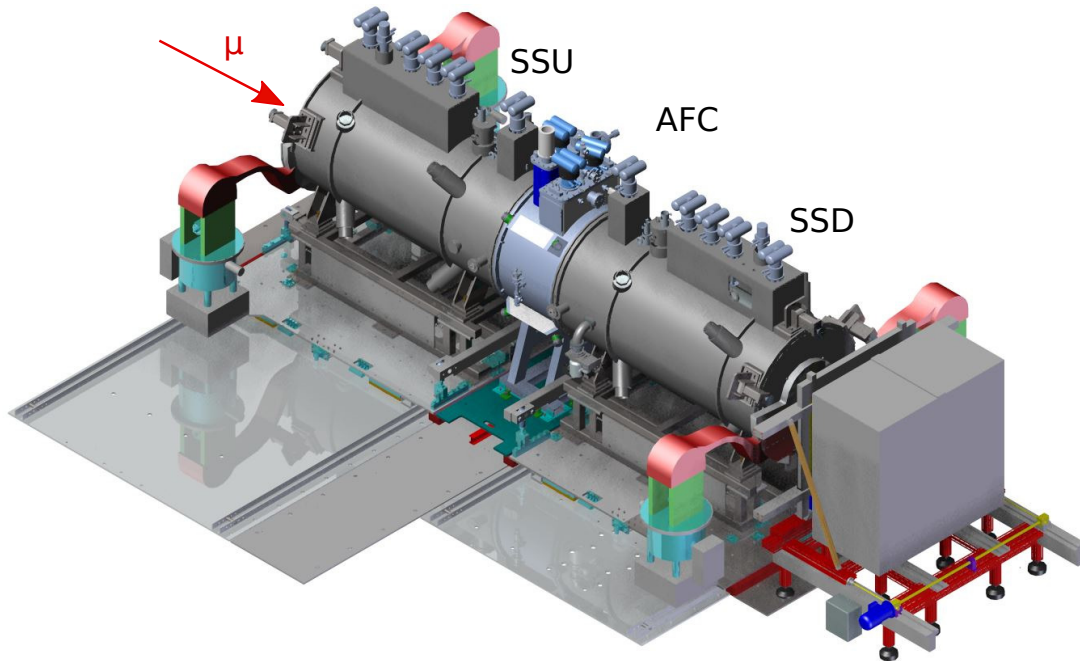


Fig. 2.5 Labelled rendering of the step IV cooling channel set-up. The direction of the muon beam is shown by the red arrow. The large box at the downstream end is the EMR detector.

The cooling channel can be operated in two modes – “solenoid” and “flip” mode. In solenoid mode all the coils are operated with the same polarity. In flip mode, all coils downstream of the absorber are operated with the opposite polarity to the others. As the beam travels through the fringe fields of a solenoid, where there are radial field components, particles that are off the axis receive an azimuthal kick. This kick gives the particles angular momentum, of which a build up can make the beam harder to focus [24]. To reduce this

build up the polarity of the solenoid magnets in the channel are alternated, like in flip mode, so that the azimuthal kicks are opposite.

### 2.1.2.1 Spectrometer Solenoids

The spectrometer solenoids host the scintillating fibre trackers that perform the emittance measurement. Each SS consists of five superconducting coils made from Niobium-Titanium (NbTi). These coils are known as Match Coil 1, Match Coil 2, End Coil 1, End Coil 2 and the Centre Coil. These names will be abbreviated to M1, M2, E1, E2 and CC in this thesis.

The trackers sit within the field of the centre coil so that traversing particles undergo helical paths meaning that their transverse momenta can be measured. The currents in the two end coils can be tuned so that the field in the tracker region is uniform allowing the betatron function to be flat as shown in figure 2.6. The two match coils are tuned to allow the beam to be matched into and out of the absorber.

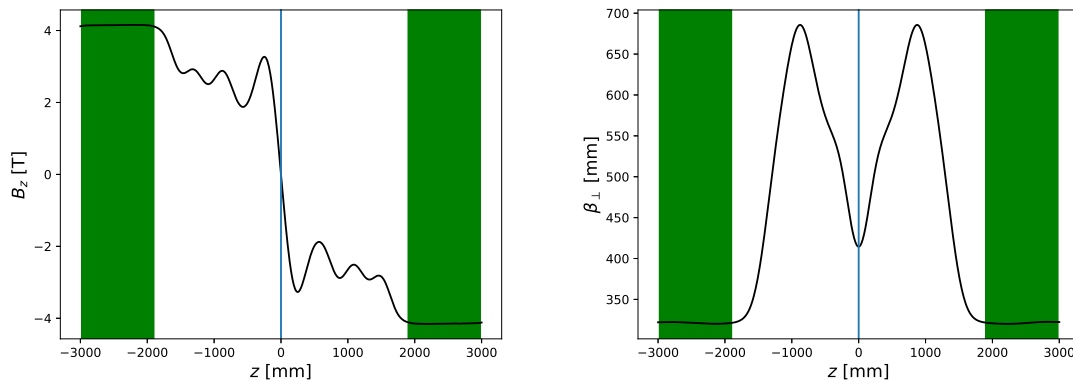


Fig. 2.6 Plots showing the axial field (left) and transverse betatron function (right) as a consequence of the cooling channel magnets operated in flip mode. The blue line shows the location of the centre of the absorber and the green regions show where the trackers are situated.

The spectrometer solenoids will be discussed in greater detail in section 3.2 as they are the prime subject of this thesis.

### 2.1.2.2 Absorber Focus Coil

The absorber focus coil (AFC) module hosts the absorber material. The cooling equation, shown in section 1.4, dictates that cooling is maximised when the betatron function is small in the absorber. To achieve this the AFC employs superconducting solenoids to focus the beam thus reducing the betatron function. Superconducting solenoids are ideal for focussing

in cooling channels because they focus the beam in both transverse directions and as such are far more space efficient than quadrupole triplets. The focussing length,  $f_{\text{sol}}$ , of a solenoid is given by

$$\frac{1}{f_{\text{sol}}} = \int \left( \frac{eB_s}{2p} \right)^2 ds \quad (2.1)$$

where  $e$  is the charge of the particle,  $s$  is the coordinate along the nominal beam axis,  $B_s$  is the axial component of the solenoid field and  $p$  is the momentum of the particles in the beam. As the focussing length is proportional to the square of the momentum, solenoids are only suitable for focussing lower momentum beams which are typical for ionisation cooling channel designs [25]. The effect of the AFC on the betatron function can be seen in the right hand plot in figure 2.6. Focussing solenoids cause  $\beta_{\perp}$  to be at a local minimum at the centre of the absorber.

Figure 2.7 shows a cutaway drawing of the AFC module. When operated with LH<sub>2</sub>, an insulating vacuum space between the absorber windows and safety windows is required. The safety windows are made as thin as possible to avoid any undesirable emittance growth.

### 2.1.2.3 Absorber Material

As mentioned in section 1.4, the two primary absorbers that are used in the MICE experimental programme are liquid hydrogen and lithium hydride as they exhibit the ideal properties according to the cooling equation. These properties are summarised in table 2.2. The liquid hydrogen is contained inside a 21 litre aluminium vessel which sits inside the focus coil. The lithium hydride absorber consists of a disk with a thickness of 65 mm.

Material	$X_0$ [g cm <sup>-2</sup> ]	$\langle \frac{dE}{dx} \rangle$ [MeV g <sup>-1</sup> cm <sup>2</sup> ]	$\epsilon_{\text{eq}}$ [mm·rad]
LH <sub>2</sub>	63.04	4.103	1.71
LiH	79.62	1.897	2.93

Table 2.2 Table of radiation length, mean energy loss and equilibrium emittance for the MICE absorbers. Numbers from [26]. Equilibrium emittance calculated from equation 1.26 for a typical 200 MeV/c momentum beam with  $\beta_{\perp} = 42$  cm as is the case for the cooling channel field shown in figure 2.6.

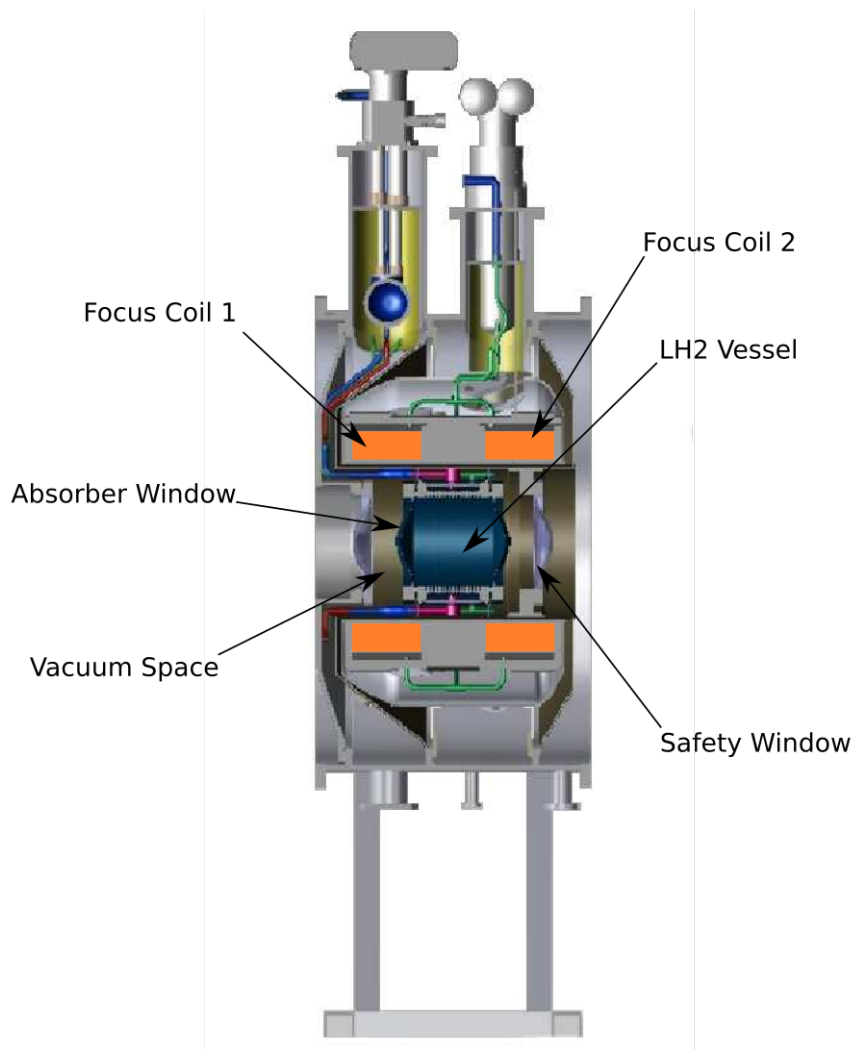


Fig. 2.7 Labelled cutaway drawing of the absorber focus coil module when it is operated with liquid hydrogen.

### 2.1.3 Detectors

MICE hosts a variety of detectors along the beamline tasked with particle identification, emittance measurement, beam characterisation and calorimetry.

As mentioned in section 2.1.1, the MICE beamline has the necessary equipment to select almost pure muon beams but some contamination is inevitable. Particle identification (PID) is an important aspect for the MICE experiment, as such there are multiple detectors tasked with PID: the time of flight detectors; the Cherenkov detectors; the KLOE-light and EMR detectors. The emittance measurement is carried out by the two scintillating fibre trackers.

This section gives a brief overview of each detector, how they work and what their role is.

### 2.1.3.1 Luminosity Monitor

The ISIS accelerator has argon based ionisation chamber detectors installed around its inner ring. They detect particles originating from stray protons interacting with the accelerator components, acting as beam loss monitors (BLM). The signal from the BLMs in the vicinity of the target is used as a guide when decided how deep the target should be dipped into the ISIS beam. However due to their size and positioning they sample a large part of the accelerator and therefore are not useful in determining the particle rate for the MICE beamline. Instead there is a luminosity monitor (LM) installed near the target, shown in figure 2.2.

The LM is positioned at roughly the same angle and height as the beamline formed by the first three quadrupoles but on the opposite side of the synchrotron. This is so that it samples the particle rate that would go through the beamline without being an obstruction. Its primary use was to validate Monte Carlo beam generation routines [27].

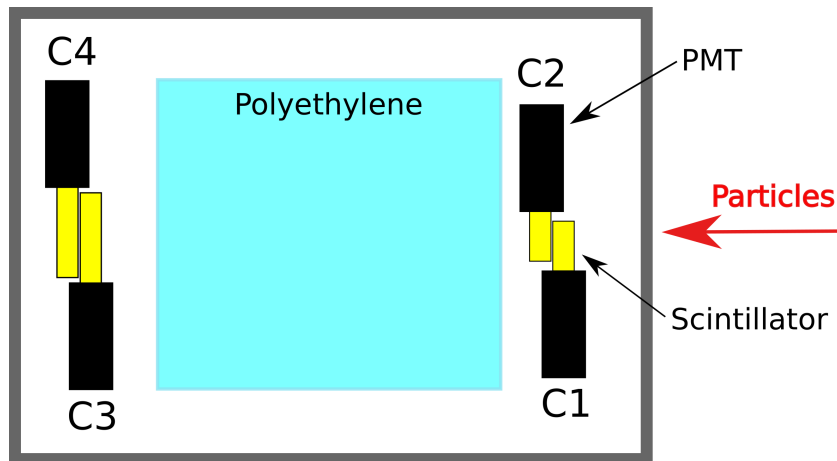


Fig. 2.8 Labelled diagram showing the design of the luminosity monitor.

The design of the LM is shown in figure 2.8. It consists of four blocks of scintillator that are read out by low noise photomultiplier tubes (PMTs) arranged in two pairs either side of a 15 cm wide polyethylene block. The polyethylene absorbs protons with momenta  $\lesssim 500$  MeV and pions with momenta  $\lesssim 150$  MeV. Three coincidence signals are recorded from the four PMTs: one from the first pair (C12); one from the second pair (C34) and finally a coincidence signal from all four PMTs (C1234).

### 2.1.3.2 Time of Flight Detectors

The primary PID detectors are the time of flight (TOF) detectors of which there are three, named TOF0, TOF1 and TOF2. Figure 2.2 shows the position of TOF0 and TOF1. TOF2 is placed downstream of the cooling channel and before the KL and EMR detectors. By

measuring the time it takes for a particle to travel between the detectors, and precisely knowing the distance between the detectors and the momentum selected by D2, the particle species in the beam can be identified. The TOFs ability to discriminate particle species is shown by the histograms in figure 2.9. They also double up as a tool to measure the longitudinal momentum of the beam. This set-up allows particle species to be identified upstream and downstream of the cooling channel. When MICE was to be operated with RF-cavities<sup>2</sup>, the time measurement from the TOF detectors determined the phase of the cavity's oscillating accelerating field, ensuring the beam is accelerated.

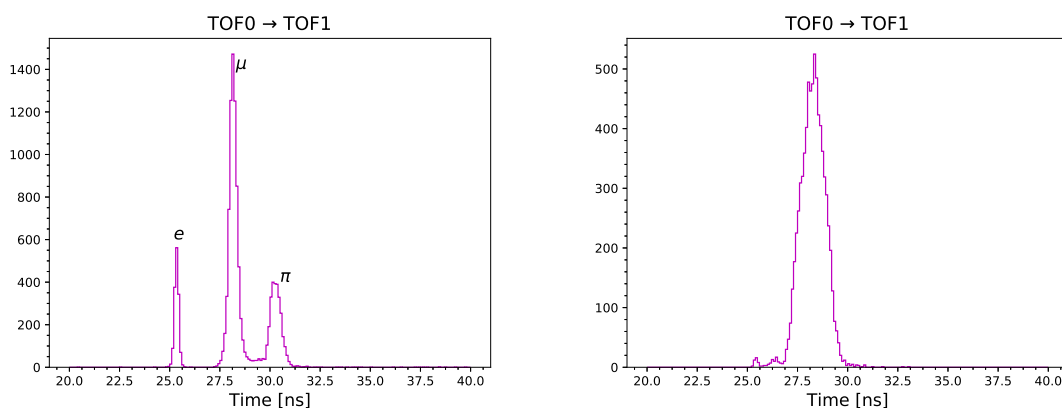


Fig. 2.9 Time of flight histograms for two measured 200 MeV beams. The abscissa is the time taken to travel between TOF0 and TOF1. The left plot shows a mixed beam; the electron, muon and pion peaks are clearly separated and labelled. The right plot shows a muon beam with a broader peak and a slight electron peak.

The TOF detectors are scintillator based hodoscopes, allowing the transverse position of the impinging particles to be determined. A photograph of TOF1 is shown in figure 2.10. All three detectors consist of two planes made up of 1 inch thick bars of scintillator which are arranged horizontally in one plane and vertically in the other, forming pixels. Therefore they also act as a rudimentary beam profile monitor. Both ends of the bars are read out by Hamamatsu R4998 fast PMTs [28]. By considering the time difference between the signals in both PMTs, a more precise measurement of the position can be made.

Whilst the TOFs share the same design principle, there are a few differences between each individual detector; their key parameters are summarised in table 2.3. Iron shielding is placed around the PMTs of TOF1 and TOF2 to protect them against any stray magnetic field originating from the spectrometer solenoids.

<sup>2</sup>As of time of writing this is no longer going to happen.

Parameter	TOF0	TOF1	TOF2
Active Area [cm <sup>2</sup> ]	40 × 40	42 × 42	60 × 60
Bar Width [cm]	4	6	6
Scintillator	BC-420	BC-404	BC-404
Time Resolution [ps]	52.2 ± 0.9	59.5 ± 0.8	52.7 ± 1.1

Table 2.3 Table showing the key parameters for all three TOF detectors.

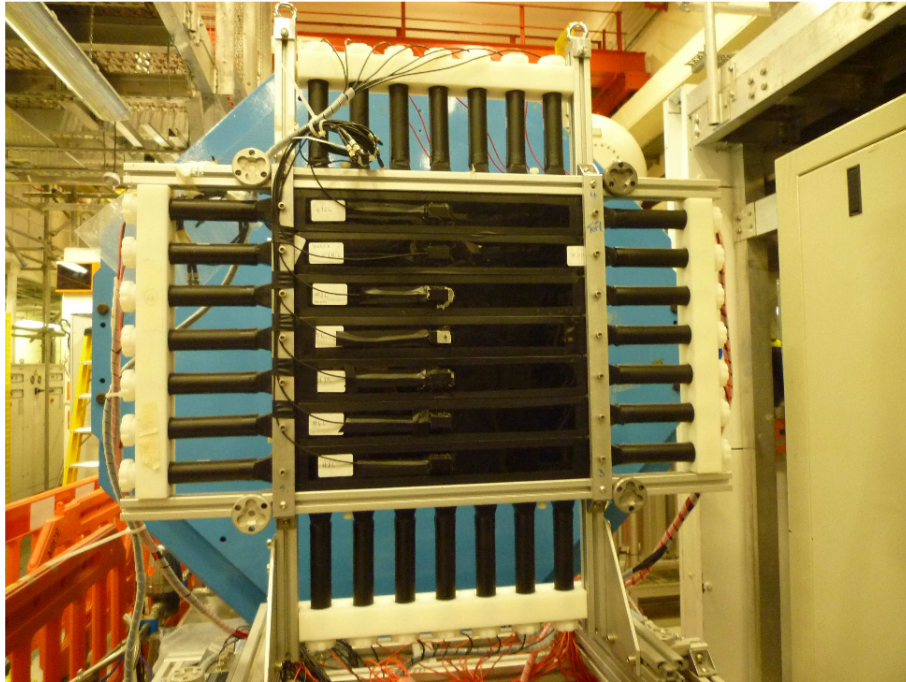


Fig. 2.10 Photograph of TOF1 installed in the MICE beamline. The plane with horizontal slabs is shown. The black cylinders are the PMTs. Also shown are the laser injection prisms, stuck onto the faces of the bars, that are used for calibration. Picture from [29].

### 2.1.3.3 Cherenkov Light Detectors

To complement the TOF detectors there is a pair of Cherenkov light (Ckov) detectors. Threshold Cherenkov detectors are widely used for particle identification due to their mode of operation. Charged particles emit a cone of Cherenkov light when they travel through a medium faster than the speed of light in that medium. This light can then be converted into a signal using PMTs. By picking the refractive index of the medium carefully, and therefore the threshold velocity, particles of different masses but equal momenta can be distinguished from each other.

The pair of Ckov detectors, known as CkovA and CkovB, have different threshold velocities that allow them to distinguish between pions and muons that have the same

momentum. Both use high density aerogel as the medium with refractive indices of 1.07 and 1.12 for Ckov A and B respectively [30]. Table 2.4 illustrates which particle species produce signals in the detectors for the three momentum settings that MICE uses. Note that for the 140 MeV/c beam, only electrons are above threshold meaning that the TOFs are relied upon for distinguishing between pions and muons.

Beam Momentum [MeV/c]	Signal in CkovA	Signal in CkovB
140	$e$	$e$
200	$e$	$e, \mu$
240	$e, \mu$	$e, \mu, \pi$

Table 2.4 Table showing which particle species are above the threshold velocity for both Cherenkov detectors for the three primary MICE beam momenta.

An exploded view of the MICE Cherenkov detectors is shown in figure 2.11. The aerogel is surrounded by mirrors one of which is shaped like a pyramid to reflect light into the four PMTs that detect the Cherenkov light and convert it into a signal.

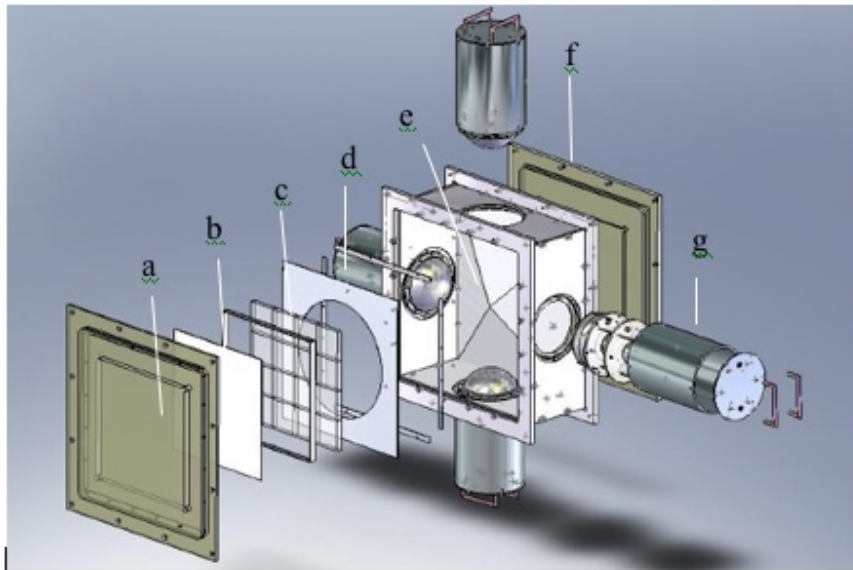


Fig. 2.11 Labelled exploded view of the MICE Cherenkov detectors: a) and f) are the entrance/exit windows, b) mirror, c) aerogel, d) acetate window e) reflector panel and g) photomultiplier tube. Figure from [31].

#### 2.1.3.4 Scintillating Fibre Trackers

The emittance of the beam is measured upstream and downstream of the absorber by two scintillating fibre trackers, labelled TkU and TkD respectively. They sit inside the two

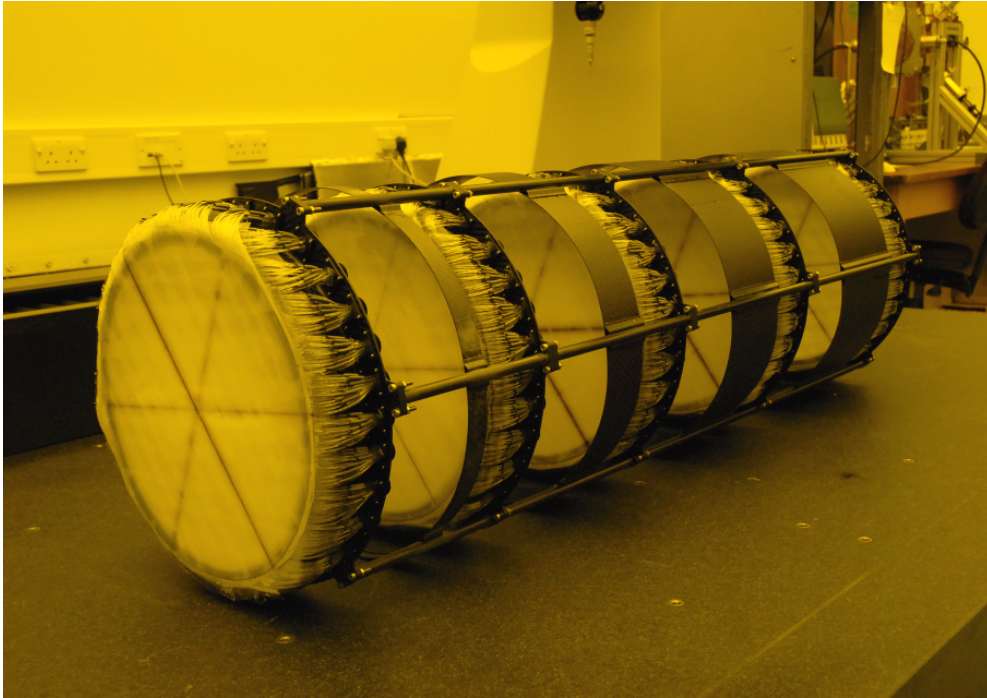


Fig. 2.12 Photograph of one of the scintillating fibre trackers. The five stations are shown and the black lines on each station mark the orientation of the three planes of fibres.

spectrometer solenoids within the centre coil region, as discussed earlier. The downstream tracker is rotated  $180^\circ$  with respect to the upstream tracker so that they are mirrored across the centre of the absorber, as shown in figure 2.1.

Both trackers comprise of five circular stations, shown in figure 2.12, with a radius of 15 cm and the two end stations are 1.1 m apart. The five stations have unequal separation between them to ensure that the azimuthal motion of the particles is sampled at different phases of rotation. The stations are labelled 1-5 with station 1 always being the closest to the absorber for both trackers.

Each station supports three doublet layers of  $350 \mu\text{m}$  diameter scintillating fibres, shown in figure 2.13, that are glued together with a protective mylar layer. These three doublet layers, labelled as  $u, w$  and  $v$ , are arranged such that they are rotated by  $120^\circ$  to each other as shown in figure 2.13. The fibres in the doublet layers are grouped in channels consisting of seven adjacent fibres. Three overlapping channels then form a triangular pixel allowing a position resolution of  $\sim 470 \mu\text{m}$  [32].

Light from each channel is collected by wave guides that run out of the spectrometer solenoid bore and into cassettes of visible light photon counters (VLPCs) which form the signals that are read out by the DAQ. The VLPCs are kept cold at 9 K in liquid helium cryostats to reduce thermal noise.

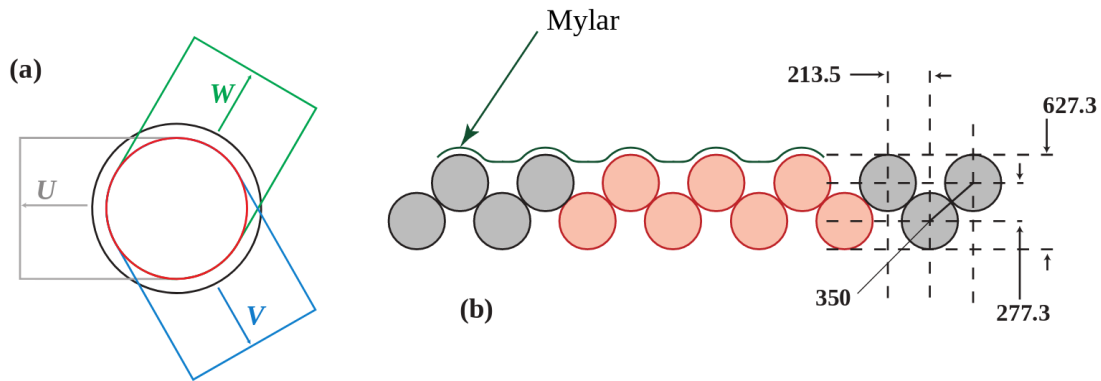


Fig. 2.13 Diagram showing the arrangement of the tracker fibre doublet layers. Diagram a.) shows how the three layers are arranged on each station. Diagram b.) shows a cross section of a doublet layer. The seven fibres highlighted in red compose a single channel. Dimensions are in  $\mu\text{m}$ .

### 2.1.3.5 KLOE-Light Detector

As mentioned, additional PID is carried out downstream of the cooling channel. Whilst the first two TOFs, along with the Cherenkov detectors, are designed to identify muons before they enter the cooling channel; some muons will inevitably decay into electrons (and neutrinos) which will continue to propagate down the beam line.

The KLOE-Light (KL) detector is tasked with identifying decay electrons. It is known as the KLOE-Light detector because it is a smaller version of the electromagnetic calorimeter used on the KLOE experiment [33] and its design is adjusted for the lower particle energies present in MICE.

The KL is a sampling calorimeter with scintillating fibres acting as the active component and extruded lead foil for the showering material with a scintillator:Pb ratio of  $\sim 2:1$  by volume. The layout of the fibre and lead foil is shown in figure 2.14. Layers of the lead-scintillator matrix are arranged into modules with each module divided into three cells which are read out at both ends by PMTs with the light collected from multiple fibres by Winston cone light guides, as shown in figure 2.15. The KL is then made up of seven modules, arranged horizontally, giving an active volume of  $93 \times 93 \times 4 \text{ cm}^3$ .

The KL is designed to cause electrons to shower within it; allowing the measurement of their time and energy with resolutions of  $\Delta t \approx 70 \text{ ps}/\sqrt{E}$  and  $\Delta E/E \approx 7\%/\sqrt{E}$ . These pre-showers then impinge on the electron muon ranger detector, which sits downstream of the KL.

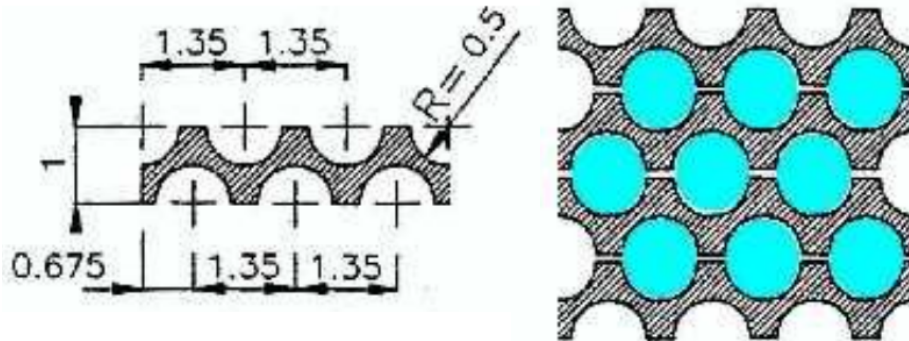


Fig. 2.14 Cross sectional diagram showing the arrangement of the lead foil and scintillating fibres in the KL detector. Dimensions shown are in millimetres. The right hand diagram shows how the layers are stacked, with the blue regions representing the scintillator. Figure from [31].

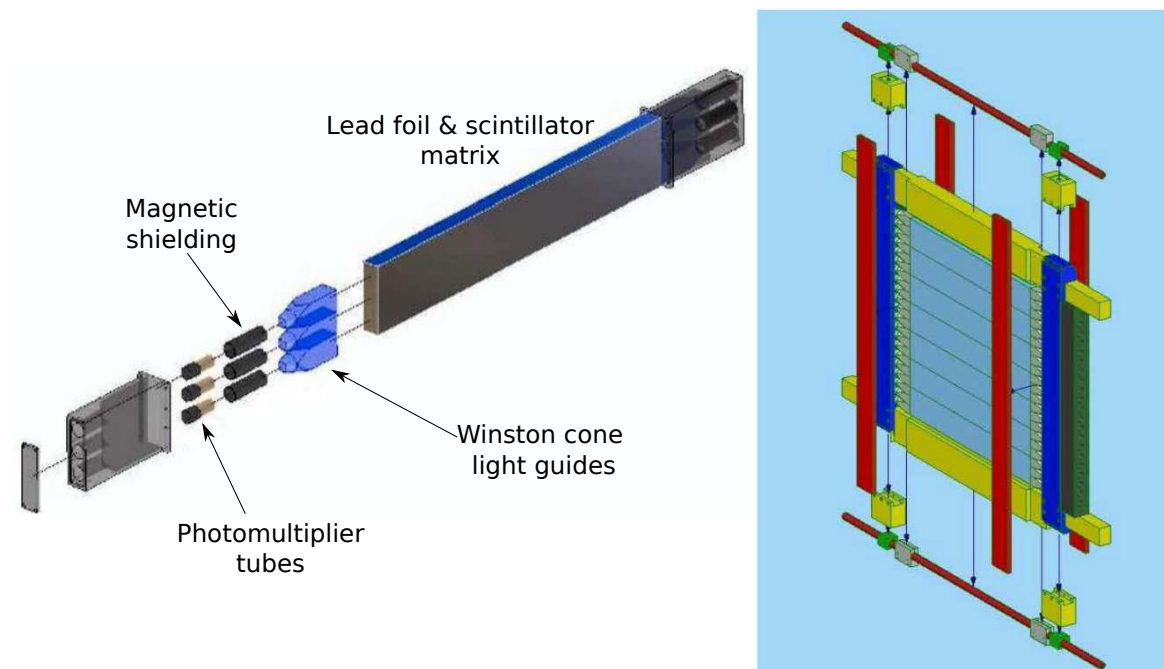


Fig. 2.15 Labelled exploded view of one KL module on the left. On the right is a rendering of the whole KL detector showing how the seven modules are arranged. Figure adapted from [31].

### 2.1.3.6 Electron Muon Ranger

The last detector in the MICE beam line is the electron muon ranger (EMR). The EMR is a fully active calorimeter with particle tracking functionality. As with the KL detector, it is tasked with identifying decay electrons in the beam. It is also designed to measure the range of muons passing within the detector allowing an estimate of their momenta.

The EMR is made up from triangular prism shaped scintillator bars with wave length shifting fibres running down the centre. The scintillator bars are then tessellated together to form square planes with each plane containing 59 bars and covering an area of  $1.27 \text{ m}^2$  [34]. The full detector is then made up of 48 planes with alternating planes stacked at  $90^\circ$  with respect to the last, thus allowing a position measurement along the two axes that are transverse to the beam axis.

For each plane both ends of the 59 fibres are grouped together and read out by a single PMT. For one side, all fibres are read out by a single-anode PMT (SAPMT); and the other side they are read out by a 64-channel multi-anode PMT (MAPMT). This set-up allows the SAPMTs to measure the total energy deposited in one module and the MAPMTs to measure energy deposition in each individual bar. Figure 2.16 shows the arrangement of the bars and planes that make up the EMR detector.

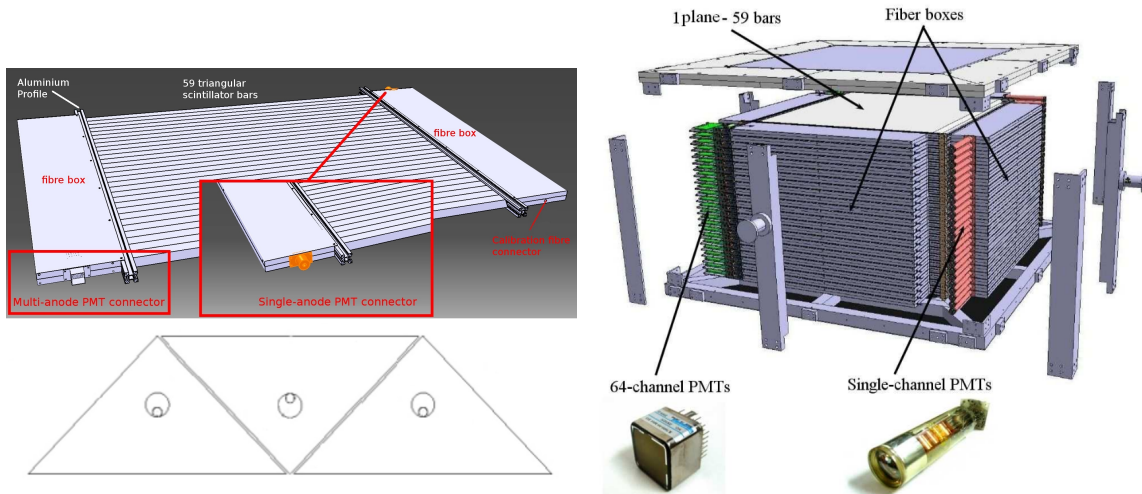


Fig. 2.16 The left hand drawings [35] show how the triangular scintillator bars build up a plane of the EMR. The right hand figure [36] is an exploded drawing showing how the planes constitute the full detector. Also shown are examples of the two types of PMT that the EMR utilises.

Figure 2.17 shows two event displays from the EMR detector. Muons can be distinguished since they leave a straight track with secondary tracks from their decay electrons/positrons.

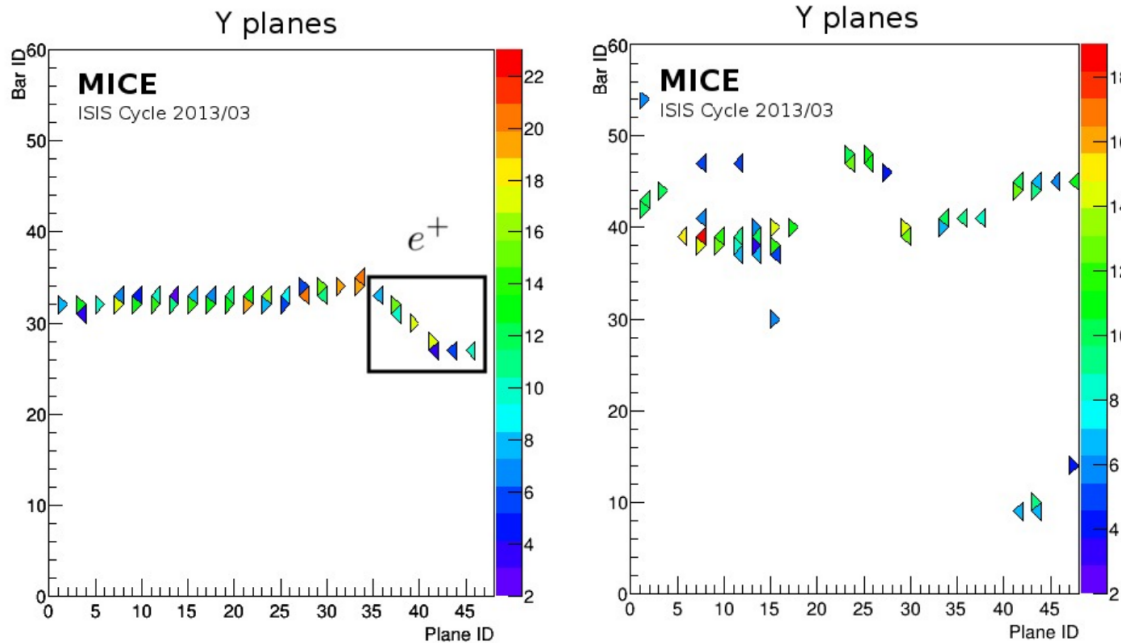


Fig. 2.17 Plots showing a muon decay (left) and an electron shower event (right) in the Y-plane of the EMR detector. The colour is proportional to the energy deposited. Plots adapted from [35].

Electrons present within the beam can be distinguished because they shower within the KL, and these showers are imaged by the EMR.

## 2.2 MICE Software

### 2.2.1 MICE Analysis User Software

Software for simulation, data reconstruction and analysis is provided by the MICE Analysis User Software (MAUS), which is written in a combination of C++/python and follows a Map-Reduce style of data flow to enable efficient parallelisation [37].

MAUS enables simulations of the MICE experiment to be performed with the ability to generate beams, starting from D2, of different energy and initial emittances. Beam generation is handled by the G4beamline package [38] and particle tracking through matter and simulating physics processes, such as scattering, is handled by the Geant4 package [39]. Simulated particle tracks are then converted into detector hits by custom digitisation routines for all detectors in the MICE beamline. These detector hits are then reconstructed by the same routines that reconstruct the raw data from the DAQ.

MAUS takes the raw data from the DAQ and reconstructs them into detector hits. These detector hits are then fed into track fitting and global reconstruction algorithms so that the transverse phase space of the particles can be determined. Reconstructed data is then output into a ROOT [40] file for further analysis, such as emittance calculations.

Reconstruction of raw data can also be performed whilst data taking is occurring. Histograms and detector event displays are then available for viewing to diagnose any problems whilst the experiment is operational to ensure data quality.

### 2.2.2 Configuration Database

MICE is a constantly evolving experiment. Each time the specifications change, the absorber material is swapped out, the equipment/detectors are moved or the calibration of a detector is altered, the changes are logged into the MICE configuration database (CDB).

The CDB is an online MySQL database that allows users to obtain the geometry files of the experiment for any of the data taking runs so that Monte Carlo simulations may be performed with the same set-up as the true data. Along with the physical geometry of the beamline, detectors and cooling channel, the CDB also stores the currents of all magnets present on the experiment.

### 2.2.3 Controls, Monitoring and DAQ

The control and monitoring of the detectors and hardware is centralised within MICE run control. MICE run control integrates the EPICS [41] framework with DATE<sup>3</sup> [42] data acquisition software. It allows beam settings to be selected at the click of a button and adjusts the diffuser and beamline magnets accordingly whilst also arming the DAQ. Run control also monitors the operating parameters of all the hardware components and alerts the user if something is wrong via the alarm handler, allowing any problems to be quickly diagnosed.

The MICE DAQ system utilises front end VME electronics that digitise the data and stores it in a buffer until the end of a spill. After the spill is complete, the data is then read-out and stored onto hard-disk drives. The DAQ is designed to be able to handle 600 muon events in a 1 ms spill period [43].

---

<sup>3</sup>Originally produced for use on the ALICE experiment.

## **2.3 Conclusion**

This chapter has given an overview of the detectors, beamline elements, the cooling channel and software that make up the muon ionisation cooling experiment. The superconducting spectrometer solenoids will be discussed in further detail in the next chapter as they are the primary focus of this thesis.



## Chapter 3

# Field Mapping of the MICE Spectrometer Solenoids

The spectrometer solenoids are an essential part of MICE and are necessary to perform the emittance measurement of the muon beam. The prime focus of this thesis is to produce computer models of the magnetic field of both spectrometer solenoids, SSU and SSD. The actual model will be described in chapter 4.

To produce the computer models, the magnetic fields need to be measured so that comparisons between the model and data can be made. The data are also required for the fitting procedure of the field model. A custom made mapping machine was developed by the CERN B-field mapping team to measure the field.

The spectrometer solenoids have been field mapped twice in their lifetime, by the same mapping machine. First they were mapped soon after they were assembled and a large set of field map data was taken. They were mapped again in March 2018, where they sit in the MICE beamline during data taking.

During commissioning of the experiment, it was realised that large stray magnetic fields could cause problems with the detector electronics. This motivated the design, construction and installation of the partial return yoke to mitigate the stray fields. Moreover the spectrometer solenoids had to be re-trained after installation in the MICE beamline; this process will be discussed in section 3.3. These two facts meant that the field within the bore of the solenoids will be different when they are installed in the beamline to when they were mapped for the first time, hence the motivation for the second set of data.

The second set of data is much less comprehensive but hugely important as the field is measured in situ so that any effect on the field from the partial return yoke or the training process can be taken into account in the field model.

### 3.1 Motivation

A good knowledge of the field in the tracker regions is essential for the measurement of the MICE muon beam, before and after passing through the absorber. This is due to the measurement of the transverse momenta,  $p_{x,y}$ , being dependent on the axial field component,  $B_z$ . This can be shown by considering a muon travelling down the beamline with longitudinal momentum  $p_z$  and initial transverse momenta  $p_x$  and  $p_y = 0$ .

The scintillating fibre trackers measure the position and time of the muon as it passes through each tracker plane. As the muon enters the solenoidal field within the tracker region, it will undergo a helical trajectory with the radius of the helix given by:

$$R = \frac{p_x}{qB_z} \quad (3.1)$$

and helix wavenumber given by:

$$k = \frac{qB_z}{p_z} \quad (3.2)$$

where  $q$  is the charge of the muon.

In simplified terms, the track finding software fits a helix to the measured space points at all five tracker planes using  $R$  and  $k$  as fit parameters. The components of the momenta of the muon can then be deduced from the above equations.

As stated in section 1.2.1, it is better to define the RMS emittance,  $\epsilon_{RMS}$ . The normalised RMS emittance in two dimensions is calculated from the determinant of the covariance matrix shown in equation 1.16. Noting that  $\langle x'^2 \rangle \propto \sigma_{p_x}^2$  where  $\sigma_{p_x}$  is the standard deviation of the distribution of  $p_x$  for an ensemble of muons. Then equation 3.1 becomes:

$$\sigma_R = \frac{\sigma_{p_x}}{qB_z} \quad (3.3)$$

From here it is clear that the fractional error of  $\sigma_{p_x}$  is related to the fractional error on  $B_z$  via:

$$\frac{d\sigma_{p_x}}{\sigma_{p_x}} \propto \frac{dB_z}{B_z} \quad (3.4)$$

In the tracking region the betatron function,  $\beta$ , is flat as shown in figure 2.6. This implies that  $\beta' = 0$  and therefore the off-diagonal terms of the covariance matrix are zero since  $\alpha = -\beta'/2$ . Therefore the 2D emittance reduces to:

$$\epsilon_{x,RMS} \propto \sqrt{\sigma_x^2 \sigma_{p_x}^2} = \sigma_x \sigma_{p_x} \quad (3.5)$$

where the proportional sign is used as constants are multiplied for the conversion between phase space and trace space.

Therefore the fractional error on the emittance due to the error on the field is given by:

$$\frac{d\varepsilon}{\varepsilon} \propto \frac{dB_z}{B_z} \quad (3.6)$$

MICE aims to measure the emittance of the muon beam to within  $10^{-3}$  [21]. This requires that all systematic uncertainties to be constrained to around  $10^{-4}$  so that their sum does not exceed the specification. Therefore the axial field should be known to within  $10^{-4}$ .

## 3.2 Spectrometer Solenoids

Both spectrometer solenoids consist of five superconducting coils labelled – M1, M2, E1, CC and E2. These coils are wound on a common mandrel, machined from a single piece of aluminium that is  $\sim 2544$  mm long and has a diameter of  $\sim 711$  mm when warm. The coils are wound from NbTi, a type-II superconductor, incorporated into a copper matrix with a Cu:NbTi ratio of 4:1 [44]. The critical temperature of NbTi is  $\sim 10$  K; consequently, the coils must be kept cool using liquid helium at  $\sim 4$  K. Aluminium plating is then attached over the mandrel to create spaces to allow the coils to be bathed in roughly 180 litres of liquid helium. This assembly forms the ‘cold mass’ of the magnet, as shown in figure 3.1. An aluminium cylinder exists coaxial with the cold mass, with a diameter roughly half the outer casing, acting as a thermal radiation shield.

The helium for the coils is kept cold using three two-stage cryo-coolers each with a cooling capacity of 1.5 W at 4 K with an additional single-stage cooler to cool the high temperature superconductor (HTS) leads that supply currents to the magnet. The radiation shield is kept at  $\sim 70$  K, reducing the heat load on the cold mass. After preliminary testing of the spectrometer solenoids it was discovered that there was excessive heat leaking to the cold mass and so modifications were made that include adding two pulse-tube cryo-coolers to each magnet to increase the total cooling capacity to 7.5 W [46].

Two large support rings are attached to the cold mass to act as an anchor for the supports. The cold mass is suspended in the magnet assembly by eight supports made from racetrack shaped fibre/epoxy bands with aluminium links. The high spring constant of the material ensures that any movement of the cold mass during operation is minimal. These supports are designed to carry loads in the longitudinal direction of 500 kN and loads of 50 kN in the radial direction. The outer casing is then formed from 20 mm thick 304 stainless steel, surrounding

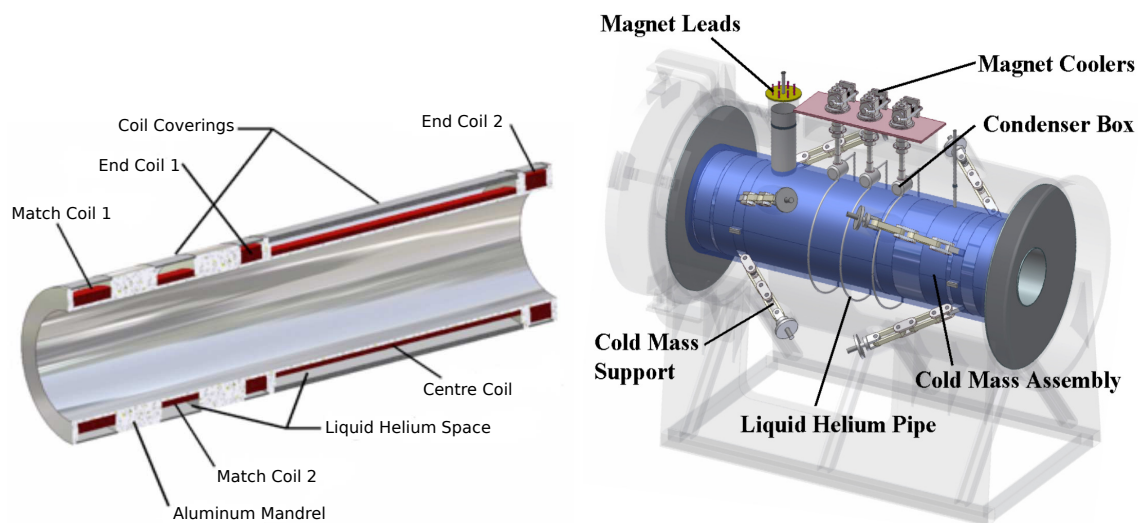


Fig. 3.1 Left: a labelled cross section diagram of the cold mass assembly of a spectrometer solenoid. Right: diagram showing how the cold mass sits inside the spectrometer solenoid's cryostat along with the support structures, current leads and helium supply lines. Note that this figure does not show the radiation shield. Figures adapted from [45].

the cold mass assembly and radiation shield, forming a vacuum vessel for insulation. This steel is austenitic and therefore non-magnetic.

The two match coils are each powered by a power supply that can output  $\sim 300$  A at 10 V. The tracking part of the solenoid is formed by the two end coils and the centre coil, together known as ECE. These three coils are powered in series with a supply with the same rating as the match coils. To allow the field from the two end coils to be tuned, they are both in parallel with a pair of trim power supplies that can deliver  $\pm 60$  A. A simple circuit diagram is shown in figure 3.2. By tuning these power supplies, the field in the centre coil region can be made to be uniform. Current is supplied to the magnets from the power supplies with copper wire capable of carrying 300 A. Then within the magnet, the current is passed to the HTS leads which then supply the coils.

Superconducting magnets provide strong magnetic fields which interact with the conductors of the coils. If windings in the coil move against each other, the movement can cause frictional heat to be generated [47]. If the temperature of the surrounding conductor reaches above the critical temperature, the superconductor becomes resistive and the massive current being supplied further heats the conductor through Joule heating. This event is known as a 'quench'. If no protection against a quench exists the superconductor can be extensively damaged from arcing or large heat loads. For very strong fields, superconducting magnets are 'trained' which is explained in section 3.3.

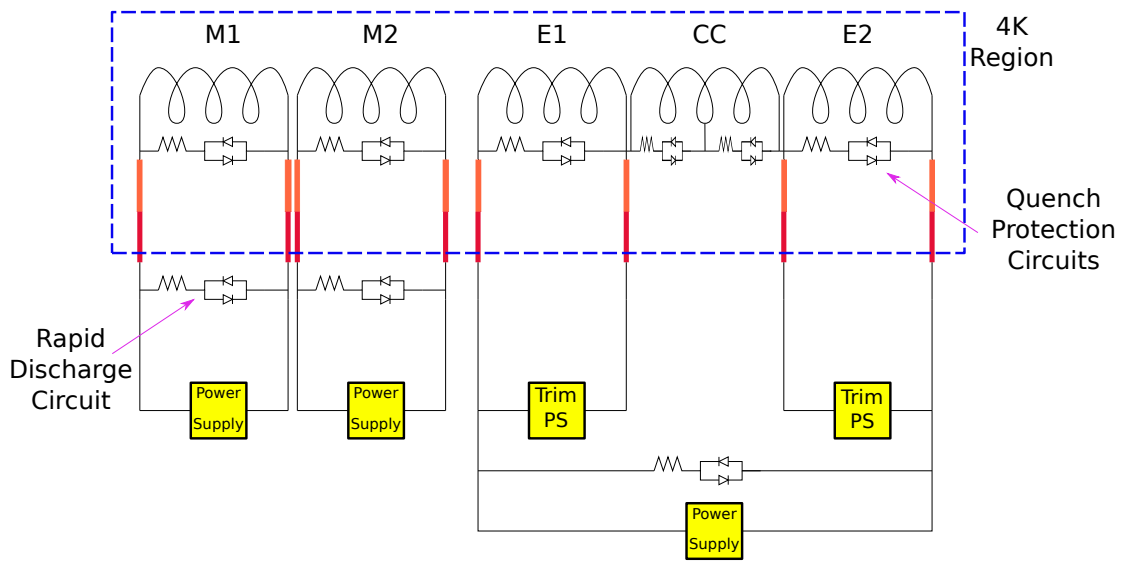


Fig. 3.2 Simplified circuit diagram of the spectrometer solenoids.

The MICE spectrometer solenoids have quench protection circuits designed to safely absorb the stored energy, of the order of megajoules, of the coils when a quench occurs. In the event of a quench, the current from the power supplies is cut and then the current present in the magnets is allowed to pass through dump resistors which dissipate the energy stored in the magnets via heat. This heat then boils off the liquid helium. The primary concern is the ‘hot-spot’ temperature which occurs at the origin point of the quench. If it is too high then the conductor can burn out. To reduce the hot-spot temperature, it is desirable to transition the whole magnet into a non superconducting state so that the heat generated from Joule heating is dissipated by the whole volume of the magnet rather than by a small portion. Heating of the coils is aided by a process known as ‘quench-back’. This process occurs due to the conducting aluminium mandrel that the coils are wound around, which acts as a secondary coupled circuit. Currents are induced in the mandrel due to the changing magnetic field from the coils as the current decays away when it is dumped into the resistor packs. These currents then heat the mandrel which then conduct heat to the coils.

### 3.2.1 As Built Dimensions

The field models of the spectrometer solenoids described in chapter 4 use the dimensions and winding pattern of the coils to calculate magnetic fields. The as-built dimensions of both spectrometer solenoids are listed in the two tables below. These dimensions are from [48].

Coil	$R_{\text{inner}}$ [mm]	$R_{\text{outer}}$ [mm]	Depth [mm]	Length [mm]	Centre [mm]	$N_{\text{Layers}}$	$N_{\text{Turns}}$	$N_{\text{Total}}$
M1	258.0	304.1	46.1	201.2	124.0	42	115	4830
M2	258.0	288.9	30.9	199.4	564.0	28	114	3192
E1	258.0	318.9	60.9	110.6	964.0	56	64	3584
CC	258.0	280.1	22.1	1314.3	1714.0	20	768	15360
E2	258.0	325.7	67.7	110.6	2464.0	62	64	3968

Table 3.1 As built coil dimensions of SSU. The coil centre position is measured from the M1 end of the cold mass.  $N_{\text{Turns}}$  is the number of turns in each layer.

Coil	$R_{\text{inner}}$ [mm]	$R_{\text{outer}}$ [mm]	Depth [mm]	Length [mm]	Centre [mm]	$N_{\text{Layers}}$	$N_{\text{Turns}}$	$N_{\text{Total}}$
M1	258.0	304.4	46.4	201.2	124.0	42	115	4830
M2	258.0	288.6	30.6	199.4	564.0	28	114	3192
E1	258.0	319.6	61.6	110.6	964.0	56	64	3584
CC	258.0	280.4	22.4	1314.3	1714.0	20	766- 768	15352
E2	258.0	326.2	68.2	110.6	2464.0	62	64	3968

Table 3.2 As built coil dimensions of SSD. Note that the first four layers of the centre coil for SSD are wound with two less turns.

### 3.2.2 SSU Cold Dimensions

The as-built dimensions are expected to change when the magnet is cooled down to operating temperatures due to thermal contraction. A small scale study performed using a finite element analysis software package, [49] was performed to estimate how the coils of SSU deform as they are cooled down and the effect on the field. The results of that study are shown in table 3.3 below.

Coil	$R_{\text{inner}}$ [mm]	$R_{\text{outer}}$ [mm]	Depth [mm]	Length [mm]	Centre [mm]
M1	257.04	301.5	44.5	200.6	123.666
M2	256.98	286.6	29.6	198.9	562.116
E1	257.09	316.5	59.4	110.2	960.566
CC	257.12	278.3	21.2	1310.1	1708.216
E2	257.12	322.9	65.7	110.2	2455.766

Table 3.3 Estimated cold dimensions of SSU.

### 3.3 Superconducting Magnet Training

As mentioned, the individual windings in superconducting magnets can move when a large field is reached by the coils. Movement between windings can cause frictional heat resulting in a quench. To reach the high design current of the coils, they first need to be ‘trained’. Magnet training involves gradually increasing in the current in a coil until it quenches due to coil slippage and then repeating this process until the design current is reached. Gradually the windings in the coil settle into position due to the material’s shape memory effect [47]. This training can be lost when the coils are warmed up to room temperature and the coils relax.

The spectrometer solenoids were trained after construction and needed to be re-trained after the modifications were made. They also had to be re-trained when they were placed into the MICE beamline with each of the cooling channel magnets operating together.

#### 3.3.1 SSD M1 and Quench Protection Issues

During the training and commissioning of the spectrometer solenoids in September 2015, the leads supplying current to the M1 coil in SSD failed, rendering it unusable. Field map data exists with it operational in the first data set. Its dimensions are still listed for completeness but it will be largely ignored in the rest of this thesis.

Problems with the quench protection system on SSD meant that it was not possible to safely use the trim power supplies during the MICE step IV data taking programme. Furthermore, due to SSU having an identical design, it was deemed too risky to use its trim supplies. Therefore during the second round of field mapping, the trim supplies were unavailable and so the currents supplied to the E1 and E2 coils are identical to the current supplied to the centre coil.

### 3.4 Partial Return Yoke

Calculations showed that the stray magnetic field originating from the cooling channel magnets was in excess of 50 mT [50] at  $\sim 7.5$  m from the beam axis. This was deemed dangerous to the electronic equipment operating in the MICE hall, especially the tracker electronics which sit right next to the spectrometers. The solution adopted was to retrofit a return yoke for the field, shielding the equipment outside of it. Ideally the return yoke would be a cylinder that surrounds the cooling channel magnets but this was impossible in practice due to the design of the solenoids and supporting structures. Instead the partial return yoke (PRY) was conceived.

The PRY, as its name suggests, only covers the cooling channel partially with the top and bottom being uncovered. Shown in figure 3.3, it covers two sides of the cooling channel, leaving the top and bottom uncovered. It consists of eight steel plates 4 m long and 1.5 m high with an additional four smaller plates that cover the AFC region. This makes it easier to swap absorber material since only a small section needs to be removed. The upstream and downstream ends of the PRY then have end plates with openings for the beam to propagate through that are 0.25 m in radius. The whole assembly is bolted to large steel legs that are bolted to the floor with support braces bolted across the top for stability.

The shielding plates are all 10 cm thick made from AISI 1010 low carbon steel. This steel was chosen because it is relatively cheap and has a high relative magnetic permeability,  $\mu_r$ , and high saturation level. These factors make it ideal for use in magnetic shielding. The performance of the PRY is determined by where the magnetic field drops to 5 G ( $5 \times 10^{-4}$  T) outside of the shield as this is the level deemed to be safe by the laboratory. Detailed studies show that it contracts the 5 G line to within the PRY horizontally [50]. Although the vertical direction is not shielded, the 5 G line is still halved to 2 m.

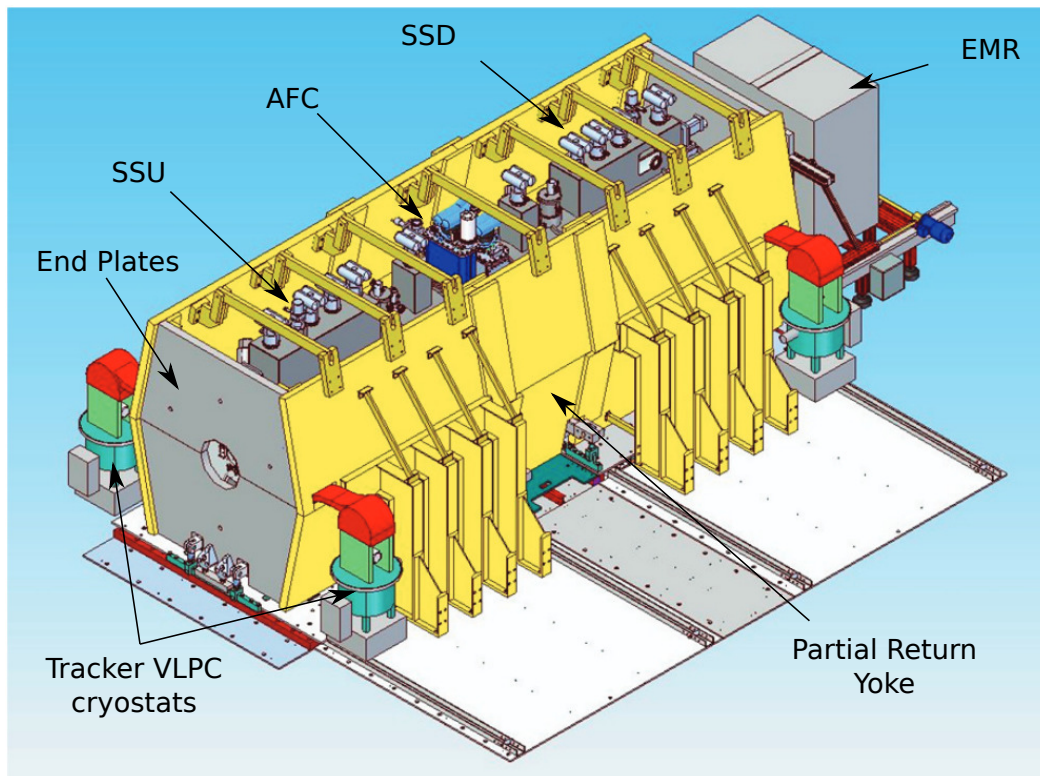


Fig. 3.3 Labelled rendering showing how the cooling channel is enclosed within the partial return yoke. The red parts on top of the tracker cryostats are the wave guides coming from the trackers within the spectrometer solenoids. Figure adapted from [51].

The horizontal forces on the PRY are of the order of a few kN, as such they must be monitored during operation. To do this wire strain gauges are employed.

## 3.5 Field Mapping Machine

The custom made field mapping machine has been used to map the field of all the cooling channel magnets including the focus coils which will not be discussed. An overview of its design and operation is given below.

### 3.5.1 Design

The field mapping machine, shown in figure 3.4, consists of a moving disk with Hall probes attached to it. The disk is orientated transverse to the solenoid axis and its motion is along this axis. It sits on a carriage that is guided on a pair of rails fixed to a 5 m long aluminium quarter pipe. A toothed belt is fixed to the carriage which is moved by a servo motor at one end of the quarter pipe. The disk can be rotated in steps of  $5^\circ$  and is fixed into place with a pneumatically operated piston; this slots into holes that are drilled around the outside of the disk. The disk and the carriage are made from non-magnetic materials.

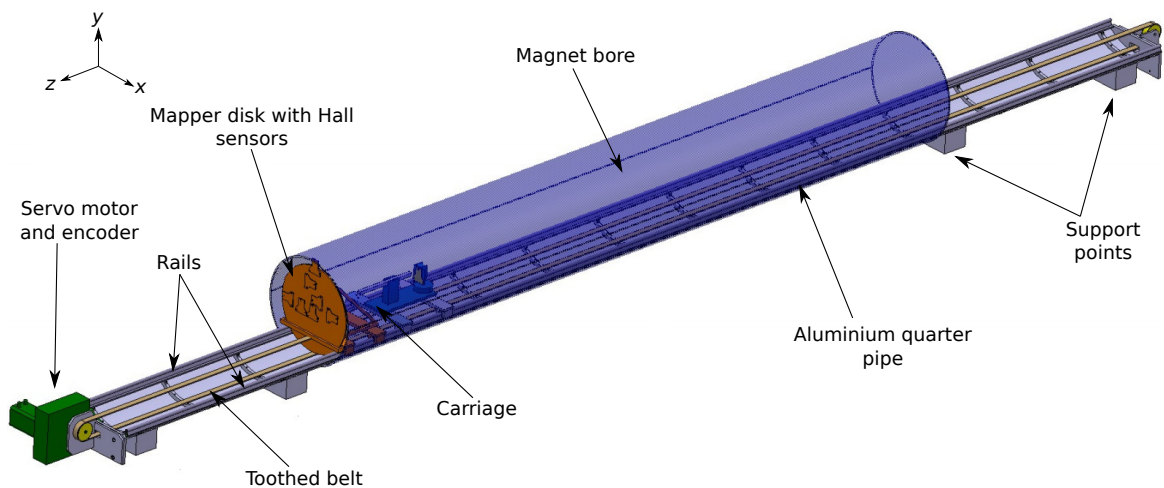


Fig. 3.4 Labelled diagram of the field mapping machine as it would sit inside the bore of a magnet which is represented by the translucent blue cylinder.

The disk can hold up to seven individual Hall probes, labelled 0-6, that are attached at different radii given in table 3.4. Each Hall probe consists of a glass cube with three

individual single axis Hall sensors attached to three faces. They are arranged such that each probe measures the  $B_r$ ,  $B_\phi$  and  $B_z$  components of the solenoidal field for any rotation of the mapper disk. This is shown clearly in figure 3.5.

Probe Number	0	1	2	3	4	5	6
Radius [m]	0.0	0.03	0.06	0.09	0.12	0.15	0.18

Table 3.4 Probe number with its corresponding radius from the centre of the disk.

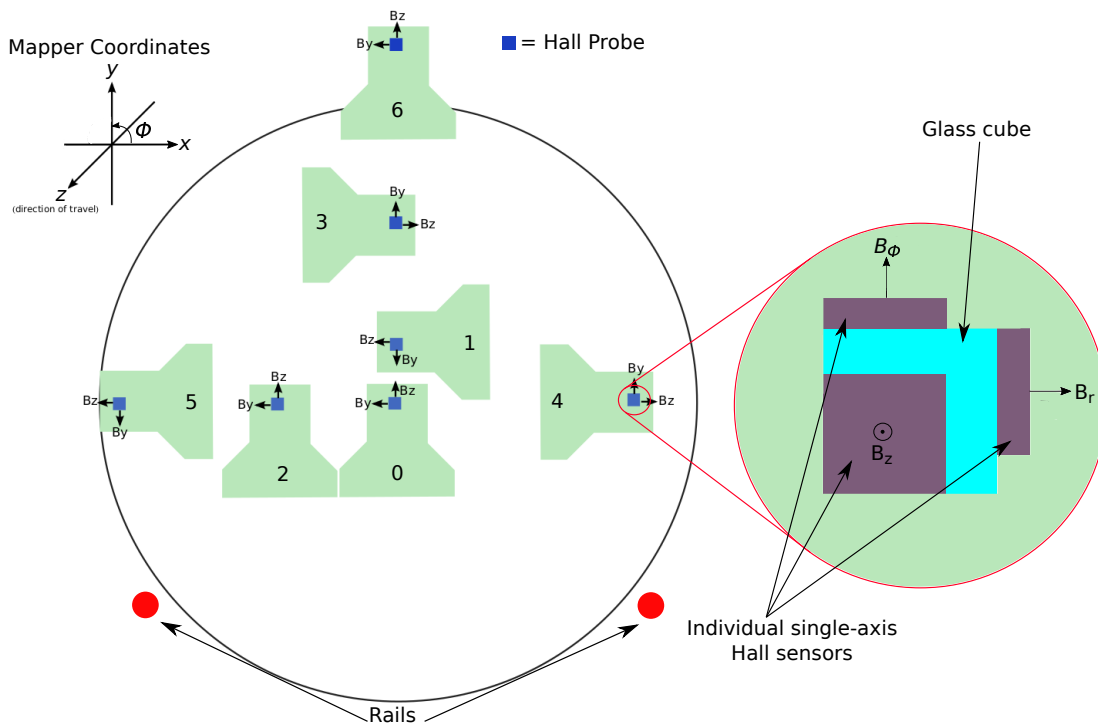


Fig. 3.5 Schematic diagram of the mapper disk and a close up of one of the Hall probes. The  $B_y$  and  $B_z$  component arrows show the transverse field as measured in the probes individual coordinate system. These are converted into the mapper's coordinate system when the data is read out. The green areas show the electronics cards that support and read out each of the Hall sensors with the number on each card denoting the corresponding probe number.

### 3.5.2 Operation

The mapping machine is operated by a PC that sits well outside of the high field region. This PC also reads out the Hall probe signals and saves the data to text files for analysis. To control the mapping machine, a grid file is written that contains information about the desired

measurement grid for a field map run. The grid file contains the start and end position in both the longitudinal and azimuthal directions along with the chosen number of steps.

Before each run, the mapper disk sits in its home position. This position is where the longitudinal coordinate,  $z$ , is zero. When mapping the field the disk is moved forward by the servo motor via the toothed belt to a longitudinal position defined by the grid file. The disk is then stopped and the field values are read out by each Hall probe. Then the disk is moved towards the next longitudinal position and so forth until the end position is reached. When the end position is reached, the disk is rotated to the next azimuthal position and the disk is then moved backwards to each longitudinal position. This procedure repeats until all points defined by the grid file are mapped.

Probe 6 protrudes from the edge of the disk and therefore it clashes with the two rails and the quarter pipe, as can be inferred from figure 3.5. For this reason, probe 6 is required to be removed when the bottom  $110^\circ$  arc is mapped. Therefore, complete field maps consist of two mapping runs and so two sets of data – one with probe 6 and one without (although for the latest mapping data, probe 6 was not used). These reasons will be discussed in section 3.6.2.

### 3.5.3 Mapper Coordinate System

The mapper coordinate system is a right handed coordinate system and is shown in figure 3.5, with the longitudinal coordinate,  $z$ , being approximately parallel with the solenoid axis. Also shown are the two transverse coordinates,  $x$  and  $y$ , with the former being horizontal and the latter being the vertical. Due to the cylindrical symmetry of the magnets, it is often much easier to work with cylindrical polar coordinates. In this case the azimuthal angle,  $\phi$ , is defined from the positive  $x$  axis.

It is not possible to perfectly align the mapping machine axis with the axis of the solenoid magnets. Instead the axes of the magnets and mapping machine will be rotated and offset with respect to each other. The field models described in chapter 4 will account for this, although to aid the field models, the magnetic axis is estimated as described in section 3.9.

In addition to the imperfect alignment, the mapper carriage is not expected to move longitudinally perfectly and without motion in the transverse plane. To account for this effect, a survey was taken and corrections are applied to the data. The survey is discussed in section 3.7.2.

Each Hall probe measures the field in its individual coordinate system. As discussed, due to the arrangement of the Hall probes it is easy to convert from the probe's system to the mapper system in cylindrical polar coordinates.

## 3.6 Field Mapping Data

Two sets of field mapping data were taken for both spectrometer solenoids. This thesis will emphasize the second set of data, since the data were taken in situ and include the effect of the retrofitted PRY. The first data set is also discussed because it was used to hone the field models described in the next chapter.

### 3.6.1 Original Data Set

The original data set was taken in the summer of 2013 after the spectrometer solenoids were modified and trained as described in previous sections. A plethora of different field maps were recorded with different magnet currents and measurement grids.

The field models described in the next chapter were developed and tested using this original data set. The modelling work preceded the field measurement described in this chapter, and indeed the original data set would have formed the basis of the results in this thesis. However, the opportunity to re-measure the field of the spectrometer solenoids as they sit in the experiment was desirable considering any change to the field caused by the PRY could be measured and included in the field models.

### 3.6.2 In Situ Data Set

The second data set was recorded in March 2018 with the spectrometer solenoids left in the position they were during MICE step IV data taking. The absorber focus coil module was removed so that the mapping machine could be loaded into the bores of the spectrometer solenoids. The data had to be taken in only a week and as a result of the large inductances of the superconducting solenoids, they ramp up/down to current slowly. Hence due to these time constraints, the second set of data was far less comprehensive but the most important field maps were recorded to produce the field models.

As mentioned previously, probe 6 needs to be removed to map certain azimuthal portions. Considering the time constraints and the fact that its radius is outside of the tracker region, it was deemed much more efficient to keep it removed. Thus, this set of data has no measurements from probe 6.

The current settings that were mapped for SSU and SSD are shown in tables 3.5 and 3.6 respectively. The tags are used to distinguish between the current settings and will be referenced throughout this thesis.

Settings with individual coils or the two end coils and centre coil together, collectively known as ‘ECE’, powered to 30 A are required to build the field models. Then for SSU a

realistic step IV beam line setting, with a field of 3 T in the tracker region, is also mapped. For SSD a similar setting is mapped along with a lower power setting with 2 T in the tracker region. These step IV beam line setting field maps are used to test the effectiveness of the field models. In addition to the 30 A ECE setting, higher current field maps were also recorded to check the linearity of the field and the effect of the PRY.

When the currents of the coils reached the desired setting, a short field map with no rotation of the mapper disk was taken. The field was then plotted from these maps so that the grid for the full field map could be decided. Full field maps would then be taken with every 20° rotation of the disk and every 5 cm longitudinally as the grid. For individual coil settings, every 2.5 cm was mapped in the longitudinal direction to allow the sharp peak of the field to be mapped in more detail.

$I_{M1}$ [A]	$I_{M2}$ [A]	$I_{E1}$ [A]	$I_{CC}$ [A]	$I_{E2}$ [A]	Setting Tag
0	0	0	0	0	<b>0A-SSU</b>
0	0	30.0	30.0	30.0	<b>30A-ECE-SSU</b>
30.0	0	0	0	0	<b>30A-M1-SSU</b>
0	30.0	0	0	0	<b>30A-M2-SSU</b>
191.0	168.25	205.7	205.7	205.7	<b>3T-SSU</b>

Table 3.5 Table of mapped currents for SSU.

$I_{M1}$ [A]	$I_{M2}$ [A]	$I_{E1}$ [A]	$I_{CC}$ [A]	$I_{E2}$ [A]	Setting Tag
0	0	0	0	0	<b>0A-SSD</b>
0	0	30.0	30.0	30.0	<b>30A-ECE-SSD</b>
0	30.0	0	0	0	<b>30A-M2-SSD</b>
0	195.72	144.0	144.0	144.0	<b>2T-SSD</b>
0	193.78	205.7	205.7	205.7	<b>3T-SSD</b>

Table 3.6 Table of mapped currents for SSD. Note that the M1 coil is unusable but listed here for completeness.

During the mapping of SSU, the mapper disk's home position sits at the upstream end of the magnet. This means that the mapper's  $z$  coordinate points from upstream to downstream. Conversely for SSD, the disk's home position sits at the downstream end of the magnet. This is due to the fact that the support structure for the motor end of the mapping machine does not fit in the empty space usually occupied by the AFC module. Hence for SSD, the  $z$  coordinate points from downstream to upstream. Therefore, the greater the  $z$  position in mapper coordinates, the closer it is to the centre of the cooling channel for both spectrometer solenoids. This difference in coordinate systems is rectified using the survey data described in section 3.7.2.

The axial field component,  $B_z$ , as measured by the central probe (probe 0) for each of the settings shown in the tables above, is shown in figure 3.6. Note that the polarity of SSD is the same as SSU, however, as described above the mapper disk runs in the opposite direction. This results in the Hall probes being orientated in the opposite direction meaning that they register the positive  $B_z$  field as negative.

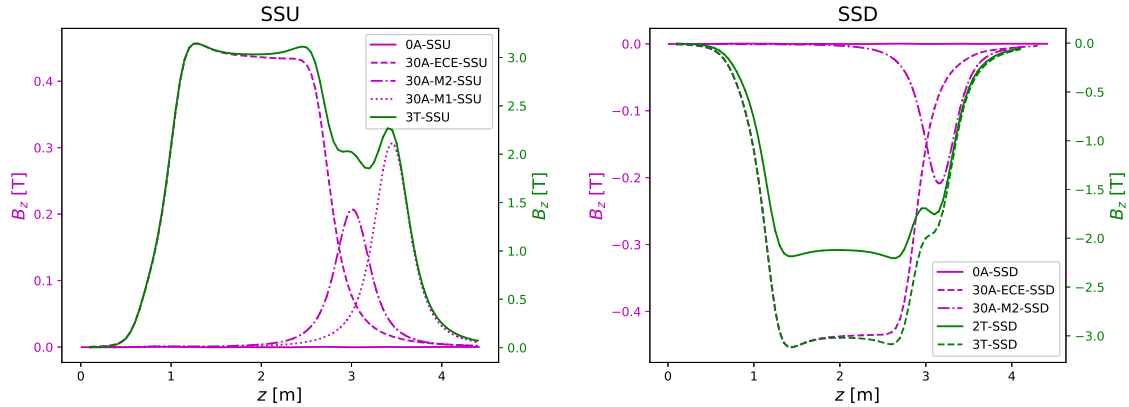


Fig. 3.6 Plots showing the axial field component,  $B_z$ , for SSU (left) and SSD (right) as measured by probe 0. The colour of the dual y-axes labels correspond to the colour of the graph lines.

### 3.7 Field Mapper Survey

Working in the coordinate system of the mapper is convenient although this system neglects any aberration of the mapper disk's movement through the solenoid bores. To study the movement of the disk, a survey detailing the motion of the disk was performed for each solenoid.

The survey was achieved using a laser survey device which scans the position of a reflective target that is attached to the mapper disk using the Hall probe support points. There are many survey points that are fixed in various positions within the MICE hall. By keeping the laser scanner stationary at one end of a spectrometer solenoid and by surveying the fixed points, the position of the scanner in the coordinate system of the MICE hall can then be determined. Then it is trained onto the target attached to the mapper disk as it moves through the solenoid. The target's position can then be determined, in the MICE hall coordinate system, for multiple points as the disk moves along its axis.

For both SSU and SSD three sets of survey data were recorded, each with the target in a different position. One set had the target attached to the centre of the mapper disk in the

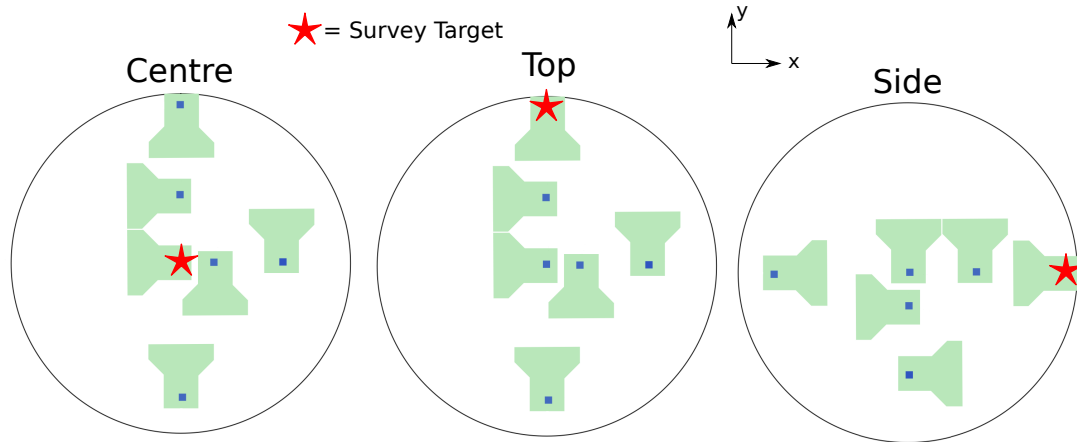


Fig. 3.7 Diagram showing the position of the survey target for the three sets of survey data. The longitudinal coordinate,  $z$ , comes out of the page. This diagram shows the mapper disk from the perspective of the laser scanner.

space usually occupied by probe 0. For the other two sets, the target was attached to the point where probe 5 sits, at a radius of 0.15 m from the centre of the disk. Then for one of these data sets, the mapper disk is rotated such that the survey target sits at the top of the mapper disk and for the other set the disk is rotated so that the target sits at  $90^\circ$  with respect to the top. This is illustrated in figure 3.7. The three sets of survey data are then designated as: centre, top and side.

The same grid file was used to operate the field mapper for all surveys. The grid was chosen to be a set of 44 longitudinal steps, each step being 100 mm in distance. No rotations of the disk were undertaken during a survey run and the mapper disk was operated in the forward direction only.

### 3.7.1 Survey Results

The survey is intended to be used to convert from the coordinates reported by the mapping machine to the coordinates used by the experiment. The MICE coordinate system is a right-handed coordinate system with one axis, the  $z$  axis, marking the nominal beam line that runs through the experiment, the zero of which is close to the exit of the second dipole (D2). In this thesis the MICE hall coordinates will be represented by:  $(x', y', z')$  with each of these coordinates being parallel to the unprimed  $(x, y, z)$  that represent the coordinate system reported by the mapping machine installed on SSU. As mentioned, to measure the field for SSD the mapping machine had to be placed so that it is mirrored across the centre of the cooling channel. Therefore, the  $z$ -axis for the mapper installed on SSD runs anti-parallel to

the MICE coordinate system; this is easily accounted for. Hence,  $z'$  runs along the beam axis,  $y'$  runs anti-parallel to gravity and  $x'$  is the horizontal coordinate. The spectrometer solenoids are placed such that ideally their magnetic axes are collinear with the  $z'$  coordinate.

The results of the surveys and how they are used to convert to MICE coordinates are shown in the following sections.

### 3.7.1.1 SSU

Firstly, the conversion between  $z$  and  $z'$  is found. This is simply a case of plotting the longitudinal coordinate reported by the mapper against the coordinate measured by the survey and fitting a straight line as shown in the top left plot of figure 3.8. The gradient and intercept of the fitted line is then used to convert  $z$  into  $z'$ .

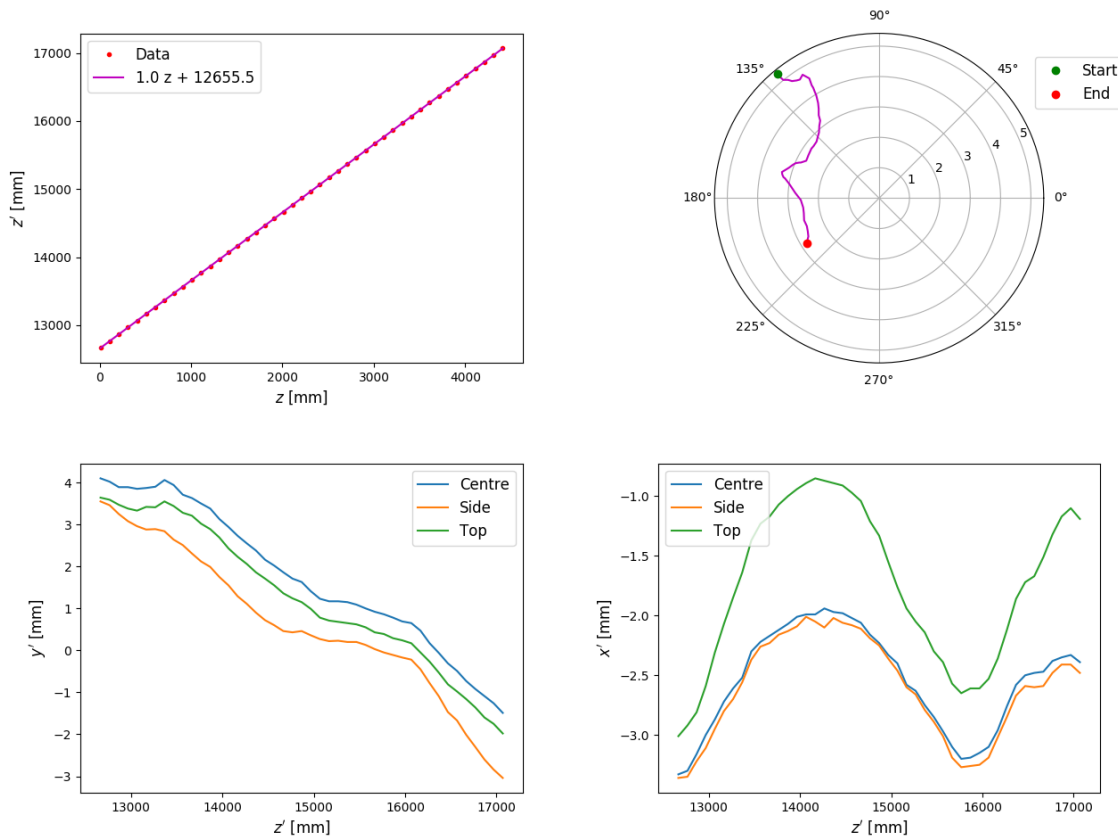


Fig. 3.8 Plots summarising the results of the survey performed on the mapping machine installed in SSU. The radial coordinate of the polar plot is in millimetres.

The motion of the centre of the mapper disk in the plane transverse to the beam axis, as the disk moves towards the survey machine, is shown in the polar plot. The start and end points are labelled as the green and red dots respectively. The motion of the mapper disk in

the two transverse axes is shown in the bottom two plots and in figure 3.8. For the  $y'$  vs  $z'$  plot, the radial offset (150 mm) of the survey target from the centre of the disk is subtracted from the  $y'$  measurements for the top survey. Likewise, the offset is subtracted from the  $x'$  measurements of the side survey for the  $x'$  vs  $z'$  plot. This is to clearly show the motion of the target in all three surveys.

The bottom left plot shows the motion in the vertical direction with respect to the beam axis. It shows a general downward trend indicative of the mapper carriage being tilted. The bottom right plot shows the motion in the horizontal direction. The disk moves in a side-to-side motion. Since the mapper disk is reset to the home position before each survey, these plots also show that the motion of the disk along the carriage is coherent across each run for SSU. However, the top survey shows that the side-to-side motion of the top of the disk is stronger and offset by approximately 0.5 mm. This could be due to the mapper disk tilting on its support by varying amounts as it moves along the carriage. A more detailed set of survey measurements could highlight this.

### 3.7.1.2 SSD

As with SSU, the conversion between the longitudinal coordinates is found with a straight line fit, shown in the top left plot of figure 3.9. For SSD however, the gradient is negative due to the mapper disk moving from downstream to upstream.

The plots shown in figure 3.9 show the same information as the plots in figure 3.8 except with the survey data from SSD. In the case of SSD, the motion of the disk in the vertical axis appears to be relatively level until a point where a sharp decline is experienced. However, the side survey shows deviation from the top and centre surveys, especially at lower  $z'$ . The cause of this is unknown but could be due to tilting or rotation of the disk from its nominal position. The horizontal motion of the disk seems to be far more coherent between the surveys albeit with the top survey showing deviation as with SSU.

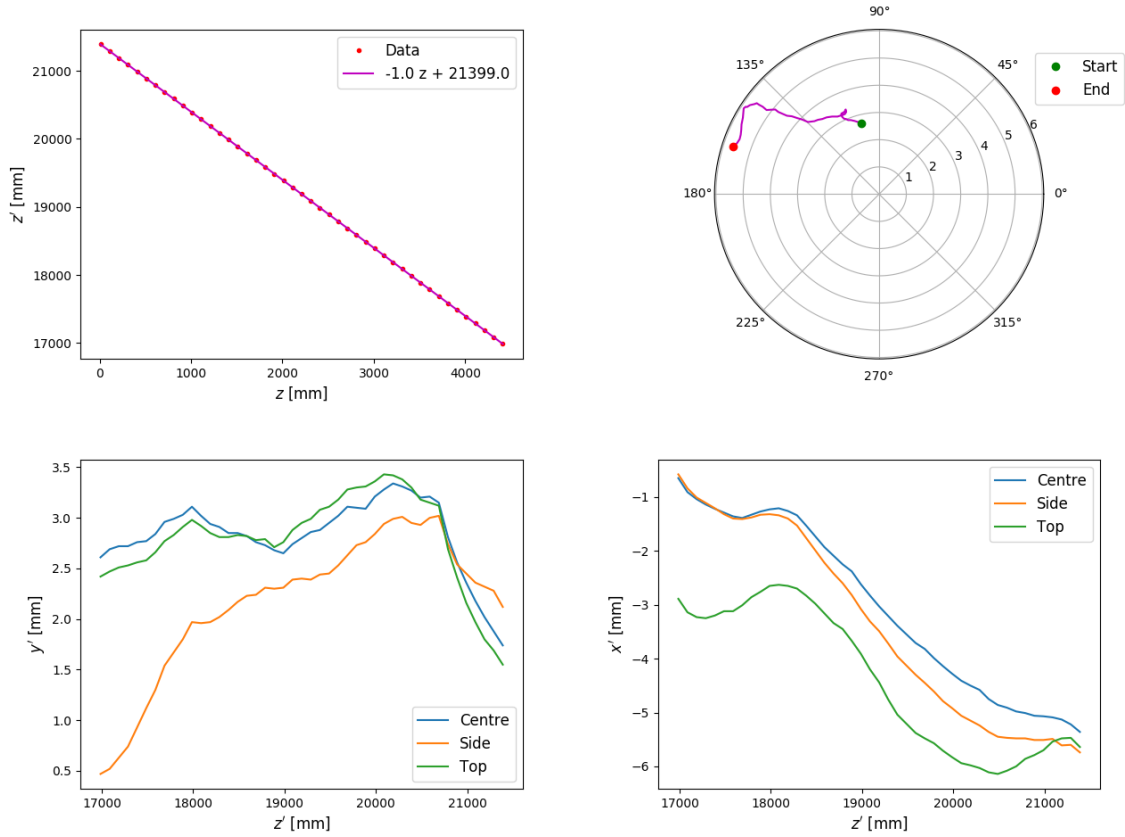


Fig. 3.9 Plots summarising the results of the survey performed on the mapping machine installed in SSD. The radial coordinate of the polar plot is in millimetres.

### 3.7.2 Applying Survey Corrections

Before the data are used to produce the magnetic field models, the coordinate system needs to be converted from the mapper coordinate system to the MICE coordinate system. First the longitudinal coordinate is converted using the gradient and intercept found in the straight line fit discussed above.

The motion of the centre of the disk is approximated by calculating the average  $x'$  and  $y'$  for each  $z'$  step across all three surveys. By using simple linear interpolation between these averages, two functions are found,  $X(z')$  and  $Y(z')$ , for the offsets that are applied to each transverse coordinate of the data points to convert to MICE coordinates.

$$\begin{aligned} x' &= x + X(z') \\ y' &= y + Y(z') \end{aligned} \tag{3.7}$$

The caveat with this approach is that this method assumes that the mapper disk remains flat in the transverse plane as it travels along the rails, meaning that the measured  $B_x, B_y, B_z$  components are unchanged. With more time, a far more comprehensive survey could be done to remedy this and allow corrections to be made.

### 3.7.3 Mapper Coordinate Reproducibility

The mapping disk is not expected to travel the exact longitudinal distance for each step. This causes the mapper disk to reach the incorrect location and records the field components with the  $z$  position it should be at. This can be a problem in the regions where the field gradient is high. The mapping machine reports its own  $z$  coordinate in the output data according to the amount of rotations from the home position that the servo motor has made, which is only accurate to within 0.5 mm. The accuracy of the survey equipment is much better – to within  $\sim 0.01$  mm.

Since all surveys were performed with the same grid, it is possible to estimate the random error in the longitudinal coordinate of the mapper. For all survey data, the longitudinal interval,  $\Delta z$ , between two neighbouring points was calculated and is plotted in the histogram shown in figure 3.10.

The histogram shows that the mean interval is 0.056 mm more than the chosen step size of 100 mm. It also shows that there is a spread in the distance moved by the disk with an RMS of 0.112 mm. The offset of the mean interval could cause problems as the error in the interval begins to add up, causing data points that are taken later on to have a compounded error in their longitudinal position. Whether this level of reproducibility of the longitudinal coordinate is acceptable is found by looking at the field measurements themselves.

To investigate the errors associated with the mapper not reaching the correct position sufficiently, five field maps of the 2T-SSD setting, using the same measurement grid were recorded. The grid chosen was similar to the grid used for the survey except with longitudinal step sizes of 50 mm, making 80  $z$  steps in total. The 2 T setting was chosen for convenience in the data taking schedule along with the stronger field. The stronger field gives rise to very steep gradients of the axial field in the regions at the edges of the solenoid, and in the regions between coils albeit less steep. Small offsets from the set  $z$  coordinate cause the wrong slice of the field to be sampled which could have large effects in these high gradient regions.

For each point in space,  $p$ , of the measurement grid, there are five measurements of each component of the field. Only the  $B_z$  component is considered here because it is the largest

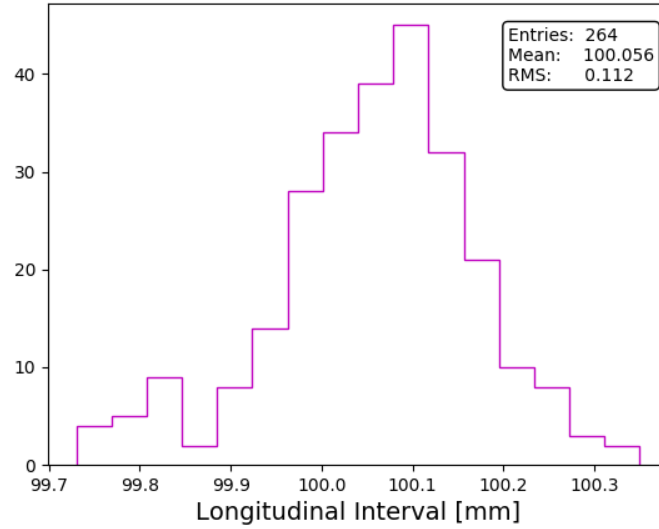


Fig. 3.10 Histogram showing the longitudinal interval between neighbouring points for all survey data.

and also experiences the largest gradients. At each point the average  $B_z$  is calculated:

$$\langle B_z \rangle_p = \frac{\sum_{i=1}^5 B_{z,i}}{5} \quad (3.8)$$

Then the residual between each measurement and  $\langle B_z \rangle$  calculated at that point is taken. The residual for all measurement points for all five field maps is then plotted in the histogram shown in figure 3.11. Any noise from the Hall sensors, which is expected to be a maximum of 0.1 mT (1 G), will also effect the residuals. The histogram shows that the residuals are centred about 0 mT with an RMS of 0.044 mT indicating that the mapping machine is sufficiently accurate and the reproducibility of the motion of the disk is also good. The noise on the Hall sensors seems to be less than was expected.

### 3.8 Estimating the Centre Positions of the Coils

To produce the field models of the spectrometer solenoids, the longitudinal location of the centre of each coil is required. Although the dimensions and position on the mandrel of the coils is known, the centre position of the coils in the mapping machine and MICE coordinate systems are not.

An estimation of the the centre position of the coil is possible by finding where the axial field component is at a maximum. To achieve this an eighth order polynomial is fitted to the

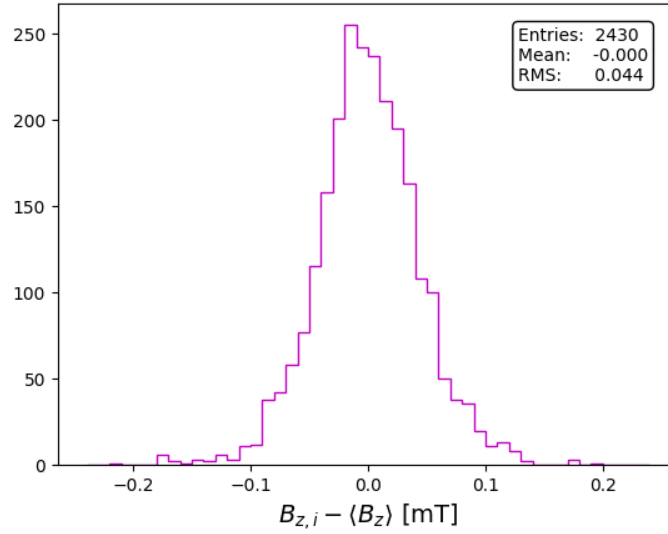


Fig. 3.11 Histogram of residual between measured  $B_z$  and  $\langle B_z \rangle$  for each data point.

region about the maximum measured  $B_z$ , shown in figure 3.12. Five steps in  $z$  either side of the maximum was chosen. This polynomial is then differentiated to give a function,  $f(z)$ , whereby finding the root in the region where  $B_z$  is at a maximum will yield an estimate for the  $z$  position of the centre of the coil.

The root of  $f(z)$  is found by using Halley's method, an iterative root finding algorithm given in equation 3.9. The initial  $z_n$  used is the  $z$  coordinate of the point with the strongest measured axial field. The iterations are stopped when  $z_{n+1} - z_n \leq 1 \mu\text{m}$ .

$$z_{n+1} = z_n - \frac{2f(z_n)f'(z_n)}{2(f'(z_n))^2 - f(z_n)f''(z_n)} \quad (3.9)$$

This is only achievable with the data sets where a single coil is powered. Therefore, only the centre positions of the two match coils for SSU and only M2 for SSD can be found. The remaining coil's centre positions are then inferred from these results and by looking at the dimensions of the spectrometer solenoids in tables 3.1 and 3.2. Using the survey data described in the previous section, the coil centre positions are also readily converted into MICE coordinates. The centre positions of all coils for both solenoids given in both  $z$  and  $z'$ , are shown in tables 3.7 and 3.8.

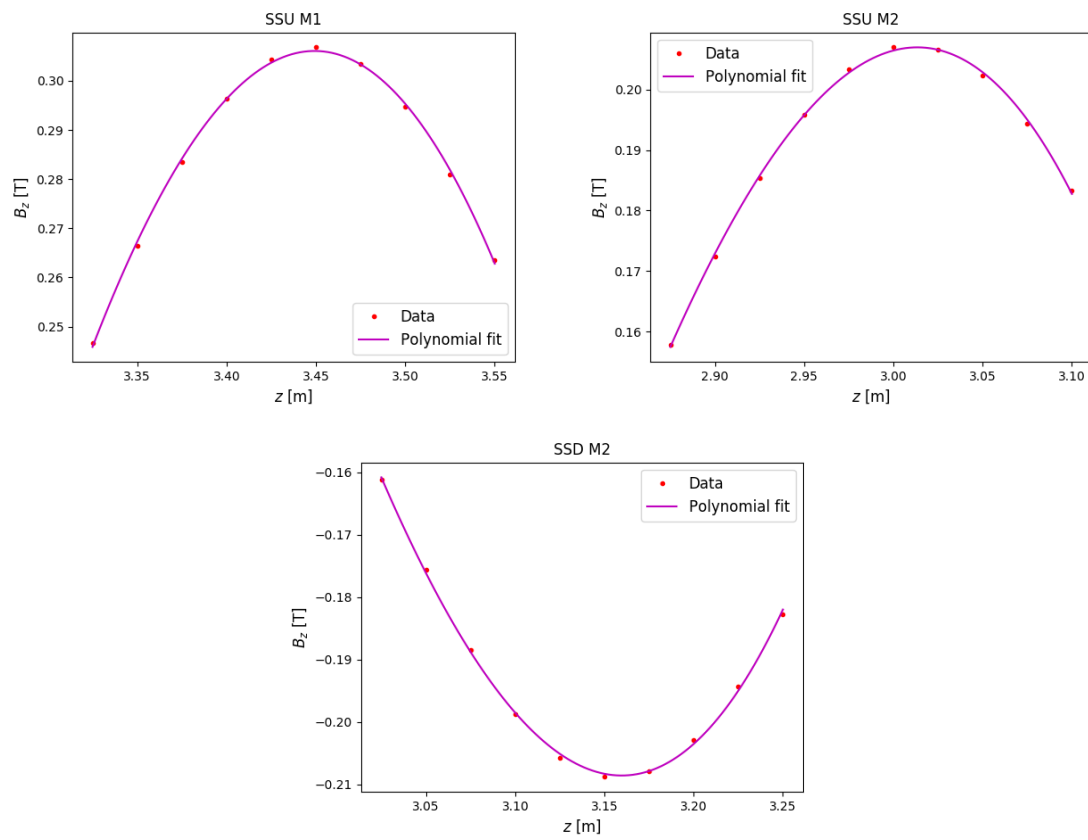


Fig. 3.12 Plots showing the polynomial fits used for the centre finding algorithm. The titles indicate the coil under inspection.

SSU	M1 [mm]	M2 [mm]	E1 [mm]	CC [mm]	E2 [mm]
$z$	3449.22	3013.39	2613.39	1863.39	1113.39
$z'$	16106.55	15670.49	15270.29	14519.90	13769.50

Table 3.7 Table of centre positions in  $z$  and  $z'$  for all of SSU's coils. Coloured cells are those that are calculated from the method described above.

SSD	M1 [mm]	M2 [mm]	E1 [mm]	CC [mm]	E2 [mm]
$z$	3599.65	3159.65	2759.65	2409.65	1259.65
$z'$	17797.05	18237.34	18637.59	18987.81	20138.54

Table 3.8 Table of centre positions for all of SSD's coils.

## 3.9 Finding the Magnetic Axis

Ideally the longitudinal axis of the mapping machine would coincide with the magnetic axes of the spectrometer solenoids, however, the mandrels holding the coils will be rotated and offset with respect to the mapper axis and the MICE Hall coordinates. It is possible to estimate these angles and offsets by exploiting the properties of solenoidal fields.

Before the method is discussed in section 3.9.2, corrections to the  $B_\phi$  components of the measured field are required. The evidence for this correction originates from looking at vector plots of the transverse field for a complete revolution of the mapper disk at a point in  $z$ . For a Maxwellian field, the transverse field vectors should point towards the magnetic axis. As shown in figure 3.13 this is not quite the case. Instead the vectors appear to be rotated in such a way that they do not converge at the axis. This was assumed to be caused by a slight rotation of the Hall sensors which mixes the three components of the field. The  $B_\phi$  component gains contributions from the two much larger  $B_z$  and  $B_r$  components, which can be accounted for.

### 3.9.1 Probe Tilt Corrections

If a Hall sensor is not perfectly aligned to the coordinate system, the measurements it makes will include contributions from the other two field components proportional to the angle between the true orientation of the Hall probe and the axes of the coordinate system. The measured  $B_\phi^m$  component approximately becomes:

$$B_\phi^m = B_\phi^t + A_{\phi z} B_z^t - A_{\phi r} B_r^t \quad (3.10)$$

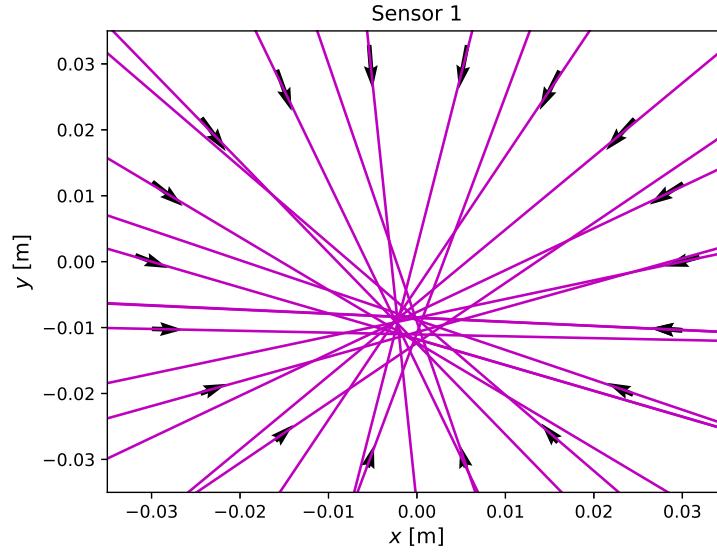


Fig. 3.13 Vector plot showing the transverse field as measured by probe 1 for a whole rotation of the mapper disk at a single position in  $z$ . The purple lines continue in the direction of the vectors. The transverse coordinates are in the mapping machine system.

where a superscript ‘m’ denotes a measured value and ‘t’ denotes the true value with the two small mixing angles,  $A_{\phi_z}$  and  $A_{\phi_r}$ . In the following section the mapping machine coordinate system is used.

By exploiting Maxwell’s equations for magnetic fields, these two angles can be found so that the  $B_\phi$  component can be corrected accordingly. Taking the integral form of  $\nabla \times \vec{B} = 0$  with the safe assumption that there are no sources of current density or electric fields within the bore of the solenoid:

$$\oint \vec{B} \cdot d\vec{l} = 0 \quad (3.11)$$

This equation implies that the integral of  $B_\phi^t$  over a complete revolution of the mapper disk should equal zero. Any deviation from this is due to the contributions described in equation 3.10. By combining equations 3.10 and 3.11 and using the approximations  $B_z^t \approx B_z^m$  and  $B_r^t \approx B_r^m$ , the following relation is obtained:

$$\oint B_\phi^m dl = A_{\phi_z} \oint B_z^m dl - A_{\phi_r} \oint B_r^m dl \quad (3.12)$$

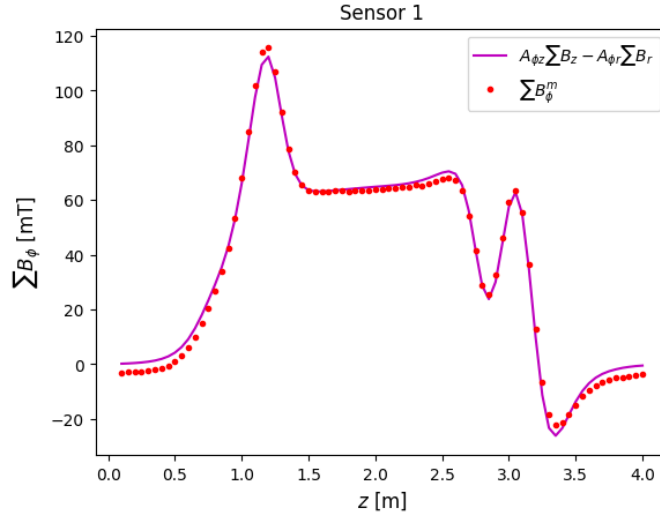


Fig. 3.14 Plot showing an example of the fit performed on the left hand side of equation 3.13. The data shown here is as measured by probe 1 for the 2T-SSD setting.

Where the integral of  $B_\phi^t$  vanishes accordingly. Then by replacing the integral with sums of all measured components in a complete revolution in  $\phi$ , the relation becomes:

$$\sum_{\phi} B_{\phi}^m = A_{\phi z} \sum_{\phi} B_z^m - A_{\phi r} \sum_{\phi} B_r^m \quad (3.13)$$

By evaluating the sums in the above equation for every  $z$  position of a field map, the two angles are found by using a least squares fit. Minimising the sum of the squared residuals between the left hand side and right hand side of equation 3.13 yields the two mixing angles. The fit is performed using MINUIT [52]. An example of this fit is shown in figure 3.14.

With the two mixing angles found for each probe, the  $B_\phi$  components for all the data are then corrected by re-arranging equation 3.10 for  $B_\phi^t$  and using the same approximations used for equation 3.12. Note that this method is not applicable to probe zero because of the fact that it is close to the magnetic axis where the transverse field is very small. The correction then becomes obvious when the same vector plot as in figure 3.13 is repeated but with the corrections applied as shown in figure 3.15. The transverse field vectors now converge somewhat to a point.

Field maps for all current settings were used to calculate the mixing angles and the mean taken. This is shown for both spectrometer solenoids in figure 3.16. The errors shown are the standard error of the mean. The angle  $A_{\phi r}$  has larger errors, especially for smaller radii probes, which is expected due to the fact that the  $B_r$  and  $B_\phi$  components are small.

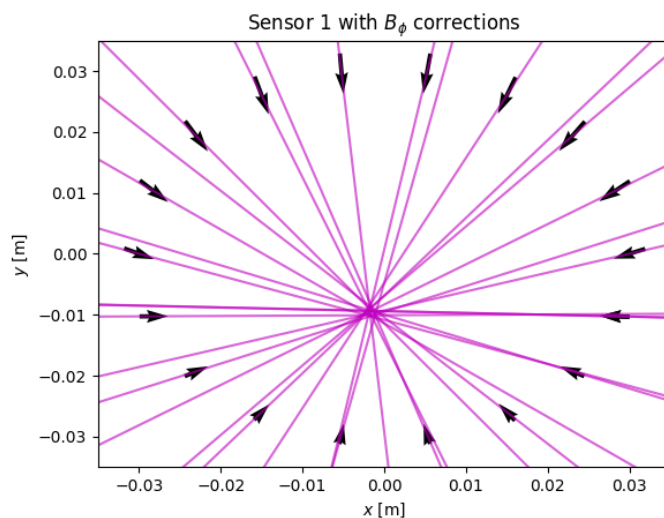


Fig. 3.15 Vector plot showing the same transverse field as figure 3.13 but with the  $B_\phi$  components corrected.

Since the probes were removed from the mapper disk whilst the mapping machine was moved from SSD to SSU and to perform the survey, the above process was applied to the data from both magnets.

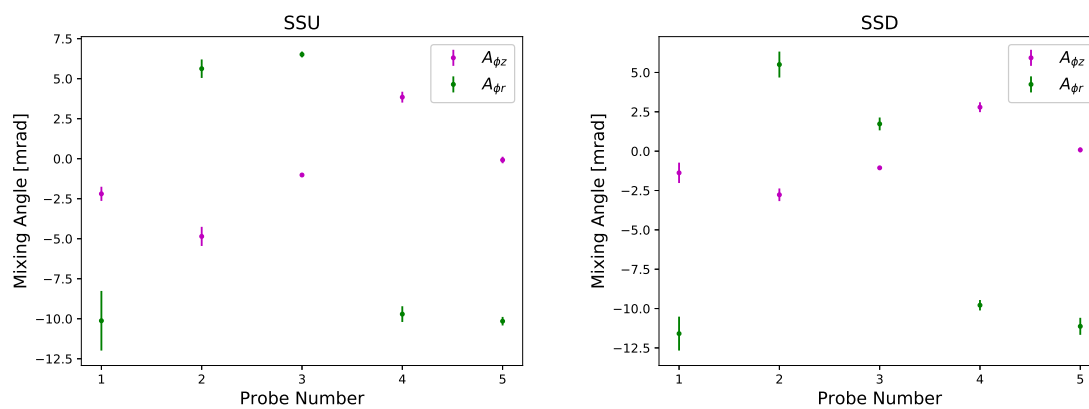


Fig. 3.16 Plots showing  $A_{\phi_z}$  and  $A_{\phi_r}$  mixing angles for probes 1-5 for both solenoids.

### 3.9.2 Method

The corrections to the  $B_\phi$  components of the field are performed. Then before the magnetic axis is found, the survey corrections are applied to the data as per section 3.7.2. This allows the magnetic axis to be known in MICE coordinates along with accounting for the transverse movement of the mapper.

Working in Cartesian coordinates is easier when considering rotations about the axis. Consider a set of points in the mapper coordinate system  $(x_m, y_m, z_m)$ . The coil is rotated about the  $x$  and  $y$  axes by angles of  $\theta_x$  and  $\theta_y$  respectively, with rotations in the  $z$  axis neglected due to the cylindrical symmetry. Also the coil could be offset from the transverse axes by the offsets  $p_x$  and  $p_y$ . Then consider a set of points in the coordinate system of the coil, where the  $z_c$  axis is the magnetic axis,  $(x_c, y_c, z_c)$ . The coordinates of the coil system can be found by applying rotation matrices and the offsets:

$$\begin{pmatrix} x_c \\ y_c \\ z_c \end{pmatrix} = R_y R_x \begin{pmatrix} x_m \\ y_m \\ z_m \end{pmatrix} + \begin{pmatrix} p_x \\ p_y \\ 0 \end{pmatrix} \quad (3.14)$$

Where  $R_y$  and  $R_x$  are the rotation matrices whose product is given by:

$$R_y R_x = \begin{pmatrix} \cos \theta_y & -\sin \theta_x \sin \theta_y & \sin \theta_y \cos \theta_x \\ 0 & \cos \theta_x & -\sin \theta_x \\ -\sin \theta_y & \cos \theta_y \sin \theta_x & \cos \theta_x \cos \theta_y \end{pmatrix} \quad (3.15)$$

Then applying the small angle approximation so that  $\cos \theta_i \approx 1$  and  $\sin \theta_i \approx \theta_i$  and letting terms with  $\mathcal{O}(\theta_i \theta_j) \approx 0$ . Multiplying out equation 3.14 gives approximate expressions for the coordinates of the coil system with respect to the mapper and MICE hall systems:

$$x_c = x_m + \theta_y z_m + p_x \quad (3.16)$$

$$y_c = y_m - \theta_x z_m + p_y \quad (3.17)$$

$$z_c = -\theta_y x_m + \theta_x y_m + z_m \quad (3.18)$$

The magnetic field components measured in the mapper coordinate system,  $(B_{x,m}, B_{y,m}, B_{z,m})$ , are then calculated by:

$$\begin{pmatrix} B_{x,m} \\ B_{y,m} \\ B_{z,m} \end{pmatrix} = (R_y R_x)^\top \begin{pmatrix} B_{x,c} \\ B_{y,c} \\ B_{z,c} \end{pmatrix} \quad (3.19)$$

with  $(B_{x,c}, B_{y,c}, B_{z,c})$  being the components of the field that would be measured in the coil system. Using matrix multiplication and applying the same small angle approximations as before, the expressions for  $(B_{x,m}, B_{y,m}, B_{z,m})$  become:

$$B_{x,m} = B_{x,c} - B_{z,c} \theta_y \quad (3.20)$$

$$B_{y,m} = B_{y,c} + B_{z,c} \theta_x \quad (3.21)$$

$$B_{z,m} = B_{x,c} \theta_y - B_{y,c} \theta_x + B_{z,c} \quad (3.22)$$

To first approximation, the transverse field components,  $B_{x,y}$ , should be linear with their respective coordinate at a given longitudinal position as shown in figure 3.17. For a solenoid magnet, the transverse field is zero on the magnetic axis. This is where  $x_c = y_c = 0$  and  $B_{x,c} = B_{y,c} = 0$ .

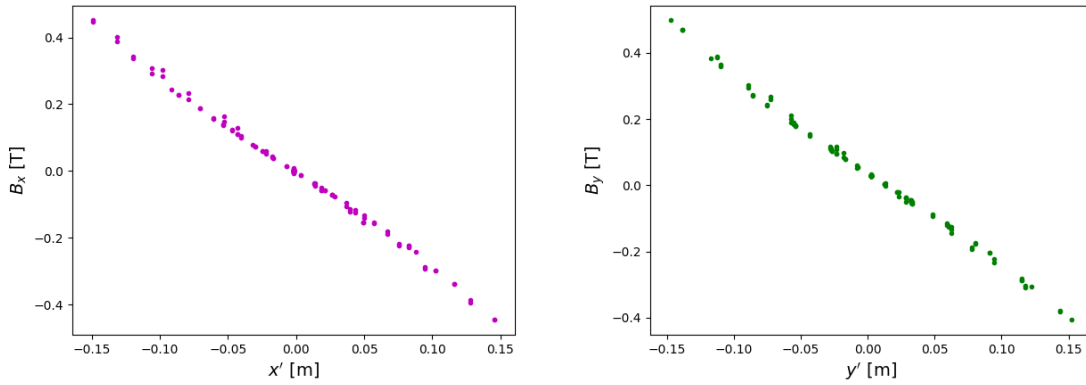


Fig. 3.17 Plots of  $B_{x,y}$  vs  $x', y'$  for a particular  $z'$  position using data from all probes.

By considering the  $x$  component only, the rotation angle  $\theta_y$  and offset  $p_x$  can be estimated. The linearity of the transverse components mean that a straight line can be fitted so that:

$$B_{x,m} = m_x x_m + c \quad (3.23)$$

The straight line fit is performed for all  $z$  positions so that they all have a unique  $m_x$  and  $c$ . The constant represents any offset from the axis. In the coil system there is no such offset as it is perfectly aligned with the axis, furthermore, the  $B_{x,c}$  component must be linear with  $x_c$ . Then equation 3.14 becomes:

$$B_{x,m} = m_x x_c - B_{z,c} \theta_y \quad (3.24)$$

where  $x_c$  is given by equation 3.10. Using the approximation  $B_{z,c} = B_{z,m}$ , which is justifiable since the two angles are small and  $B_{x,y} \ll B_z$ . Then letting the gradient  $m_x$  be the same for  $B_{x,m}$  and  $B_{x,c}$ , the angle and offset can be found by minimising the quantity:

$$\chi^2 = \sum_i^N \frac{(B_{x,m}^{\text{meas}} - B_{x,m}^{\text{calc}})^2}{\sigma^2} \quad (3.25)$$

with  $B_{x,m}^{\text{meas}}$  being the measured values,  $\sigma$  the measurement error and  $B_{x,m}^{\text{calc}}$  calculated from:

$$B_{x,m}^{\text{calc}} = m_x(x_m + \theta_y z_m + p_x) - B_{z,m} \theta_y \quad (3.26)$$

The error in the measurement of  $B_{x,m}$ ,  $\sigma$ , is then estimated as  $\sim 1$  mT. The error is likely overestimated, however, it allows an estimate of the errors for the angles and offsets to be calculated by the fitting routine.

The fit is then performed using MINUIT with the angle and offset as the free parameters. To find the angle  $\theta_x$  and the offset  $p_y$ , the same method is applied but to the  $y$  components of the field.

### 3.9.3 Test on a Simulated Coil

In order to test the magnetic axis finding method, the magnetic field of a test coil powered at 200 A was calculated using the method described in the next chapter. The field produced by the coil is shown in figure 3.18. The test coil has identical dimensions to those of M1 and is rotated and offset from the measurement axis with the following angles/offsets:

$\theta_x$ [mrad]	$\theta_y$ [mrad]	$p_x$ [mm]	$p_y$ [mm]
0.37	-0.72	-12.23	4.28

Table 3.9 Rotation angles and offsets applied to the simulated test coil.

Using the method described above, the calculated angles and offsets of the test coil are:

$\theta_x$ [mrad]	$\theta_y$ [mrad]	$p_x$ [mm]	$p_y$ [mm]
$0.33 \pm 0.07$	$-0.76 \pm 0.07$	$-12.28 \pm 0.25$	$4.04 \pm 0.25$

Table 3.10 Calculated rotation angles and offsets of the simulated test coil.

These results show decent agreement within in the estimated errors. With this in mind, this method can be used on the real data sets with the survey corrections applied to them.

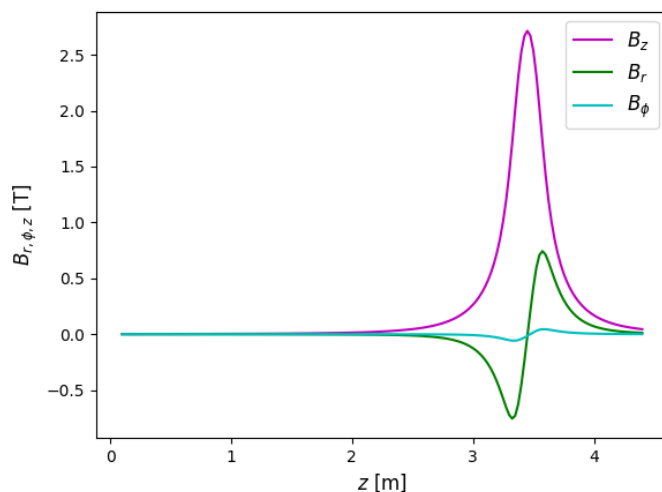


Fig. 3.18 Plot showing the  $B_r$ ,  $B_\phi$  and  $B_z$  components of the test coil as would be measured by a Hall probe at a radius of 0.15 m and angle of  $30^\circ$  from the horizontal .

### 3.9.4 Results

To calculate the angles and offsets for SSU, a field map of the 3T-SSU setting is used. For SSD field maps of the 2T-SSD and 3T-SSD settings were used and the reported values are the average of the two. Field maps taken with strong magnetic fields were chosen because the stronger transverse fields are well above the level of noise on the Hall probes. The results are summarised in tables 3.11 and 3.12 below.

$\theta_x$ [mrad]	$\theta_y$ [mrad]	$p_x$ [mm]	$p_y$ [mm]
$-0.61 \pm 0.03$	$0.90 \pm 0.03$	$-13.05 \pm 0.44$	$-7.64 \pm 0.44$

Table 3.11 Estimated rotation angles and offsets of SSU.

$\theta_x$ [mrad]	$\theta_y$ [mrad]	$p_x$ [mm]	$p_y$ [mm]
$0.26 \pm 0.02$	$1.12 \pm 0.02$	$-17.40 \pm 0.43$	$-8.43 \pm 0.43$

Table 3.12 Estimated rotation angles and offsets of SSD.

## 3.10 Conclusion

The anatomy of the MICE spectrometer solenoids were discussed in detail and the dimensions of their constituent coils given as they are necessary for the field models described in the next chapter. The partial return yoke was also discussed along with the reason it was installed. Problems that occurred during commissioning of the solenoids mean that the downstream spectrometer's M1 coil is unusable.

A custom made field mapping machine was manufactured for the purpose of producing field map data for the spectrometer solenoids. This design of the machine and its method of operation is explained. An original set of data was taken just after the solenoids were built, however, this was before the need for the PRY was realised. A second set of data was taken at the end of MICE's Step IV program ended in March 2018. This data set had the spectrometer solenoids in the positions they were in during data taking with the PRY surrounding them. It is this data set that will be used in the next chapter to produce the field models.

A survey of the mapping machine as it travels through the bores of the solenoids was performed. This chapter details the motion of the mapper disk and explains how the survey is used to convert from the mapping machine's internal coordinates into those of the MICE experiment. Converting between the two systems does assume that the mapper disk stays flat in the  $x$ - $y$  plane. With more time for a comprehensive survey this could be addressed.

The field models require an estimate of the centre position of the individual coils. To achieve this, a simple polynomial fit and root finding algorithm were utilised. Approximate centre positions were then found for the two match coils on SSU and for M2 only on SSD. The remaining coil's centre positions were inferred from the as-built dimensions listed in this chapter.

It was realised that corrections to the  $B_\phi$  components of the measured field were needed due to rotations of the Hall probes. A method using Maxwell's equations was discussed and the results show that the transverse field appears better behaved after the corrections are applied.

The method used to estimate the rotation angles and offsets of the solenoids from the MICE coordinate system was tested using a simulated test coil. The results are deemed to be satisfactory for an estimation. With this in mind, the method was used on the two spectrometer solenoids and their respective angles and offsets are listed.

Now that the field map data can be converted into the MICE hall coordinates and certain parameters of the coils have been estimated, modelling of the magnetic fields can begin.



## Chapter 4

# Magnetic Field Models of the MICE Spectrometer Solenoids

To perform an accurate measurement of the emittance, the magnetic field produced by the spectrometer solenoids within the tracking region needs to be well known. Producing Monte Carlo simulations of the experiment that agree with data requires knowledge of the whole field, including in the fringe field regions. In order to make field models for MAUS simple coil models are efficient, although they will not account for field aberrations from the PRY or deformity of the coils. Another method is to use finite element analysis using commercially available software packages. This method is time consuming and requires detailed measurements of the dimensions for each coil in the spectrometer solenoids, which is difficult considering they are susceptible to change during commissioning. With the field measurements described in the previous chapter, data driven field models are possible.

The MICE spectrometer solenoids can be operated at different current settings, therefore, the field model must be also be able to replicate any setting from given coil currents. It is inconceivable to record field maps of all the settings that were used.

The chosen approach was to record field maps of each individual coil, or the ECE coil set, at a low current – 30 A. The full procedure is then applied to all of these field maps to produce models that replicate the field produced by each coil/set if they were powered at 30 A. Then the field for a whole spectrometer magnet can be built up by scaling each modelled field according to the desired current and adding them together in a vector sum.

The model involves a few steps that each utilise least squares fitting to find the parameters of the model. First the method by which a solenoidal field, that must obey Maxwell's equations, is calculated from the dimensions and parameters of a coil is described. The first stage is a simple model which mixes two fields calculated from different dimensions that 'bracket' the dimensions of the coil in question. This is known as the geometrical fit model

which only accounts for the magnetic field produced by the coils. The PRY is expected to change the field within the spectrometer solenoids; this will be explored in this chapter. Therefore, the model must be able to account for this change.

The field components of the geometrical fit model are then subtracted from those of the data to form the residual field. This field must also obey Maxwell's equations. Using separation of variables, solutions to the Laplace equation are found involving Bessel functions, with infinite sums forming a general solution. The properties of the Bessel functions allow fitting to happen in stages to find the coefficients and phases of each term. When found, the residual field can be calculated at any point. This model is known as the Fourier-Bessel model.

Each element of the field model is described in this chapter and the model is then compared with the field map data. The level at which the complete model agrees with the data is then discussed.

## 4.1 Calculating a Solenoidal Field

To calculate the field produced by a solenoid we start with analytical expressions for the field produced by an individual current loop centred on the  $z$ , with radius  $a$  and current  $I$ . The following expressions are reported in [53]. Working in cylindrical polar coordinates the individual components of the field, at a point  $(r, \phi, z)$ , are calculated via:

$$\begin{aligned} B_z &= \frac{\mu_0 I}{2\pi\alpha^2\beta} [(a^2 - r^2 - z^2)E(k^2) + \alpha^2 K(k^2)] \\ B_r &= \frac{\mu_0 I z}{2\pi\alpha^2\beta r} [(a^2 + r^2 + z^2)E(k^2) - \alpha^2 K(k^2)] \\ B_\phi &= 0 \end{aligned} \quad (4.1)$$

where the following substitutions are made for clarity:

$$\begin{aligned} \alpha^2 &= a^2 + r^2 + z^2 - 2ar \\ \beta^2 &= a^2 + r^2 + z^2 + 2ar \\ k^2 &= 1 - \frac{\alpha^2}{\beta^2} \end{aligned} \quad (4.2)$$

The functions  $K(k^2)$  and  $E(k^2)$  are elliptical integrals of the first and second kind respectively. Equations 4.1 are exact for all points in space outside of the conductor, however, the elliptical

integrals are evaluated using numerical methods. The SciPy [54] scientific python library contains quick functions used for the evaluation of the integrals.

To calculate the field from a whole coil, it is first divided up into current loops according to the total amount of superconducting wire turns that constitute it. The separation between the current loops and their radii are calculated from the dimensions of the coil. The field at a point is then evaluated by adding each of the components calculated from all current loops in a vector sum. This process is performed for each set point in space to form a solenoidal field map.

Fields from rotated and offset coils, like the test coil in the previous chapter, are calculated by first rotating and offsetting the coordinates using the rotation matrix, given in equation 3.15, and then calculating the field. The coordinates and components are then rotated back using the transpose of the rotation matrix.

All field maps are handled in software using arrays of classes. These contain the three space coordinates and the three components of the field along with the norm,  $|\vec{B}|$ , calculated from the three components. Field maps are stored on disk in plain text, human readable, files. Scripts convert the raw data from the mapper machine into the same format as simulated fields. This enables real and calculated field map data to be processed by the same functions.

## 4.2 Geometrical Fit Model

The basis of the geometrical fit model is mixing two calculated solenoidal fields, using the method described above, in different proportions until a good fit to the data is achieved. These two fields are known as ‘bracketing’ fields.

The two bracketing fields are calculated using adjusted dimensions of the coil in question. For one field, the length of the coil is made 10% longer and the depth ( $R_{\text{outer}} - R_{\text{inner}}$ ), is made 10% thinner. For the other field, the length is 10% shorter and the depth 10% larger. This is illustrated in the rendering shown in figure 4.1. The green volume shows the actual dimensions of the coil being fitted to, whilst the red and blue volumes show the dimensions that the two bracketing fields are calculated from. The field produced by the three fields are shown in figure 4.2, if the green coil represented the centre coil of SSU. From now on the two bracketing fields will be referred to as *LT* and *SF* to represent the longer/thinner and shorter/fatter fields.

The motivation behind the model is to efficiently model the field produced by the coils using their dimensions because, although their as-built quantities are known, they are expected to change as they are cooled down to operating temperature. A model could of course be derived where the coil dimensions are used as fitting parameters, however, this involves

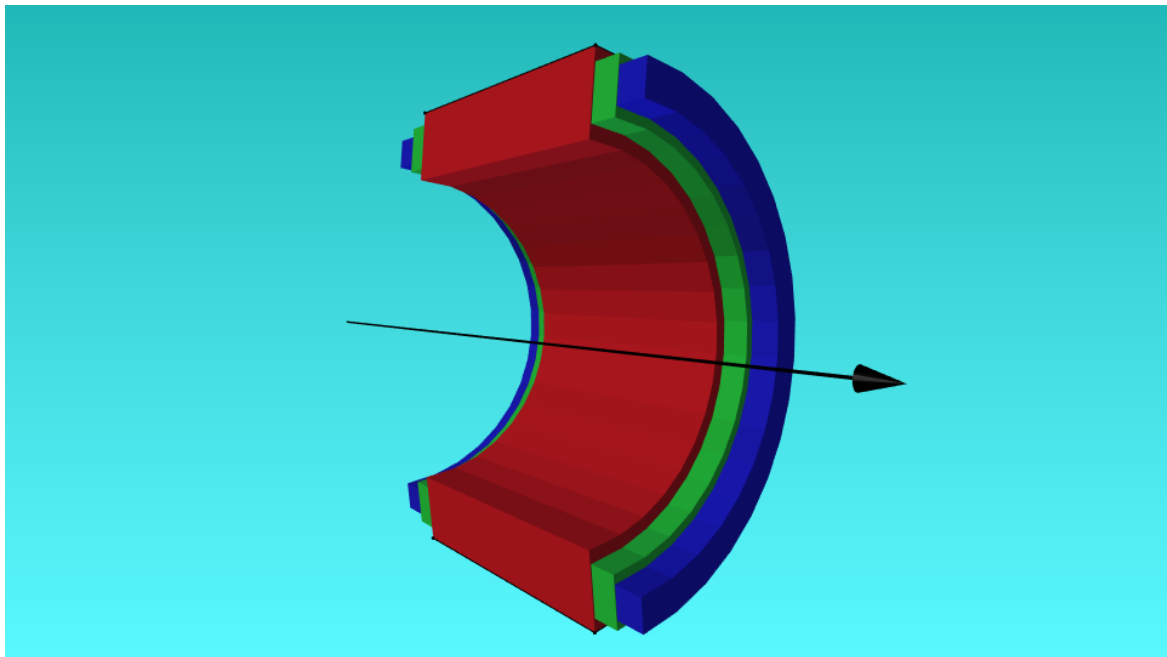


Fig. 4.1 Cutaway diagram showing the arrangement of the two bracketing coils and the true coil. The green volume shows the dimensions of the coil of interest. The blue and red volumes show the longer/thinner and shorter/fatter bracketing coils respectively.

calculating the field at all points in space during each iteration of the fit procedure. Instead, mixing two fields is far less computationally expensive. In addition to the mixing, other parameters are introduced. These other parameters include further rotation and offsets as those calculated earlier are estimations.

The technique used to calculate the bracketing fields assumes that the current loops constituting the coil are evenly spaced and perfectly circular. In reality, the winding density will not be uniform and the coils will be warped by thermal contraction, magnetic forces and gravity. These factors will cause deviations in the field from what can be modelled by the geometrical fit model. This is another motivation for the Fourier-Bessel model along with the effects of the PRY.

Both bracketing fields are calculated on an identical fine cylindrical grid of points for all coils with the appropriate rotation angles and offsets applied to them as listed in tables 3.11 and 3.12. The grid includes points at least 1 cm outside of the mapped region in both  $r$  and  $z$ . The geometric fit model is only applied to field maps of a single coil powered at 30 A, however, this is only possible for the match coils as the E1-CC-E2 (ECE) coils are powered in series for the field map data. A slightly different approach is used for the 30 A ECE field map data. First the model for the match coils is described.

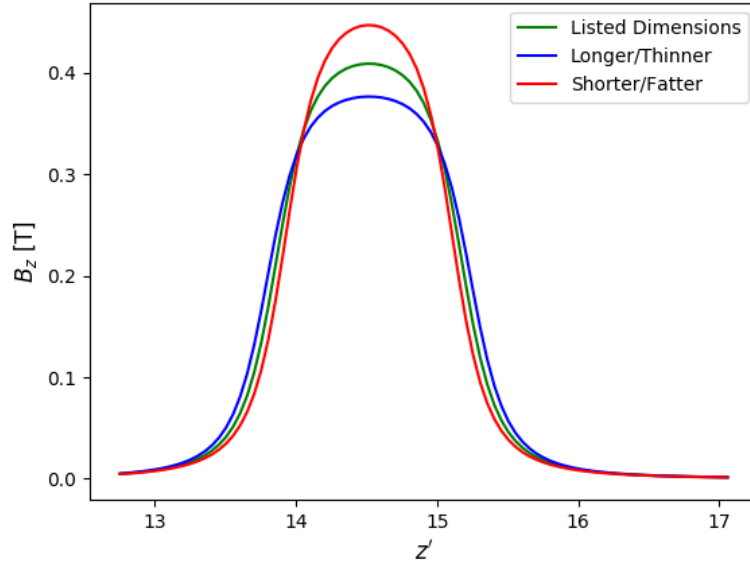


Fig. 4.2 Plot illustrating the axial field at  $r = 0$  of SSU's centre coil, powered at 30 A, as calculated from the listed dimensions in green. The blue and red lines show axial field from the two bracketing fields.

#### 4.2.1 Geometrical Fit Model for Match Coil Data

Before the fit proceeds, the data being fitted to has the survey and  $B_\phi$  corrections applied to them. As such the following is performed in the MICE coordinate system, however, prime symbols will be dropped for clarity. The superscript LT and SF below depict which bracketing field the component comes from.

The geometrical fit model proceeds as follows:

1. At each point,  $i$ , add the three field components,  $c = r, \phi, z$ , in proportion defined by the mixing parameter  $m$ , where  $0 < m < 1$ :

$$B_{c,i}^{\text{Mix}} = mB_{c,i}^{\text{LT}} + (m - 1)B_{c,i}^{\text{SF}} \quad (4.3)$$

2. Then at each point scale the field components by a scaling factor,  $s$ :

$$B_{c,i}^{\text{S}} = sB_{c,i}^{\text{Mix}} \quad (4.4)$$

3. Add longitudinal offset,  $p_z$ , to each  $z$  coordinate of the scaled field:

$$z_i = z_i^{\text{old}} + p_z \quad (4.5)$$

4. Convert this field into Cartesian coordinates; then rotate this field about the  $x$  and  $y$  axis by angles  $\theta_x$  and  $\theta_y$  whilst also add offsets  $p_x, p_y$  to the  $x, y$  coordinates:

$$\begin{pmatrix} B_{x,i} \\ B_{y,i} \\ B_{z,i} \end{pmatrix} = \begin{pmatrix} \cos \theta_y & -\sin \theta_x \sin \theta_y & \sin \theta_y \cos \theta_x \\ 0 & \cos \theta_x & -\sin \theta_x \\ -\sin \theta_y & \cos \theta_y \sin \theta_x & \cos \theta_x \cos \theta_y \end{pmatrix} \begin{pmatrix} B_{x,i}^S \\ B_{y,i}^S \\ B_{z,i}^S \end{pmatrix} \quad (4.6)$$

$$\begin{pmatrix} x_i \\ y_i \\ z_i \end{pmatrix} = \begin{pmatrix} \cos \theta_y & -\sin \theta_x \sin \theta_y & \sin \theta_y \cos \theta_x \\ 0 & \cos \theta_x & -\sin \theta_x \\ -\sin \theta_y & \cos \theta_y \sin \theta_x & \cos \theta_x \cos \theta_y \end{pmatrix} \begin{pmatrix} x_i^S \\ y_i^S \\ z_i^S \end{pmatrix} + \begin{pmatrix} p_x \\ p_y \\ 0 \end{pmatrix} \quad (4.7)$$

5. Now use 3D linear interpolation to obtain the  $B_x, B_y, B_z$  components of the mixed, scaled and rotated/offset field at each of the points in data,  $(x_j^{\text{data}}, y_j^{\text{data}}, z_j^{\text{data}})$ , to form the comparison field.
6. Convert this comparison field back into polar coordinates and then calculate the quantity:

$$\chi^2 = \sum_{c=r,\phi,z} \sum_{j=0} = \frac{\left( B_{c,j}^{\text{meas}} - B_{c,j}^{\text{comp}} \right)^2}{\sigma^2} \quad (4.8)$$

where the sum over  $j$  is the sum over all data points,  $B_{c,j}^{\text{meas}}$  is the measured  $B_c$  component at point  $j$  and  $B_{c,j}^{\text{comp}}$  is the component from the comparison field.

This procedure then forms a function with the parameters  $-m, s, \theta_x, \theta_y, p_x, p_y$  and  $p_z$ . These parameters are found using MINUIT that minimises  $\chi^2$ . The value of  $\sigma$  used is 1 mT. This is likely more than the actual error in the measured components of the field, however, it serves as a useful normalisation for the  $\chi^2$  function.

Step 5 in this model utilises a 3D linear interpolation algorithm to interpolate the rotated model field onto the data points so that the square residuals can be calculated. This interpolation method was chosen because it is relatively quick which is important considering it is required to be performed multiple times during minimisation. To keep the systematic error caused by interpolation to a minimum, the grid on which the model field is calculated is a lot finer than the grid of measured points. The model's grid is cylindrical and uses  $z$ -steps of 2 mm,  $r$ -steps of 5-mm and  $\phi$ -steps of  $5^\circ$ . Longitudinal steps in the measurement grid are variable, however the minimum  $z$ -step used is 25 mm, with  $\phi$ -steps of  $20^\circ$ . The radial steps for the measured points are of course limited to the 30 mm separation of the Hall probes.

The scaling parameter is intended to account for any change from the current supplied to the coils. Whilst they are nominally powered at 30 A, a minimal amount of deviation from this is expected. As mentioned, the bracketing fields are made with the estimated rotation

angles and offsets listed in section 3.9.4 applied. Further rotations and offsets are allowed as model parameters to improve on the estimates.

The bracketing fields for each coil are calculated using the centre positions listed in tables 3.7 and 3.8. As with the rotations/offsets, these are estimates used so the model converges quicker. Any deviation from these centre positions is accounted for with the  $p_z$  parameter.

Using the parameters found from the fitting procedure, a geometrical fit model of a coil is made by applying steps 1-4 to the bracketing fields. In order to obtain this field on a cylindrical grid centred on the  $z$ -axis, linear interpolation is used. The density of points of this grid is left to the end user to decide. It must be less dense than the bracketing fields to minimise errors introduced by the interpolation. The grid used for this thesis uses  $z$ -steps of 5 mm,  $r$ -steps of 10 mm and  $\phi$ -steps of  $15^\circ$ .

The results of this model are discussed in section 4.2.4. The residual field used for the Fourier-Bessel fit is described in section 4.2.5.

## 4.2.2 Geometrical Fit Model for ECE Data

Bracketing fields are made for E1, CC and E2 in the usual way. The technique is much the same as mentioned in the previous section with a few exceptions. In this case there are: three mixing parameters –  $m_{E1}, m_{CC}, m_{E2}$ ; three scaling parameters –  $s_{E1}, s_{CC}, s_{E2}$  and three longitudinal offsets –  $p_z^{E1}, p_z^{CC}, p_z^{E2}$ . The procedure is as follows:

1. For the two E1 bracketing fields, at each point add the components in proportion:

$$B_{c,i}^{E1} = m_{E1} B_{c,i}^{LT} + (m_{E1} - 1) B_{c,i}^{SF} \quad (4.9)$$

2. Repeat step 1 for the E2 and CC bracketing fields to obtain the three mixed fields –  $B_{c,i}^{E1}, B_{c,i}^{E2}, B_{c,i}^{CC}$ .

3. Scale each of these fields by the corresponding scale factor:

$$\begin{aligned} B_{c,i}^{E1s} &= s_{E1} B_{c,i}^{E1} \\ B_{c,i}^{CCs} &= s_{CC} B_{c,i}^{CC} \\ B_{c,i}^{E2s} &= s_{E2} B_{c,i}^{E2} \end{aligned} \quad (4.10)$$

4. Offset each of these scaled fields in the  $z$  direction by the corresponding offset.

5. Add in superposition these three scaled/mixed fields to form the ECE field:

$$B_{c,i}^{\text{ECE}} = B_{c,i}^{\text{E1s}} + B_{c,i}^{\text{CCs}} + B_{c,i}^{\text{E2s}} \quad (4.11)$$

6. Perform steps 4-6 of the geometrical fit mentioned in the previous section as normal with the resultant field.

This results in a similar function to be minimised by MINUIT with the addition of six more parameters. Then to produce a geometrical fit model of the ECE coils, steps 1-6<sup>1</sup> above are applied to the six bracketing fields with the parameters found from the fit.

### 4.2.3 Geometrical Fit Model of a Complete Spectrometer Solenoid

With the geometrical fit performed on the ECE and match coil data, the fitting parameters are used to generate field maps that represent the field produced by each coil or coil set if they are powered to 30 A. The field produced by a whole spectrometer solenoid can then be built up from these. The strength of the field increases linearly with the current of the coil. Therefore, in order to produce a field map of a spectrometer solenoid with the coils at different currents, simple scaling factors are calculated via:

$$\eta_{\text{magnet}} = \frac{I_{\text{set}}}{30} \quad (4.12)$$

with  $I_{\text{set}}$  being the desired current of the coil. Scaling factors are calculated for each of the model fields i.e for M1, M2 and ECE. Then with the model fields on the same grid as each other, calculating a field map is easily performed by scaling and summing the components at each point:

$$\begin{aligned} B_z &= \eta_{M1} B_z^{\text{M1}} + \eta_{M2} B_z^{\text{M2}} + \eta_{ECE} B_z^{\text{ECE}} \\ B_r &= \eta_{M1} B_r^{\text{M1}} + S \eta_{M2} B_r^{\text{M2}} + \eta_{ECE} B_r^{\text{ECE}} \\ B_\phi &= \eta_{M1} B_\phi^{\text{M1}} + \eta_{M2} B_\phi^{\text{M2}} + \eta_{ECE} B_\phi^{\text{ECE}} \end{aligned} \quad (4.13)$$

where the superscript labels denote the model field map that component is from. This is the case for SSU. For SSD the same is done but without the field from the M1 terms.

<sup>1</sup>Obviously re-calculating the  $\chi^2$  parameter is unnecessary.

### 4.2.4 Geometrical Fit Model Results

Before the residual field is discussed further, the resultant geometrical fit fields are compared to the data. To do this, the individual modelled fields are combined to form field maps of the 3T-SSU, 2T-SSD and 3T-SSD settings. These magnet settings are realistic MICE running settings, therefore they are used as the comparison data for the model. The residuals for each component are calculated for every point:

$$\Delta B_c = B_c^{\text{measured}} - B_c^{\text{geofit}} \quad (4.14)$$

The following histograms show the residuals between the full geometrical fit models of the three settings mentioned above and the data.

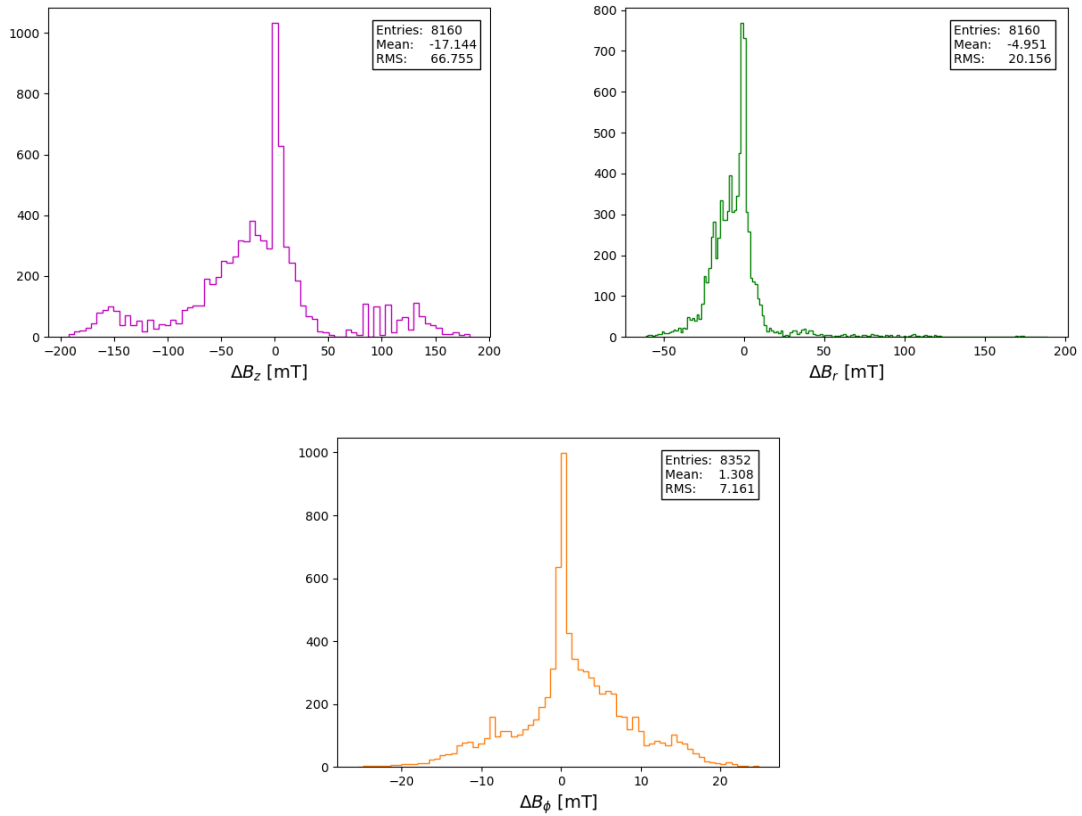


Fig. 4.3 Histograms of the residuals between the geometrical fit model and the data for the 3T-SSU setting for each field component.

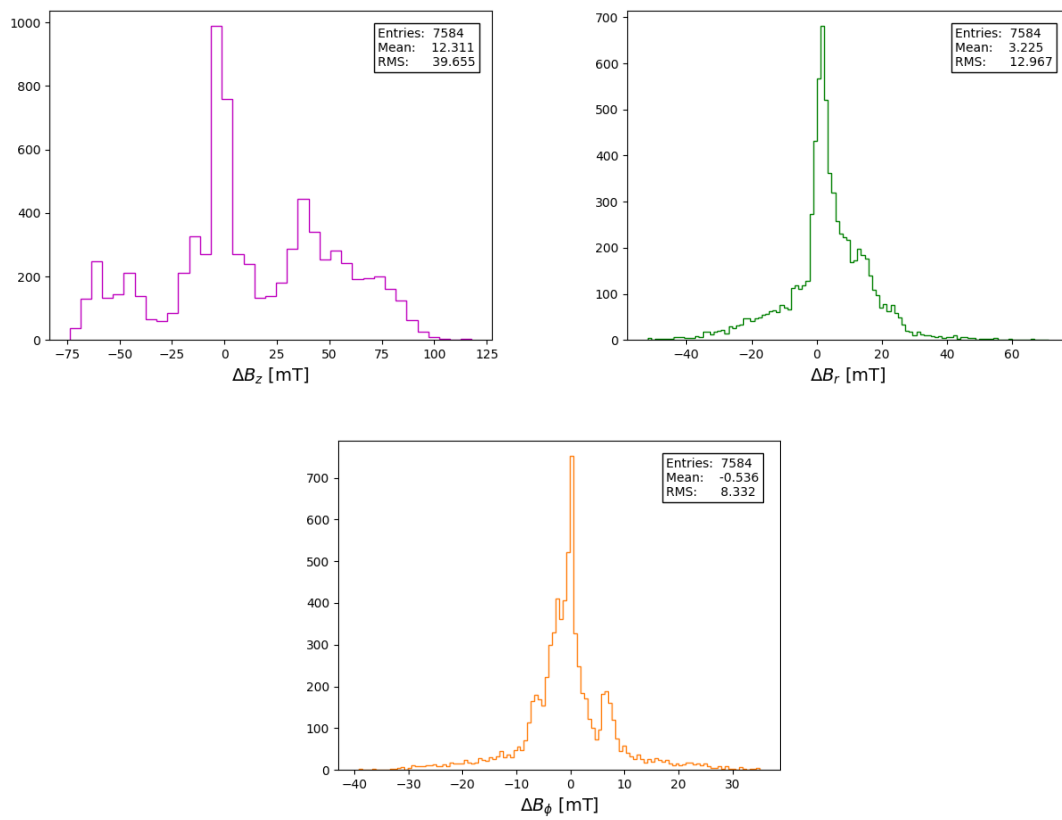


Fig. 4.4 Histograms of the residuals between the geometrical fit model and the data for the 2T-SSD setting for each field component.

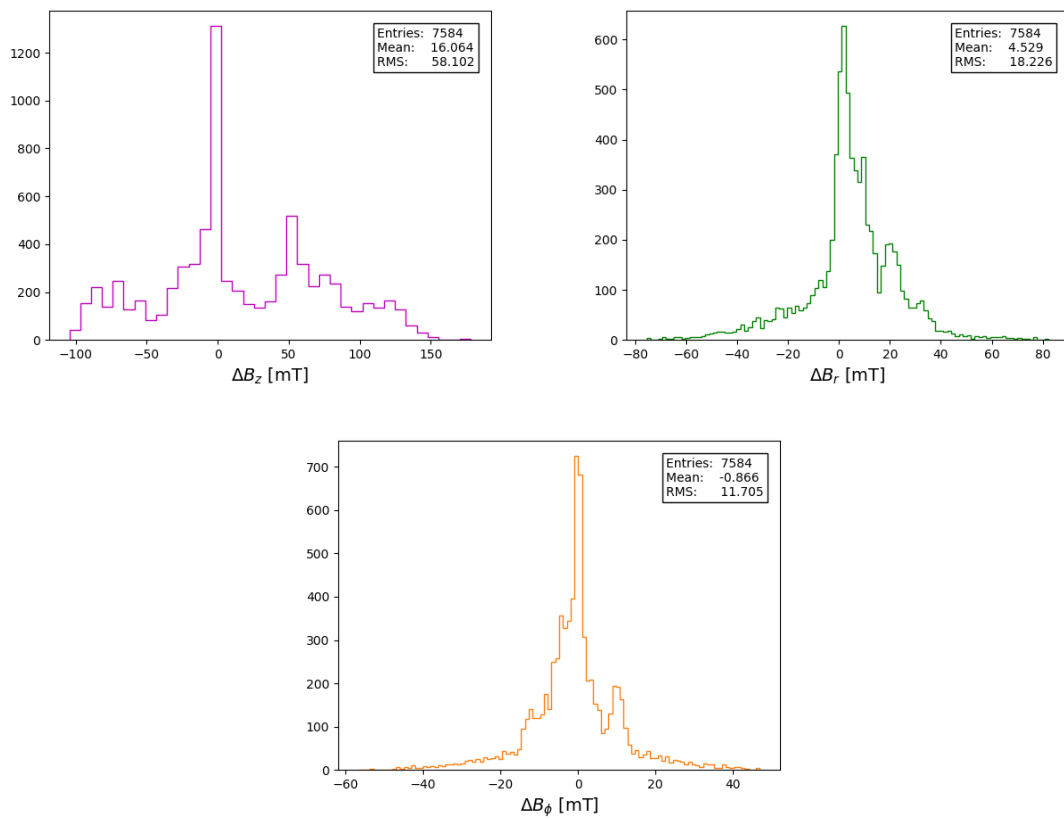


Fig. 4.5 Histograms of the residuals between the geometrical fit model and the data for the 3T-SSD setting for each field component.

The histograms show large shoulders of residuals, especially for the  $B_z$  component. These shoulders are due to the effect from the PRY as will be demonstrated in section 4.2.6. Although they show fairly poor agreement to the data, these histograms serve as useful comparisons for when the Fourier-Bessel model is applied.

#### 4.2.5 Forming the Residual Field

As will be shown, the Fourier-Bessel model uses the measured  $B_z$  component of the field<sup>2</sup> on the surface of a bounding cylinder to find parameters which can then be used to deduce the field within the cylinder volume. With the survey corrections applied, the measurements no longer sit on concentric cylinders of points.

Cubic spline interpolation is used to interpolate the data onto points which are equal in radius from the MICE beam axis. In fact, the measurements are interpolated onto points as if the mapping machine was perfectly aligned to the beam axis. The cubic spline algorithm used also allows points to be extrapolated slightly, as some of the points sit outside the cylinder with a radius of 0.15 m by only a few millimetres. A cubic spline is fitted to the  $B_z$  components for each  $z$  slice of data, an example of which is shown in figure 4.6.

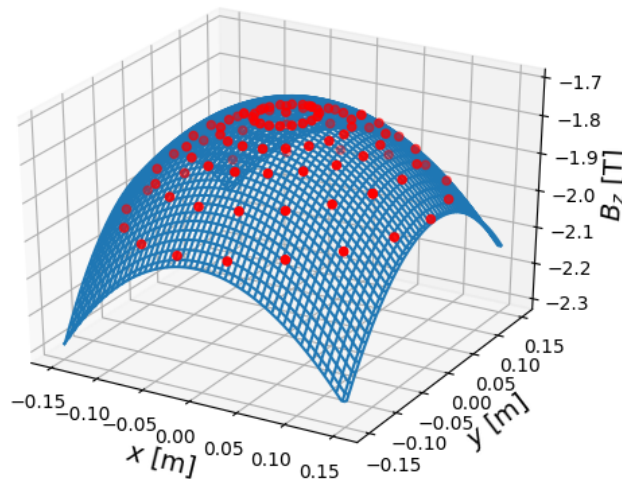


Fig. 4.6 Example of a fitted cubic spline to the  $B_z$  component at a  $z$  slice of data. The red points show the data and the blue surface is the fitted cubic spline.

<sup>2</sup> Note that part of the model utilises the  $B_r$  component, but this is done without interpolation and is discussed later.

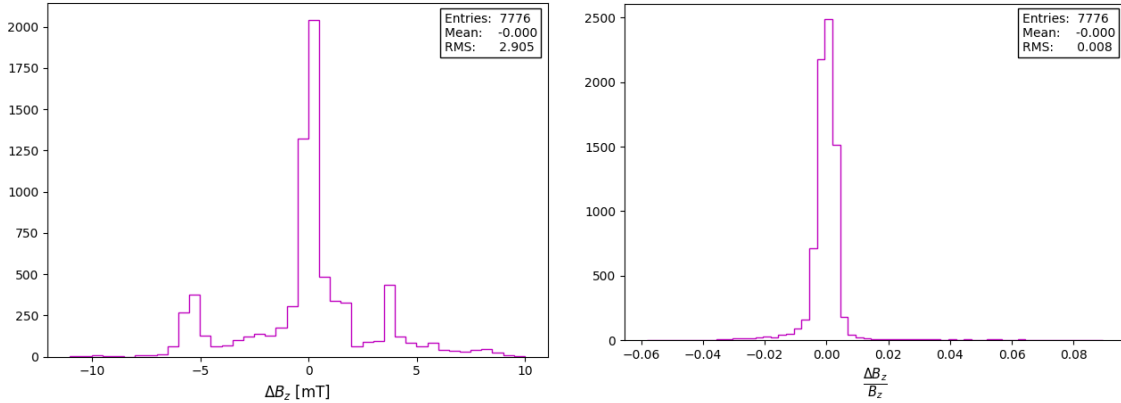


Fig. 4.7 Histograms of the absolute (left) and fractional (right) residuals between the interpolated values and data.

Since the data is on a relatively coarse polar grid, the interpolation is expected to contribute systematic errors. To investigate the errors induced, the cubic spline fit was applied to all  $z$  positions in the 3T-SSD field map. Each fitted spline was used then used to interpolate the value of  $B_z$  at each of the data points. The residuals between the data and the cubic spline were then calculated and are plotted in figure 4.7.

The residuals are centred around zero, however, two small extra peaks in the absolute residual are present. The cause of these peaks is most likely due to the field in the region between coils where the field gradients are high and  $B_z$  changes rapidly with  $r$ . Calculating the fractional residuals show that the interpolated values show good agreement with a spread of  $\sim 1\%$ .

With the data interpolated onto coaxial cylinders centred on the  $z'$  axis, with radii equal to the probe radii from the centre of the mapper disk, the residual field is calculated at all points in space of the interpolated data. The geometrical fit models are made to be on axis so that calculating the residual field is easy. Explicitly written, the residual field,  $B_z^{\text{Resid}}$ , at a point,  $i$ , is given by:

$$B_{z,i}^{\text{Resid}} = B_{z,i}^{\text{Data}} - B_{z,i}^{\text{Geo}} \quad (4.15)$$

where  $B_{z,i}^{\text{Data}}$  are the field components from the interpolated data field and  $B_{z,i}^{\text{Geo}}$  are the components from the geometrical fit model. This equation is important to consider for when the full model is calculated as described later. A residual field is produced for every 30A setting to enable the Fourier-Bessel model to be applied to all individual coils or the ECE coil set.

### 4.2.6 Effect of the PRY

With the geometrical fit model of the spectrometer solenoids and the method of producing the residual field mentioned above, the residual  $B_z$  component of the field can be plotted at different radii. The residual field for the 3T-SSU and 3T-SSD settings for each cylindrical surface are shown in figures 4.8 and 4.9 respectively.

The residual field plots show the cause of the shoulders in the histograms in section 4.2.4. The residual  $B_z$  field slowly increases in strength and then rapidly decreases at the upstream region of SSU. The effect is reversed for SSD, due to the negative  $B_z$  field, and occurs at the downstream region. This effect is thought to be caused by the end plates of the PRY with the rapid decline occurring in the region where the mapper disk passes through the hole in the end plate.

The slow rise of the residual  $B_z$  starts to occur in the region where the scintillating fibre trackers are. This is the most important region for the field models as the particle tracking algorithm requires knowledge of the  $B_z$  field. The motivation for the Fourier-Bessel model is clear from these plots.

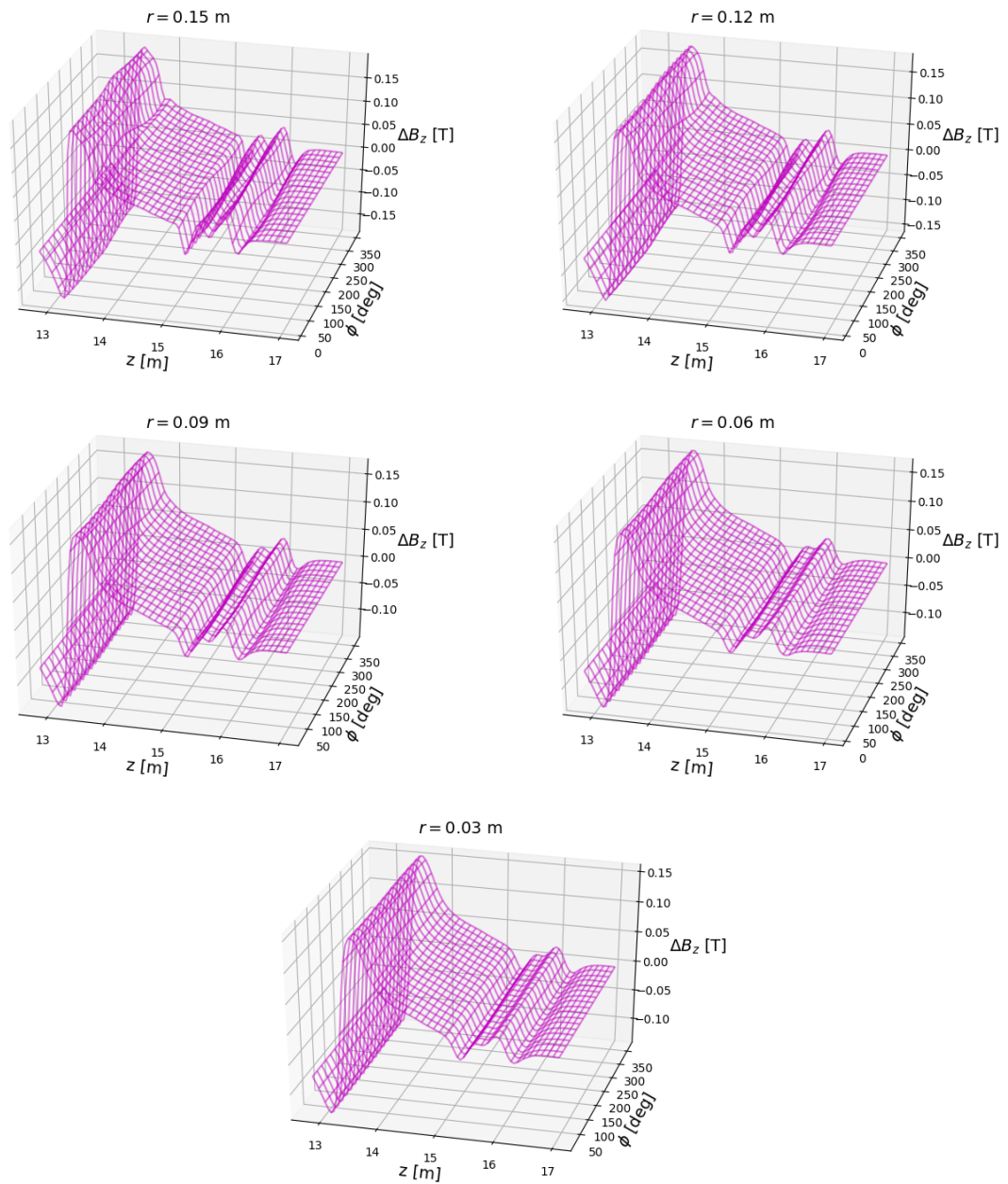


Fig. 4.8 Plots showing the residual axial field for all  $z$  and  $\phi$  for each cylindrical surface. These plots show the residual between the geometrical fit model and the 3T-SSU setting.

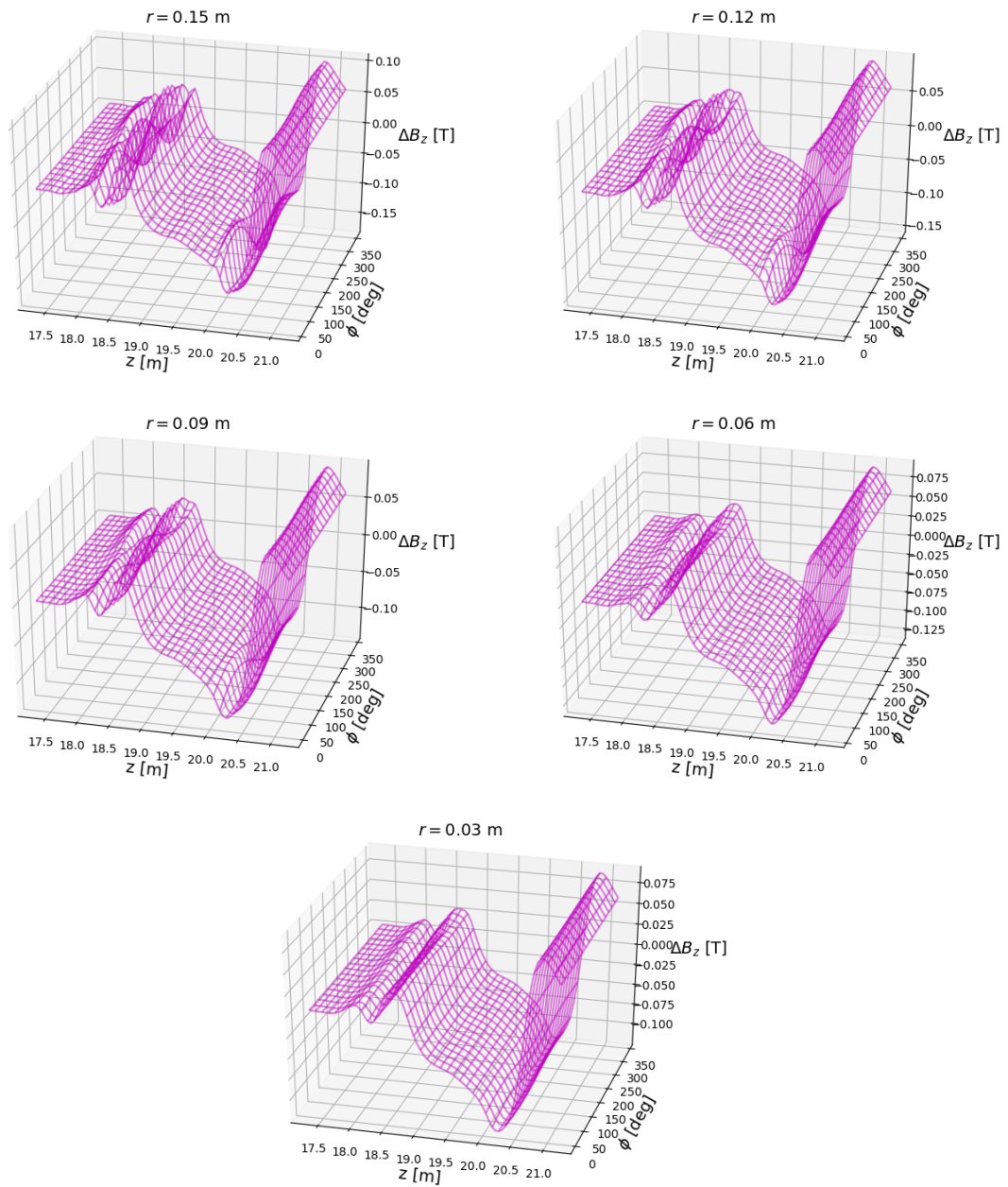


Fig. 4.9 Plots showing the residual axial field for all  $z$  and  $\phi$  for each cylindrical surface. These plots show the residual between the geometrical fit model and the 3T-SSD setting.

### 4.3 Fourier-Bessel Model

With the residual field centred on the axis, it is now possible to apply the Fourier-Bessel model to represent it so that the full field of a coil can be modelled. This model exploits Maxwell's equations to obtain series expansions with coefficients and phases which, when found, allow the field to be calculated within the volume of interest. The properties of the Bessel functions allow a staged fitting procedure to find the coefficients and phases.

Starting with the knowledge that within the bore of the solenoid it is only occupied by air i.e there are no sources of current or charge. Therefore, the magnetic field,  $\vec{B}$ , must obey the equations:

$$\begin{aligned}\nabla \times \vec{B} &= 0 \\ \nabla \cdot \vec{B} &= 0\end{aligned}\tag{4.16}$$

Then expressing the magnetic field in terms of a scalar potential,  $\Phi$ , via:

$$\vec{B} = \nabla\Phi\tag{4.17}$$

Combining the second equation in 4.16 with equation 4.17, the Laplace equation is obtained:

$$\nabla^2\Phi = 0\tag{4.18}$$

Working in cylindrical polar coordinates, solutions to the Laplace equation can be found using separation of variables. The scalar potential then becomes:

$$\Phi(r, \phi, z) = R(r)P(\phi)Z(z)\tag{4.19}$$

Performing separation of variables yields the solutions for the radial, axial and azimuthal functions. The radial and axial solutions appear in three different forms according to the separation constant:

$$\begin{aligned}Z(z) &= A \sin(\lambda z) + B \cos(\lambda z) \\ R(r) &= CI_n(\lambda r)\end{aligned}\tag{4.20}$$

$$\begin{aligned}Z(z) &= A \sinh(\lambda z) + B \cosh(\lambda z) \\ R(r) &= CJ_n(\lambda r)\end{aligned}\tag{4.21}$$

$$\begin{aligned} Z(z) &= Az + B \\ R(r) &= Cr^n \end{aligned} \quad (4.22)$$

where A, B and C are arbitrary constants,  $\lambda > 0$  and  $n \in \mathbb{N}_0$ . The functions  $J_n(\lambda r)$  and  $I_n(\lambda r)$  are  $n^{\text{th}}$ -order Bessel and modified Bessel functions respectively. Due to the periodicity of the  $\phi$  coordinate, the azimuthal factor is always:

$$P(\phi) = A \sin(n\phi) + B \cos(n\phi) \quad (4.23)$$

The general solution to  $\Phi(r, \phi, z)$  is then formed by an infinite sum over these terms. According to equation 4.17 the individual components of the magnetic field,  $\vec{B}$ , are given by:

$$\begin{aligned} B_z(r, \phi, z) &= \frac{\partial \Phi(r, \phi, z)}{\partial z} \\ B_r(r, \phi, z) &= \frac{\partial \Phi(r, \phi, z)}{\partial r} \\ B_\phi(r, \phi, z) &= \frac{1}{r} \frac{\partial \Phi(r, \phi, z)}{\partial \phi} \end{aligned} \quad (4.24)$$

The full expansions for the  $B_z, B_\phi$  and  $B_r$  components are then given by:

$$\begin{aligned} B_z(r, \phi, z) &= \sum_{n=0}^{\infty} \sum_{l=1}^{\infty} A_{nl} I_n \left( \frac{l\pi}{z_{\max}} r \right) \cos(n\phi + \alpha_{nl}) \cos \left( \frac{l\pi}{z_{\max}} z \right) \\ &\quad - \sum_{n=0}^{\infty} \sum_{l=1}^{\infty} B_{nl} I_n \left( \frac{l\pi}{z_{\max}} r \right) \cos(n\phi + \beta_{nl}) \sin \left( \frac{l\pi}{z_{\max}} z \right) \\ &\quad + \sum_{n=0}^{\infty} A_{n0} r^n \cos(n\phi + \alpha_{n0}) \\ &\quad + \sum_{n=0}^{\infty} \sum_{m=1}^{\infty} C_{nm} J_n \left( \frac{\zeta_{nm}}{r_{\max}} r \right) \cos(n\phi + \gamma_{nm}) \cosh \left( \frac{\zeta_{nm}}{r_{\max}} z \right) \\ &\quad + \sum_{n=0}^{\infty} \sum_{m=1}^{\infty} D_{nm} J_n \left( \frac{\zeta_{nm}}{r_{\max}} r \right) \cos(n\phi + \delta_{nm}) \sinh \left( \frac{\zeta_{nm}}{r_{\max}} z \right) \end{aligned} \quad (4.25)$$

$$\begin{aligned}
B_r(r, \phi, z) = & \sum_{n=0}^{\infty} \sum_{l=1}^{\infty} A_{nl} I'_n \left( \frac{l\pi}{z_{\max}} r \right) \cos(n\phi + \alpha_{nl}) \sin \left( \frac{l\pi}{z_{\max}} z \right) \\
& + \sum_{n=0}^{\infty} \sum_{l=1}^{\infty} B_{nl} I'_n \left( \frac{l\pi}{z_{\max}} r \right) \cos(n\phi + \beta_{nl}) \cos \left( \frac{l\pi}{z_{\max}} z \right) \\
& + \sum_{n=0}^{\infty} A_{n0} n r^{n-1} \cos(n\phi + \alpha_{n0}) z \\
& + \sum_{n=0}^{\infty} \sum_{m=1}^{\infty} C_{nm} J'_n \left( \frac{\zeta_{nm}}{r_{\max}} r \right) \cos(n\phi + \gamma_{nm}) \sinh \left( \frac{\zeta_{nm}}{r_{\max}} z \right) \\
& + \sum_{n=0}^{\infty} \sum_{m=1}^{\infty} D_{nm} J'_n \left( \frac{\zeta_{nm}}{r_{\max}} r \right) \cos(n\phi + \delta_{nm}) \cosh \left( \frac{\zeta_{nm}}{r_{\max}} z \right) \\
& + \sum_{n=0}^{\infty} E_n n r^{n-1} \cos(n\phi + \varepsilon_n)
\end{aligned} \tag{4.26}$$

$$\begin{aligned}
B_\phi(r, \phi, z) = & - \sum_{n=0}^{\infty} \sum_{l=1}^{\infty} A_{nl} \frac{z_{\max}}{l\pi r} I_n \left( \frac{l\pi}{z_{\max}} r \right) \sin(n\phi + \alpha_{nl}) \sin \left( \frac{l\pi}{z_{\max}} z \right) \\
& - \sum_{n=0}^{\infty} \sum_{l=1}^{\infty} B_{nl} \frac{z_{\max}}{l\pi r} I_n \left( \frac{l\pi}{z_{\max}} r \right) \sin(n\phi + \beta_{nl}) \cos \left( \frac{l\pi}{z_{\max}} z \right) \\
& - \sum_{n=0}^{\infty} A_{n0} n r^{n-1} \sin(n\phi + \alpha_{n0}) z \\
& - \sum_{n=0}^{\infty} \sum_{m=1}^{\infty} C_{nm} \frac{r_{\max}}{\zeta_{nm} r} J_n \left( \frac{\zeta_{nm}}{r_{\max}} r \right) \sin(n\phi + \gamma_{nm}) \sinh \left( \frac{\zeta_{nm}}{r_{\max}} z \right) \\
& - \sum_{n=0}^{\infty} \sum_{m=1}^{\infty} D_{nm} \frac{r_{\max}}{\zeta_{nm} r} J_n \left( \frac{\zeta_{nm}}{r_{\max}} r \right) \sin(n\phi + \delta_{nm}) \cosh \left( \frac{\zeta_{nm}}{r_{\max}} z \right) \\
& - \sum_{n=0}^{\infty} E_n n r^{n-1} \sin(n\phi + \varepsilon_n)
\end{aligned} \tag{4.27}$$

where  $A_{nl}, B_{nl}, C_{nm}, D_{nm}$  and  $E_n$  are coefficients,  $\alpha_{nl}, \beta_{nl}, \gamma_{nm}, \delta_{nm}$  and  $\varepsilon_n$  are phases and  $\zeta_{nm}$  is the  $m^{\text{th}}$  root of the  $n^{\text{th}}$  order Bessel function. The factors of  $\frac{z_{\max}}{l\pi}$  and  $\frac{\zeta_{nm}}{r_{\max}}$  from the differentiation with respect to  $r$  and  $z$  are absorbed into the coefficients for equations 4.25 and 4.26, hence the appearance of their reciprocals in the  $B_\phi$  expansion. The azimuthal factor has been re-written in the form  $A \cos(n\phi + \psi)$ .

The terms in each expansion can be logically divided into three groups:

1. **Fourier terms.** These constitute the first three lines of each of the expansions 4.25–4.27. They have the coefficients  $A_{nl}, B_{nl}$  and phases  $\alpha_{nl}, \beta_{nl}$ . These terms contribute the most to the residual field.

2. **Hyperbolic terms.** As the name suggests, these are the terms containing the hyperbolic functions. They have coefficients  $C_{nm}, D_{nm}$  and phases  $\gamma_{nm}, \delta_{nm}$ .
3. **Multipole terms.** These are the very last terms in the expansions 4.26 and 4.27 with coefficients  $E_n$  and phases  $\varepsilon_n$ . They do not contribute to the  $B_z$  component of the field since they originate from the constant term in equations 4.22 and disappear during differentiation.

This separation of the terms then becomes useful as each set of terms can be found by fitting to different parts of the field. Since the axial component of the field is the strongest and the most important, it is desirable to calculate the majority of the coefficients/phases from the expansion 4.25. The two parameters,  $z_{\max}$  and  $r_{\max}$ , are free to be set.

By setting  $r_{\max}$  to 0.15 m, the outermost radius of points of the residual field, and setting  $z_{\max}$  to a suitable length that encapsulates the coil's sphere of influence, a bounding cylinder of points is formed. The coefficients and phases for each of the terms can be found from the values of the residual field on this cylinder which can be used to calculate the residual field at any point within the volume. As for the coil's 'sphere of influence', it is arbitrarily taken to be the region in  $z$  where the strongest field component is above 1 mT. This corresponds to 0.75 m for the match coils and 1.5 m for the ECE sets.

The coefficients and phases for the three sets of terms are found by fitting to different parts of the bounding cylinder.

### 4.3.1 Determining the Coefficients for the Fourier Terms

When  $r = r_{\max}$ , the Bessel functions in the hyperbolic terms are equal to zero due to the  $\zeta_{nm}$  parameter. Therefore, the  $B_z$  component of the field on the curved surface of the cylinder is completely described by the Fourier terms,  $B^F$ .

A least squares fit is performed over the points on the curved surface by minimising the parameter:

$$\chi^2 = \sum_{i=0}^N \frac{\left( B_{i,z}^{\text{Resid}} - B_{i,z}^F \right)^2}{\sigma^2} \quad (4.28)$$

where  $B_{i,z}^{\text{Resid}}$  is the value of the residual field at point  $i$  and  $B_{i,z}^F$  is calculated from the Fourier terms and  $\sigma$  is again estimated at 1 mT. The expansions must be truncated at some point. Due to the cylindrical symmetry of solenoid fields, terms with  $n = 0, 1$  are used. The  $z$  dependence is much larger and so terms with  $l = 1-20$  are used.

### 4.3.2 Determining the Coefficients for the Hyperbolic Terms

Due to the hyperbolic functions, the hyperbolic terms,  $B^{\text{Hyp}}$ , are largest at the points where  $z = \pm z_{\text{max}}$ . To find the coefficients and phases of these terms, the newly found Fourier terms are first subtracted from each point of the residual field at the cylinder ends to give:

$$B_{i,z}^{\text{Resid-F}} = B_{i,z}^{\text{Resid}} - B_{i,z}^{\text{F}} \quad (4.29)$$

Then a least squares fit is performed in the same way as for the Fourier terms except with the square residuals being calculated between  $B_{i,z}^{\text{Resid-F}}$  and  $B_{i,z}^{\text{Hyp}}$ .

### 4.3.3 Determining the Coefficients for the Multipole Terms

The multipole terms,  $B^{\text{M}}$ , do not contribute to the  $B_z$  component. Instead these terms are found from the  $B_r$  component on the curved surface of the cylinder. The contributions to the field from the Fourier and Hyperbolic terms are subtracted from the residual field at each point:

$$B_{i,r}^{\text{Resid-F-Hyp}} = B_{i,r}^{\text{Resid}} - B_{i,r}^{\text{F}} - B_{i,r}^{\text{Hyp}} \quad (4.30)$$

Then for each  $\phi$ , the calculated  $B_{i,r}^{\text{Resid-F-Hyp}}$  values are averaged over  $z$ . The multipole terms can then be found using a least squares fit in a similar fashion to the Fourier and Hyperbolic terms but utilising the variation with  $\phi$  only.

Note that the residual field for the  $B_r$  component is not formed using the cubic spline interpolation method. Instead it is directly from the geometrical fit and the data so that the points are not perfectly on a cylinder. Then the approximation that  $r = r_{\text{max}}$  for these points is used. This approximation is fine considering that the multipole terms are very small and do not contribute to the  $B_z$  component which is the most important.

Any component of the field from the Fourier-Bessel model at any point within the bounding cylinder can then be calculated from the expansions 4.25–4.27.

### 4.3.4 Fourier-Bessel Fit Examples

The Fourier-Bessel fit to the residual field on the outer surface is illustrated in figure 4.10. Both the residual field and the field as calculated by the Fourier-Bessel expansions are plotted together. These plots only show the residual fields for SSU.

The Fourier-Bessel model fits the contours of the residual field well. The effect of the end plate of the PRY is clearly visible in the ECE plot. In the plots for the M1 and M2 coil there is significant deviation between the expansion and residual field, especially at low  $z$ .

These regions are not within  $\pm z_{\max}$  from the centre of the coil, therefore terms from the Fourier-Bessel model are not applied there.

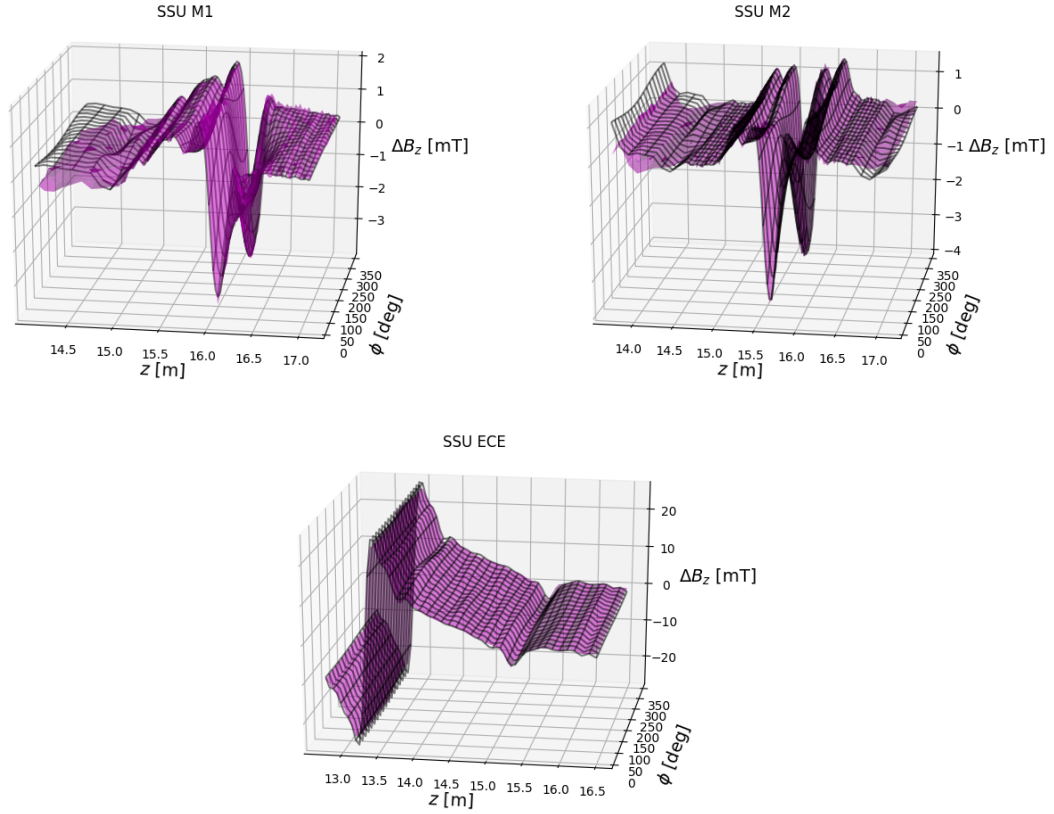


Fig. 4.10 Examples of the Fourier-Bessel fit to the residual  $B_z$  field on the bounding cylinder surface. The residual fields are represented by the purple surfaces. The black wire frame surfaces are calculated from the  $B_z$  expansion.

### 4.3.5 Full Field Model

With the coefficients and phases determined for the Fourier-Bessel expansions and with the geometrical fit models of each coil, the full model of a whole spectrometer solenoid can be made. This is achieved using equations 4.13, instead using the full model fields instead of only the fields produced by the geometrical fit.

To produce the the full field models we recall equation 4.15. The Fourier-Bessel model is fitted to the residual field and so that:

$$B_{z,i}^{\text{Resid}} \approx B_{z,i}^{\text{FB}} \quad (4.31)$$

The Fourier-Bessel model is also able to model the other two components of the residual field. Then each component of the field at a point is given by:

$$B_{c,i}^{\text{Full}} = B_{c,i}^{\text{Geo}} + B_{c,i}^{\text{FB}} \approx B_{c,i}^{\text{Data}} \quad (4.32)$$

Then with the full model for each of the 30 A settings, the full field models of the spectrometer solenoids can be made as discussed above.

## 4.4 Results of the Full Model

Using the full models of each coil, field maps of both spectrometer solenoids are made for the 3T settings. A field model for the 2T-SSD setting is also made. Then the residual  $B_z$  field between the full model and the data is generated in the same way as section 4.2.6.

The residual  $B_z$  field between the full models and the interpolated data at each radial surface are shown in figures 4.11, 4.12 and 4.13 for of the 3T-SSU, 3T-SSD and 2T-SSD settings respectively.

These residual fields show a noticeable improvement from those of just the geometrical fit. The residuals typically sit within  $\pm 30$  mT. They exhibit periodic ripples in the regions where match coils are which are far more noticeable for SSU which is likely due to both match coils being in operation. The source for these ripples is not known although it could be due to a few things.

Firstly, more terms for the Fourier-Bessel expansion might be required to resolve the fine structure of the field abnormalities. This is likely the cause for the pronounced ripples in the  $\phi$  direction for the SSD residual fields. Adding more terms, however, becomes more computationally expensive for diminishing returns to the increased accuracy.

The Fourier-Bessel model satisfies the Laplace equation, and so the expansions should be able to describe the field almost perfectly, providing many terms are used, within the bounding cylinder. Disagreement between the model and the data can point to measurement errors. Further mixing between measured field components could cause a discrepancy, especially a mixing between the  $z$  and  $r$  components of the field in a similar manner to the mixing angle described in section 3.9.1 that mixes the  $B_\phi$  component with the remaining two.

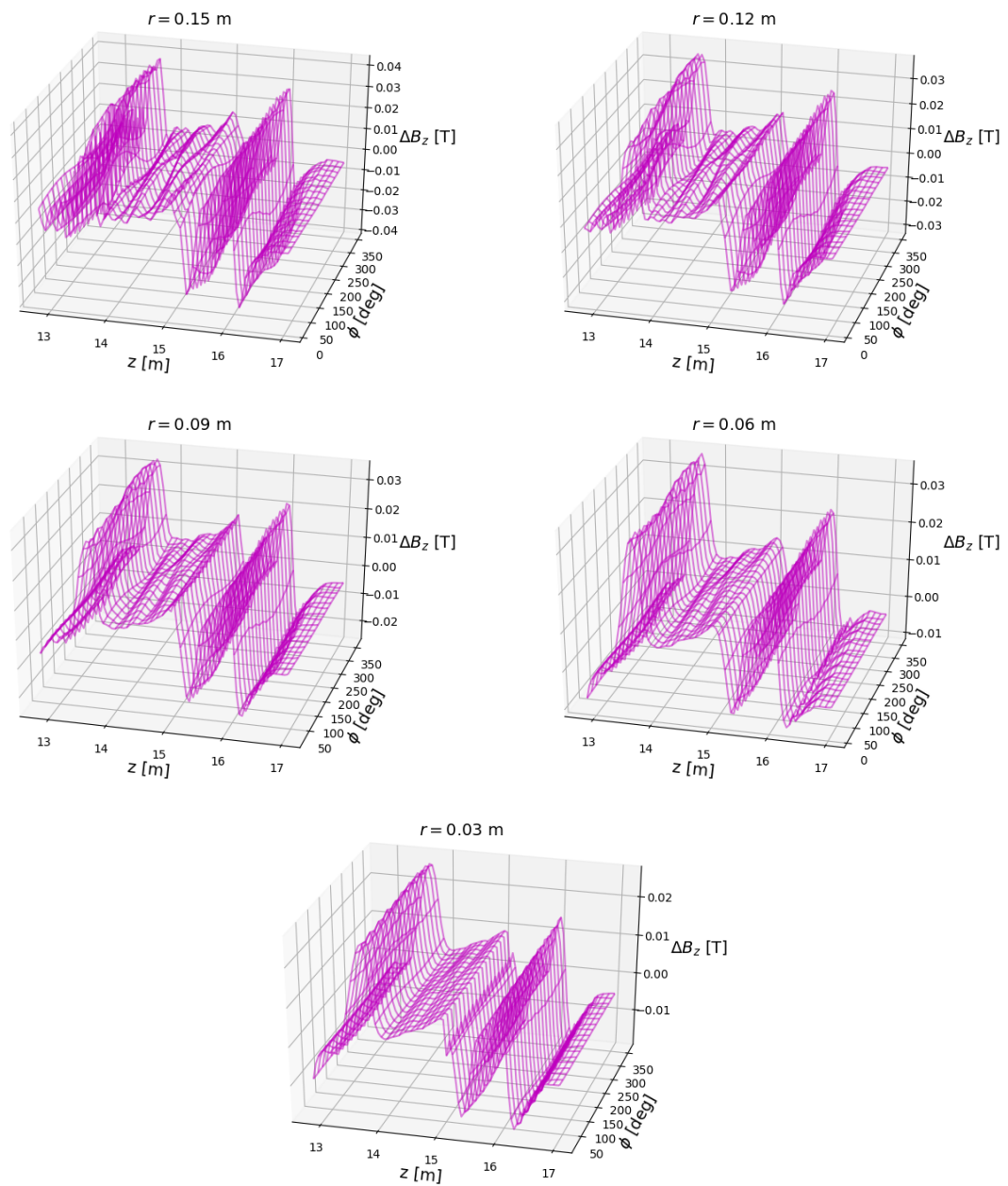


Fig. 4.11 Residual  $B_z$  field on each radial surface between the full field model and the interpolated data for the 3T-SSU setting.

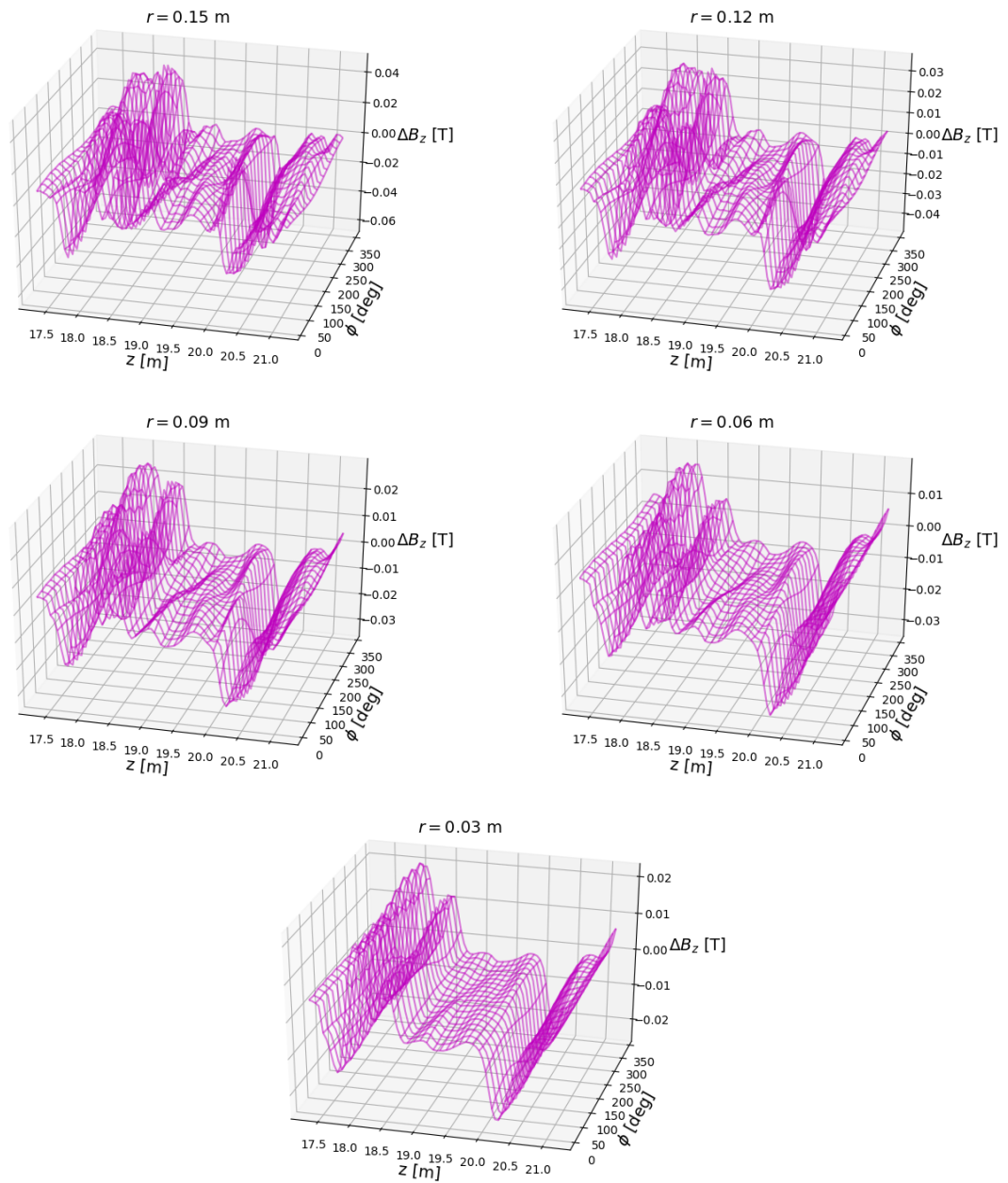


Fig. 4.12 Residual  $B_z$  field on each radial surface between the full field model and the interpolated data for the 3T-SSD setting.

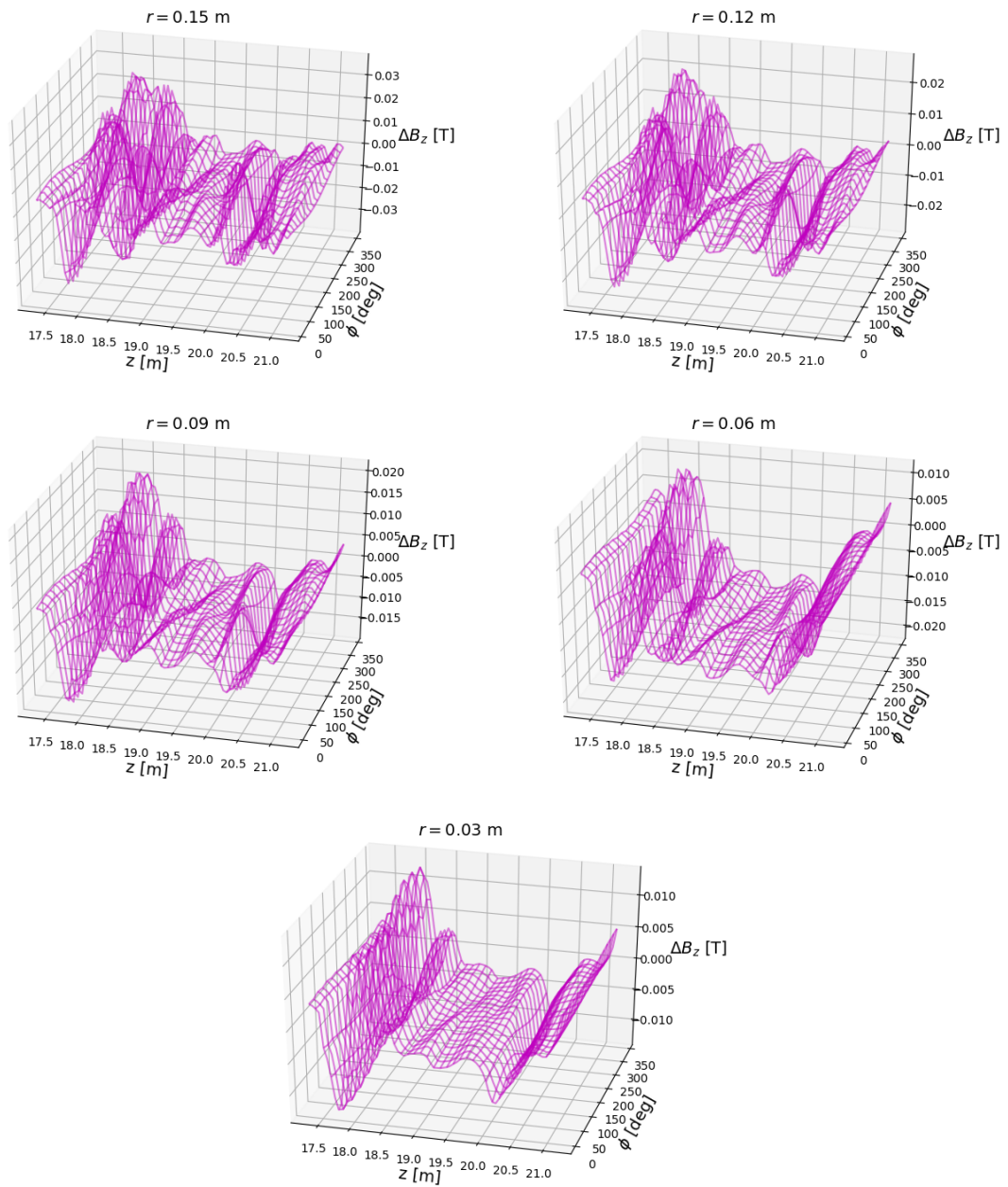


Fig. 4.13 Residual  $B_z$  field on each radial surface between the full field model and the interpolated data for the 2T-SSD setting.

Histograms displaying the residuals between the full field model of the spectrometer solenoids and the actual data are shown in figures 4.14, 4.15 and 4.16. For data points that sit outside the radius of the bounding cylinder,  $r_{\max}$  is used to calculate the Fourier-Bessel terms.

All three field models show a huge improvement in the  $B_z$  residuals compared to those shown in section 4.2.4. Moderate improvements are also seen in the  $B_r$  and  $B_\phi$  residuals.

The double peak feature in the  $B_z$  residuals for the 3T-SSU setting are caused by the ripples discussed previously. The mean  $B_z$  residual for all settings are offset from zero. The cause of this is probably due to the scaling of each modelled field from 30 A to their operating current and the saturation of the PRY. The effect on the field of the PRY will not be equal for all currents due to the magnetisation curve of the steel. This could be investigated with more field map data taken at multiple operating currents and observing if there is any correlation with the offset of the mean residual and the magnetisation curve of the iron that makes up the PRY.

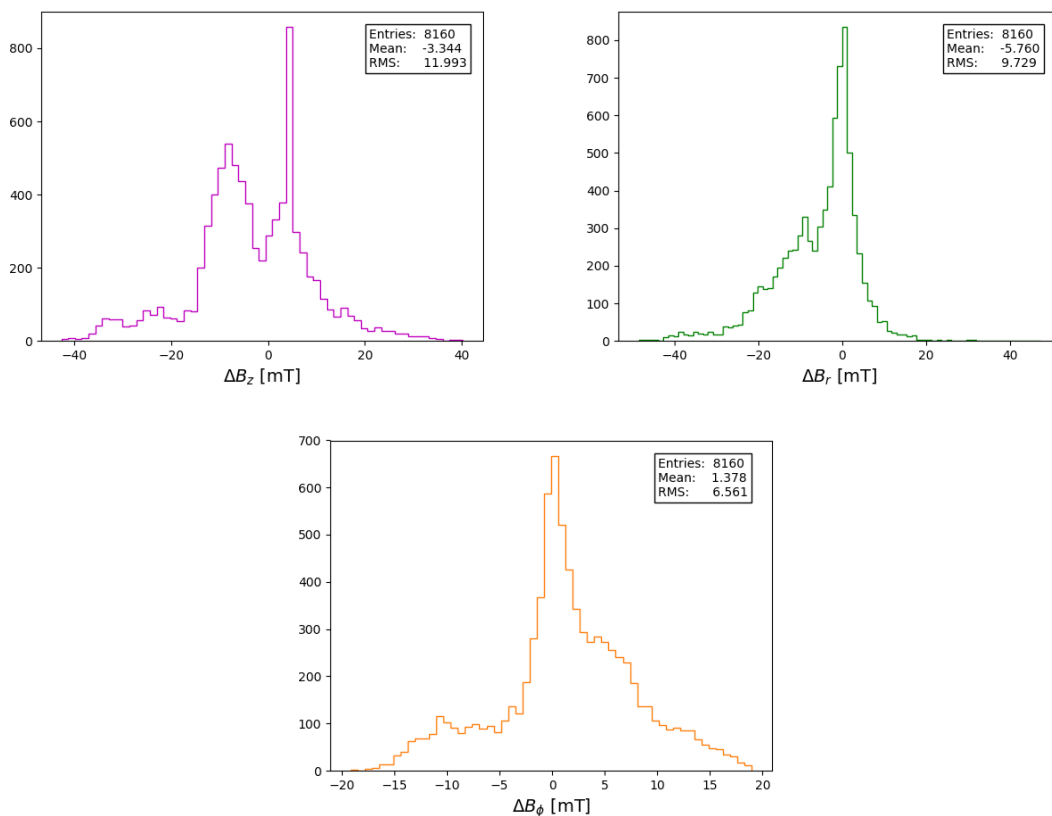


Fig. 4.14 Histograms of the residuals between the full model and the data for the 3T-SSU setting.

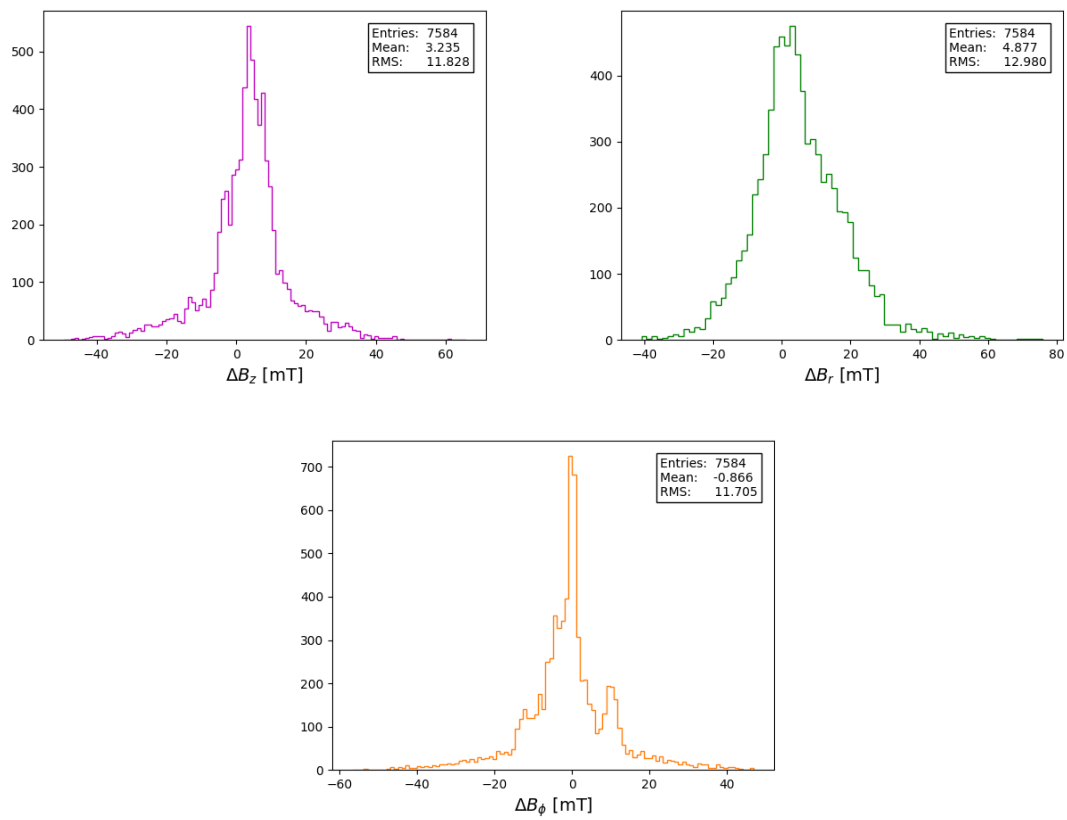


Fig. 4.15 Histograms of the residuals between the full model and the data for the 3T-SSD setting.

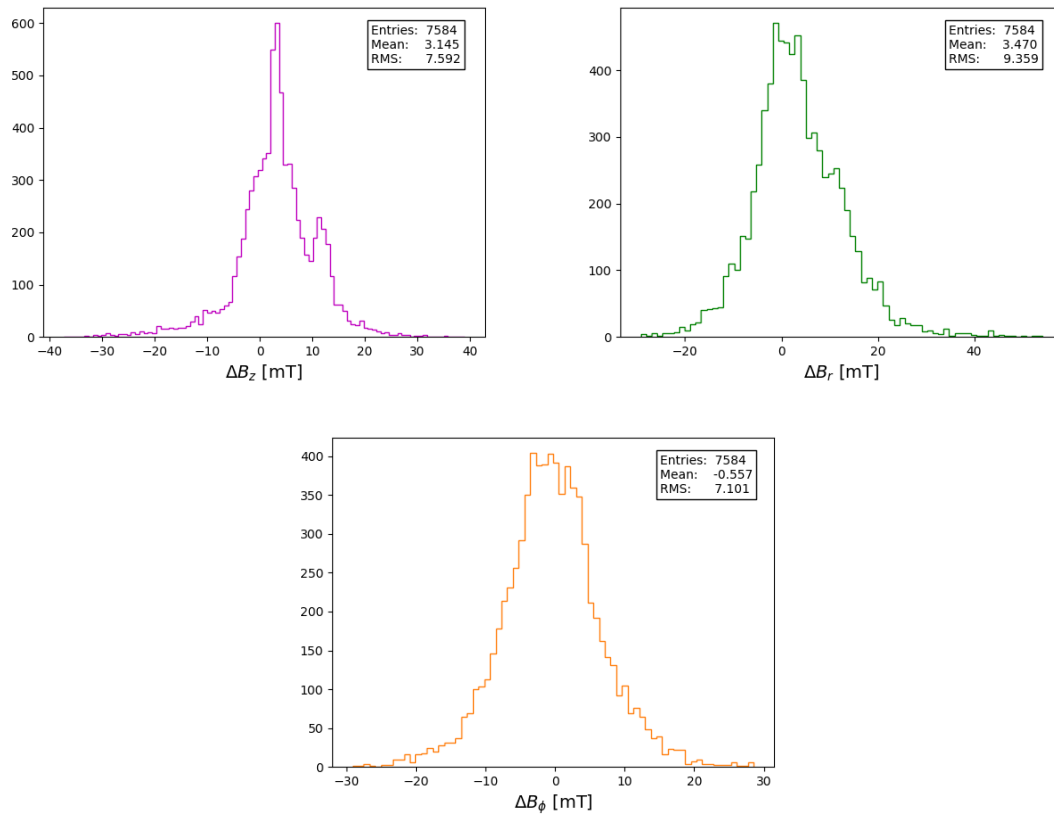


Fig. 4.16 Histograms of the residuals between the full model and the data for the 2T-SSD setting.

It is also useful to look at the fractional error,  $\Delta B_z/B_z$  in the tracker region for these three field maps. For simplicity, the tracker region is taken as the region enclosed by the centre coil only. The fractional error for each comparison field map is shown in figure 4.17 below, note that it has been multiplied by 100 to express it in terms of a percentage error.

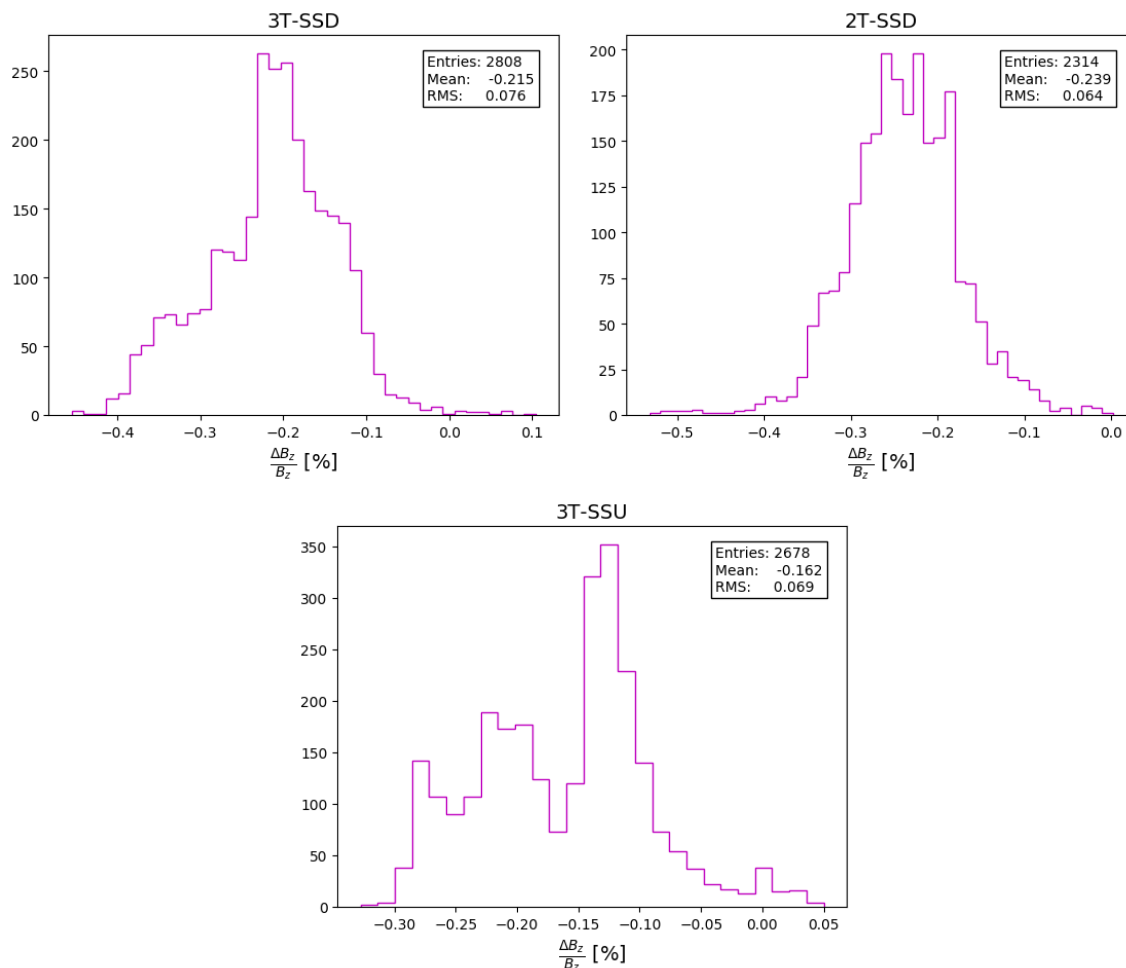


Fig. 4.17 Histograms of the fractional error,  $\Delta B_z/B_z$ , in terms of percentage for the three comparison fields.

## 4.5 Conclusion

Performing simulations of MICE and measuring the emittance from real data relies on knowledge of the magnetic field in which the muons traverse. A model that utilises least squares fitting to the field map data produced by the custom made field mapping machine has been discussed. The model is a hybrid of the so called geometrical fit model and the Fourier-Bessel model which are explained.

The geometrical fit model accounts for most of the field from the coils, however, it does not account for aberrations in the field caused by the PRY. It also does not account for coil imperfections such as varying winding densities or shape deformities, which are not thought to contribute as much. The results of the geometrical fit model highlight the effect of the PRY on the field, especially at the regions close to the end plates. An increase in the axial field is observed within the tracking region compared to what would be produced by the solenoids by themselves.

The residual field is derived from the data and geometrical fit model. This field is then used to determine the coefficients and phases of the Fourier-Bessel expansions which are derived from Laplace's equation. These expansions can then be used to calculate the components of the residual field so that the full model of the field produced by each coil can be given by the geometrical fit model plus corrections from the expansions.

The results of the full field model show large improvements to the residuals of the  $B_z$  component with mild improvements for  $B_r$  and  $B_\phi$ . These results are summarised in table 4.1.

Field Map	$\Delta B_z$ [mT]				$\Delta B_r$ [mT]				$\Delta B_\phi$ [mT]			
	$\mu$	$\sigma$	min	max	$\mu$	$\sigma$	min	max	$\mu$	$\sigma$	min	max
3T-SSU	-3.3	12.0	-42.7	40.2	-5.8	9.7	-48.6	47.4	1.4	6.6	-19.1	19.0
2T-SSD	3.1	7.6	-37.3	39.1	3.47	9.36	-29.2	54.2	-0.6	7.1	-29.2	28.6
3T-SSD	3.2	11.8	-49.5	65.8	4.9	13.0	-40.9	76.0	-0.9	11.7	-56.6	46.9

Table 4.1 Table summarising the residuals of the full field model for each of the MICE beam setting field maps.

The final model agrees with the data fairly well with the residuals having standard deviations of 13 mT or less. Features within the residual field between the full model and data suggest that there is further measurement error caused by further mixing between the components due to Hall probe misalignments.

The results in table 4.1 also show that the mean of the residuals are offset from zero which could be caused by the simple scaling approach used. This is especially noticeable for the two SSD field maps as both the mean and RMS are larger for the 3T setting compared

with the 2T setting. The response of the PRY is not expected to be linear and the iron will saturate at some point. With more field map data at multiple different current settings, it might be possible to account for this effect.

As explained in section 3.1, the fractional error of the axial field component in the tracking region should be kept within  $10^{-4}$  in order to keep the error on the emittance to within  $10^{-3}$ . According to the histograms shown in figure 4.17, this has not been achieved with the mean  $\Delta B_z/B_z$  for the three field maps being approximately  $2 \times 10^{-3}$ .

# Chapter 5

## Conclusions

Particle accelerator based experiments continue to be the driving force in particle physics as the standard model undergoes extensive testing. It is known that the standard model is not a theory of everything and physics beyond it has already been observed in the phenomenon of neutrino oscillations. Two of the primary avenues of research are currently precise measurements of the properties of the Higgs boson and the parameter space of the PMNS matrix. Both of these are currently serviced by hadron colliders. The potential of lepton accelerators, which are ideal machines for precise measurements, is once again being investigated. Muon colliders offer very high energy and clean collisions, with the ability to directly measure the Higgs width via s-channel production. Furthermore, a neutrino factory can provide intense neutrino beams with well known flavour profiles to study CP violation in the lepton sector. However, there are hurdles to overcome to make muon accelerators a reality. One hurdle in particular is the need for cooling of the muon beam produced from pion decays.

The Muon Ionisation Cooling Experiment aims to demonstrate the ionisation cooling technique which is discussed in the first chapter of this thesis. MICE step IV is reliant on a range of particle detectors and superconducting magnets in order to measure the emittance change of a muon beam when it is passed through an absorber material. The two spectrometer solenoids provide the magnetic fields that enable the scintillating fibre trackers to measure the phase space of the MICE muon beam. In order for the Mice Analysis User Software to be able to calculate the emittance from raw data, and to produce simulations of the experiment, the fields produced by the solenoids need to be modelled. For this purpose, a custom made field mapping machine was conceived.

The details of the mapping machine is described in chapter 3. The field for both magnets were measured in March 2018 and these sets of data are used for the field modelling. A survey of the mapping machine was also performed so that the modelled fields can be obtained in the MICE coordinate system. The survey exposed irregularities in the motion of the mapper

disk. The data were also used to find an estimate of the centre positions of each coil and the rotation and offsets from the beam axis. These are necessary parameters to feed into the field models.

Field models for the spectrometer solenoids are produced using two separate models. First, the geometrical fit model accounts for most of the field produced by the coils. This model assumes evenly wound circular coils and can not account for any field distortions caused by the partial return yoke (PRY). To remedy the short comings of the geometrical fit model, the residual field between it and the data is calculated. The terms of the Fourier-Bessel model are then found by fitting to this residual field.

The combined model is then applied to all the 30 A current data allowing a full field model for each spectrometer solenoid to be made. These field models were then compared with the field map data of the MICE beam settings. The residuals show a decent agreement between the model and the data, although some features exist which could be caused by unquantified measurement error. This error could be due to a mixing of the measured  $B_r$  and  $B_z$  components caused by misaligned Hall probes.

The effect of the PRY on the field was explored in section 4.2.6. The response of the PRY is not expected to be linear with the field strength as the iron will saturate. The individual coil models are formed using field maps at low currents which are then scaled up to the desired current for the full models. Evidence of the non-linear scaling of the field due to the PRY is seen in the offset of the mean residuals from zero. Furthermore, the mean and RMS of the residuals are noticeably larger for the 3T-SSD map than they are for the 2T-SSD map which hints at a scaling issue for the full field models. This issue could be further explored with more field map data where the magnets are at a range of currents allowing the response of the PRY with respect to field strength to be quantified.

The goal to model the magnetic field in the tracking region to within a fractional error of  $\Delta B_z/B_z \sim 10^{-4}$  was not realised. Improvements that are discussed above could have made this possible. The technique used in this thesis is likely more suitable for a magnet systems containing just one coil rather than a sequence of coils.

# References

- [1] M Gell-Mann. The eightfold way: A theory of strong interaction symmetry. In *Murray Gell-Mann: Selected Papers*, pages 81–127. World Scientific, 2010.
- [2] G Aad et al. Observation of a new particle in the search for the Standard Model Higgs boson with the ATLAS detector at the LHC. *Physics Letters B*, 716(1):1–29, 2012.
- [3] S Chatrchyan et al. Observation of a new boson at a mass of 125 GeV with the CMS experiment at the LHC. *Physics Letters B*, 716(1):30–61, 2012.
- [4] V Telnov. Higgs factories. *PoS*, IHEP-LHC-2012:018, 2012.
- [5] M Ishida V Barger and W Keung. Total Width of 125 GeV Higgs Boson. *Phys. Rev. Lett.*, 108:261801, 2012.
- [6] Tao Han and Zhen Liu. Potential precision of a direct measurement of the higgs boson total width at a muon collider. *Phys. Rev. D*, 87:033007, Feb 2013.
- [7] S Brodsky. High energy photon–photon collisions at a linear collider. *International Journal of Modern Physics A*, 20(31):7306–7332, 2005.
- [8] A Blondel et al. Report of the ICFA Beam Dynamics Workshop ‘Accelerators for a Higgs Factory: Linear vs. Circular’(HF2012). *arXiv preprint arXiv:1302.3318*, 2013.
- [9] T Behnke et al. The international linear collider technical design report-volume 1: Executive summary. *arXiv preprint arXiv:1306.6327*, 2013.
- [10] A Blondel et al. A High Luminosity e+ e-Collider to study the Higgs Boson. *arXiv preprint arXiv:1208.0504*, 2012.
- [11] Muon accelerator program. [online] <https://map.fnal.gov/muon-collider/graphics.shtml>.
- [12] S Alekhin, A Djouadi, and S Moch. The top quark and higgs boson masses and the stability of the electroweak vacuum. *Physics Letters B*, 716(1):214–219, 2012.
- [13] CJ Johnstone and NV Mokhov. Shielding the muon collider interaction region. In *Particle Accelerator Conference, 1997. Proceedings of the 1997*, volume 1, pages 414–416. IEEE, 1997.
- [14] B Cleveland et al. Measurement of the solar electron neutrino flux with the homestake chlorine detector. *The Astrophysical Journal*, 496(1):505, 1998.

- [15] Q R Ahmad et al. Direct evidence for neutrino flavor transformation from neutral-current interactions in the sudbury neutrino observatory. *Physical review letters*, 89(1):011301, 2002.
- [16] A Bandyopadhyay et al. Physics at a future neutrino factory and super-beam facility. *Reports on Progress in Physics*, 72(10):106201, 2009.
- [17] S Geer. Neutrino factories: Physics. *arXiv preprint hep-ph/0008155*, 2000.
- [18] H. Wiedemann. *Particle Accelerator Physics*. Springer, third edition, 2007.
- [19] D Möhl, G Petrucci, L Thorndahl, and S Van Der Meer. Physics and technique of stochastic cooling. *Physics Reports*, 58(2):73–102, 1980.
- [20] D Neuffer. Multi-TeV muon colliders. In *AIP Conference Proceedings*, volume 156, pages 201–208. AIP, 1987.
- [21] G. Gregoire et al. Proposal to the Rutherford Appleton Laboratory: an international muon ionization cooling experiment (MICE). In *MICE Collaboration Meeting CM4 Berkeley, USA, October 23-26, 2003*.
- [22] CN Booth et al. The design, construction and performance of the MICE target. *Journal of Instrumentation*, 8(03):P03006, 2013.
- [23] D Adams et al. Pion contamination in the MICE muon beam. *Journal of Instrumentation*, 11(03):P03001, 2016.
- [24] G Penn and JS Wurtele. Beam envelope equations for cooling of muons in solenoid fields. *Phys. Rev. Lett.*, 85:764–767, Jul 2000.
- [25] D Neuffer. Comments on ionization cooling channels. *Journal of Instrumentation*, 12(09):T09004, 2017.
- [26] JC Nugent and V Palladino. The physics programme of next MICE Step IV. *TUPME010, IPAC*, 14, 2014.
- [27] A Dobbs, D Forrest, and FJP Soler. The MICE luminosity monitor. In *Journal of Physics: Conference Series*, volume 408, page 012084. IOP Publishing, 2013.
- [28] R Bertoni et al. The design and commissioning of the MICE upstream time-of-flight system. *Nuclear Instruments and Methods in Physics Research Section A: Accelerators, Spectrometers, Detectors and Associated Equipment*, 615(1):14–26, 2010.
- [29] A. de Bari G. Cecchet M. Bonesini, R. Bertoni. The refurbishing of MICE TOF0 and TOF1 detectors, 2012. <http://mice.iit.edu/micenotes/public/pdf/MICE0363/MICE0363.pdf>.
- [30] L Cremaldi et al. A cherenkov radiation detector with high density aerogels. *IEEE Transactions on Nuclear Science*, 56(3):1475–1478, 2009.
- [31] M Bogomilov et al. The MICE muon beam on ISIS and the beam-line instrumentation of the Muon Ionization Cooling Experiment. *Journal of Instrumentation*, 7(05):P05009, 2012.

- [32] M Ellis et al. The design, construction and performance of the MICE scintillating fibre trackers. *Nuclear Instruments and Methods in Physics Research Section A: Accelerators, Spectrometers, Detectors and Associated Equipment*, 659(1):136–153, 2011.
- [33] M Adinolfi et al. The KLOE electromagnetic calorimeter. *Nuclear Instruments and Methods in Physics Research Section A: Accelerators, Spectrometers, Detectors and Associated Equipment*, 482(1-2):364–386, 2002.
- [34] R Asfandiyarov et al. The design and construction of the MICE Electron-Muon Ranger. *Journal of Instrumentation*, 11(10):T10007, 2016.
- [35] D Adams et al. Electron-muon ranger: performance in the MICE muon beam. *Journal of Instrumentation*, 10(12):P12012, 2015.
- [36] R Asfandiyarov, MICE Collaboration, et al. A totally active scintillator calorimeter for the muon ionization cooling experiment (MICE). design and construction. *Nuclear Instruments and Methods in Physics Research Section A: Accelerators, Spectrometers, Detectors and Associated Equipment*, 732:451–456, 2013.
- [37] CD Tunnell and C Rogers. MAUS: MICE analysis user software. *Proc. IPAC'11*, 2011.
- [38] TJ Roberts and DM Kaplan. G4beamline simulation program for matter-dominated beamlines. In *Particle Accelerator Conference, 2007. PAC. IEEE*, pages 3468–3470. IEEE, 2007.
- [39] S Agostinelli et al. Geant4 — a simulation toolkit. *Nuclear Instruments and Methods in Physics Research Section A: Accelerators, Spectrometers, Detectors and Associated Equipment*, 506(3):250 – 303, 2003.
- [40] R Brun and F Rademakers. ROOT—an object oriented data analysis framework. *Nuclear Instruments and Methods in Physics Research Section A: Accelerators, Spectrometers, Detectors and Associated Equipment*, 389(1-2):81–86, 1997.
- [41] M Clausen and L Dalesio. EPICS: Experimental physics and industrial control system. *ICFA Beam Dyn. Newslett.*, 47:56–66, 2008.
- [42] W Grandegger. DATE V1-Data Acquisition Test Environment Users Manual. Technical report, 1996.
- [43] Y Karadzhov. MICE trigger system, 2016. <http://mice.iit.edu/micenotes/public/pdf/MICE0487/MICE0487.pdf>.
- [44] B Wang et al. The design and construction of the MICE spectrometer solenoids. *IEEE Transactions on Applied Superconductivity*, 19(3):1348–1351, 2009.
- [45] D Li SP Virostek, MA Green and MS Zisman. Progress on the design and fabrication of the MICE spectrometer solenoids, 2007. <http://mice.iit.edu/micenotes/public/pdf/MICE0182/MICE0182.pdf>.
- [46] SP Virostek et al. Update on the modification and testing of the MICE superconducting spectrometer solenoids, 2012. <http://mice.iit.edu/micenotes/public/pdf/MICE0378/MICE0378.pdf>.

- 
- [47] G Pasztor and C Schmidt. Dynamic stress effects in technical superconductors and the “training” problem of superconducting magnets. *Journal of Applied Physics*, 49(2):886–899, 1978.
- [48] MA Green and SP Virostek. The dimensions and number of turns for the spectrometer solenoids as-built compared to the original, 2008. [mice.iit.edu/micenotes/public/doc/MICE0207/MICE0207.doc](http://mice.iit.edu/micenotes/public/doc/MICE0207/MICE0207.doc).
- [49] V Blackmore and H Witte. Personal communication, 2015.
- [50] H Witte, S Plate, J Tarrant, and A Bross. Partial return yoke for MICE-general concept and performance. *Proc. of NA-PAC13*, 2013.
- [51] H Witte et al. Partial return yoke for MICE step IV and final step. In *No. FERMILAB-CONF-15-476-APC*, 2015.
- [52] F James and M Roos. Minuit: A System for Function Minimization and Analysis of the Parameter Errors and Correlations. *Comput. Phys. Commun.*, 10:343–367, 1975.
- [53] J Simpson et al. Simple analytic expressions for the magnetic field of a circular current loop, 2001. <https://ntrs.nasa.gov/search.jsp?R=20140002333>.
- [54] E Jones et al. SciPy: Open source scientific tools for Python, 2001–. [Online] <http://www.scipy.org/>.